Quarterly Technical Report

DTIC FILE COPY

Solid State Research

DTIC
S ELECTE
OCT 3 0 1990
E D

1990:1

Lincoln Laboratory

MASSACHUSETTS INSTITUTE OF TECHNOLOGY

LEXINGTON, MASSACHUSETTS

90 10 25 102

This report is based on studies performed at Lincoln Laboratory, a center for research operated by Massachusetts Institute of Technology. The work was sponsored by the Department of the Air Force under Contract F19628-90-C-0002.

This report may be reproduced to satisfy needs of U.S. Government agencies.

The ESD Public Affairs Office has reviewed this report, and it is releasable to the National Technical Information Service, where it will be available to the general public, including foreign nationals.

This technical report has been reviewed and is approved for publication.

FOR THE COMMANDER

Hugh L. Southall

Hugh L. Southall, Lt. Col., USAF
Chief, ESD Lincoln Laboratory Project Office

MASSACHUSETTS INSTITUTE OF TECHNOLOGY
LINCOLN LABORATORY

SOLID STATE RESEARCH

QUARTERLY TECHNICAL REPORT

1 NOVEMBER 1989 — 31 JANUARY 1990

ISSUED 22 AUGUST 1990

LEXINGTON   MASSACHUSETTS

ABSTRACT

This report covers in detail the research work of the Solid State Division at Lincoln Laboratory for the period 1 November 1989 through 31 January 1990. The topics covered are Electrooptical Devices, Quantum Electronics, Materials Research, Submicrometer Technology, Microelectronics, and Analog Device Technology. Funding is provided primarily by the Air Force, with additional support provided by the Army, DARPA, Navy, SDIO, NASA, and DOE.

Accession For	
NTIS GRA&I	☒
DTIC TAB	☐
Unannounced	☐
Justification	
By	
Distribution/	
Availability Codes	
Dist	Avail and/or Special
A-1	

TABLE OF CONTENTS

LIST OF ILLUSTRATIONS

LIST OF TABLES

INTRODUCTION

1. ELECTROOPTICAL DEVICES

Monolithically integrated reduced-confinement antennas have been fabricated by grading the wafer surface temperature during molecular beam epitaxial growth to produce a longitudinal variation in the refractive index and thickness of the waveguide film. Reductions of > 35 percent were achieved in the far-field beam divergence for radiation emitted from single-mode GaAlAs slab waveguides, yielding far-field beams as narrow as 8.2° full width at half-maximum along the direction perpendicular to the wafer surface.

An impedance-matched lumped-element interferometric modulator for 1.3-μm operation has been demonstrated in LiNbO$_3$. A V_π of 2.6 V and bandwidth of 220 MHz was achieved at 1.3 GHz with an electrode length of only 5 mm.

2. QUANTUM ELECTRONICS

New results have been obtained on a 10-Hz Ti:Al$_2$O$_3$ master-oscillator/power-amplifier system designed for operation from 750 to 850 nm. This laser produced 200-ns, single-frequency, near-diffraction-limited, 0.38-J pulses at 800 nm.

A diode-pumped Nd:YAG laser has been demonstrated using self-starting additive-pulse mode locking with a nonlinear external cavity. Pulse durations of 1.7 ps were generated at an average output power of 25 mW without the need for active amplitude or phase modulation.

Three diode laser arrays have been coupled to a multimode fiber with 52 percent efficiency using geometric multiplexing. Calculations show it should be possible to couple tens of watts efficiently from diode arrays into a fiber.

Experiments have been carried out with LiB$_3$O$_5$, a recently discovered nonlinear optical material, to determine the temperature and thermal bandwidth for noncritically phase-matched frequency doubling of 1.06- and 1.32-μm radiation and for frequency summing 1.06- and 1.32-μm radiation. The intrinsic optical absorption of LiB$_3$O$_5$ was also measured and was found to be extremely low ($10^{-3} < \alpha < 2 \times 10^{-3}$ cm^{-1}) at 0.532, 1.06 and 1.32 μm.

The use of mechanical beam steering to decrease the thermal load on a nonlinear crystal in optical mixing has been demonstrated at low power. Essentially constant intensity harmonic radiation (0.532 μm) was generated while rapidly scanning the fundamental radiation (1.06 μm) through a 2-cm^{-1} diam. circle in a 3-cm-long LiIO$_3$ crystal.

3. MATERIALS RESEARCH

Graded-index separate-confinement heterostructure InGaAs/AlGaAs single-quantum-well diode lasers with a strained active layer have been fabricated from structures grown by organometallic vapor phase

epitaxy (OMVPE). Under pulsed operation, threshold current densities as low as 65 A/cm^2, the lowest ever reported for semiconductor lasers, have been obtained for a cavity length of 1500 μm.

The growth rate of GaAs by OMVPE has been measured as a function of substrate temperature, trimethyl-gallium (TMG) flow rate, and TMG exposure time for the procedure in which the substrate is exposed to arsine and TMG alternately rather than simultaneously. Atomic layer epitaxy (ALE), in which one monolayer of GaAs is deposited during each arsine/TMG cycle, has been accomplished over the temperature range from 425 to 475°C by varying the exposure time at a fixed flow rate, although the ALE process is not self-limiting over the parameter space investigated.

4. SUBMICROMETER TECHNOLOGY

Plasma-enhanced chemical vapor deposition has been used to deposit planarizing layers of amorphous carbon in order to overcome depth-of-focus limitations in high-resolution photolithography. The low-viscosity films reduced the deviation from planarity of 1.5-μm-deep, 400-μm-wide silicon dioxide wells to less than 0.2 μm.

Homoepitaxial diamond films have been grown by thermal decomposition of a mixture of hydrogen and acetone. Device quality morphology and electrical resistivity were obtained, and were shown to depend on the crystalline orientation of the substrate and on the amount of added $B(OCH_3)_3$, the latter serving as a source of boron dopants.

5. MICROELECTRONICS

A semiquantitative energy-band model has been developed to explain measurements of GaAs grown by molecular beam epitaxy at a substrate temperature of 200°C. The dominant feature of the model is a very high density of deep EL2-like levels 0.75 eV below the conduction band edge of GaAs.

The effects of nonuniform doping along the direction of current flow on the large-signal performance of Si permeable base transistors have been investigated. A class A power analysis, performed using simulated current-voltage characteristics, shows that output power, power-added efficiency, and large-signal gain can be increased by using nonuniform doping profiles.

A full-fill-factor CCD imager with integrated analog signal processors has been designed and fabricated. By combining charge-domain analog signal processors in a parallel, pipelined architecture, a device that performs a simple edge-detection algorithm in real time has been realized.

6. ANALOG DEVICE TECHNOLOGY

A novel method to measure substrate temperature during thin-film deposition has been developed using Au-Pt-Pd thermocouple wires bonded directly onto substrates. These thermocouples were evaluated in a specially designed vacuum oven at 775°C and show accuracy and stability to 1°C.

Y-Ba-Cu-O films have been deposited using *in situ* sputtering from single targets. These films have sharp transitions to the superconducting state at 85 K, critical currents higher than 1.4×10^7 A/cm^2 at 4.2 K and 2.3×10^5 A/cm^2 at 77, and an RF surface resistance of 1.2×10^{-5} Ω at 4.2 K and 1.2 GHz.

A four-pole Chebyshev microstrip filter has been demonstrated using both postannealed and *in-situ*-grown thin films of YBaCuO. The bandpass filters, which were designed for a 4-GHz center frequency and a 3-percent bandwidth, function at 77 K with a passband insertion loss as low as 0.3 dB, a dramatic improvement over the 2.5-dB loss of a normal-metal filter at the same temperature.

REPORTS ON SOLID STATE RESEARCH

1 November 1989 through 31 January 1990

PUBLISHED REPORTS

Journal Articles

JA No.

5592	Ion Implantation in III-V Semiconductors	J.P. Donnelly	In *III-V Semiconductor Materials and Devices,* edited by R.J. Malik (Elsevier, Amsterdam, 1989), p. 331
6125	Submicrometer Near-Intrinsic Thin-Film SOI Complementary MOSFET's	C-T. Lee K.K. Young	IEEE Trans. Electron Devices **36**, 2537 (1989), DTIC AD-A216666
6218	Structural Properties of As-Rich GaAs Grown by MBE at Low Temperature	M. Kaminska* Z. Liliental-Weber* E.R. Weber* T. George* J.B. Kortright* F.W. Smith B-Y. Tsaur A.R. Calawa	Appl. Phys. Lett. **54**, 1881 (1989)
6222	Possible Observation of a Spin-Density Wave in La_2CuO_4 by Raman Scattering	H.J. Zeiger A.J. Strauss G. Dresselhaus* Y.C. Liu* P.J. Picone* M.S. Dresselhaus*	Phys. Rev. B **40**, 8891 (1989)
6250	High-Sensitivity Lumped-Element Bandpass Modulators in $LiNbO_3$	G.E. Betts L.M. Johnson C.H. Cox, III	J. Lightwave Technol. **7**, 2078 (1989)
6277	Wavelength-Independent Faraday Isolator	P.A. Schulz	Appl. Opt. **28**, 4458 (1989)

---

* Author not at Lincoln Laboratory.

* Author not at Lincoln Laboratory.

6323	External-Cavity Coherent Operation of InGaAsP Buried-Heterostructure Laser Array	V. Diadiuk Z.L. Liau J.N. Walpole J.W. Caunt R.C. Williamson	Appl. Phys. Lett. **55**, 2161 (1989), DTIC AD-A217422
6343	A Passively Mode-Locked Ti:Al_2O_3 Laser Using a Nonlinear Coupled Cavity	J. Goodberlet* J. Wang* J.G. Fujimoto* S.R. Henion P.A. Schulz	Opt. News **15**, 8 (1989)
6347	Gain-Switched Pulsed Operation of Microchip Lasers	J.J. Zayhowski J. Ochoa A. Mooradian	Opt. Lett. **14**, 1318 (1989)
6350	Reduced-Confinement Antennas for GaAlAs Integrated Optical Waveguides	D.E. Bossi W.D. Goodhue M.C. Finn K. Rauschenbach J.W. Bales R.H. Rediker	Appl. Phys. Lett. **56**, 420 (1990)
6357	External-Cavity Diode Lasers with High Brightness and High Spectral Purity	W.F. Sharfin A. Mooradian	In *Laser Spectroscopy*, edited by M.S. Feld, J.E. Thomas, and A. Mooradian (Academic Press, Boston, 1989), p. 236
6363	Sequential Ar-O_2 Sputtering of Y_2O_3, BaF_2, and CuO Targets for Preparation of Y-Ba-Cu-O Super-conducting Films Without Wet-O_2 Annealing	M. Bhushan A.J. Strauss M.C. Finn	Appl. Phys. Lett. **55**, 2438 (1989), DTIC AD-A217508
6370	High-Performance, Externally Modulated Analog Fiber-Optic Links	C.H. Cox, III G.E. Betts L.M. Johnson	Opt. News **15**, 43 (1989)
6386	GaInP Mass Transport and GaInP/GaAs Buried Heterostructure Lasers	S.H. Groves Z.L. Liau S.C. Palmateer J.N. Walpole	Appl. Phys. Lett. **56**, 312 (1990)

* Author not at Lincoln Laboratory.

Meeting Speeches

MS No.

8023	Selective-Area Laser Photo-deposition of Transparent Conductive SnO_2	R.R. Kunz M. Rothschild D.J. Ehrlich	Materials Research Society Symposium Proc. **129,** Boston, Massachusetts, 28-31 November 1988, p. 447
8035	UV Enhancement of Surface Catalytic Polymerization of Ethylene	P.V. Purohit M. Rothschild D.J. Ehrlich	Materials Research Society Symposium Proc. **129,** Boston, Massachusetts, 28-31 November 1988, p. 259, DTIC AD-A217566
8059	Some Applications of Ion Beams in III-V Compound Semiconductor Device Fabrication	J.P. Donnelly K.K. Anderson J.D. Woodhouse W.D. Goodhue D. Yap M.C. Gaidis C.A. Wang	Materials Research Society Symposium Proc. **144,** Boston, Massachusetts, 28-31 November 1988, p. 421
8069	Excimer Laser Projection Lithography: Optical Considerations	D.J. Ehrlich M. Rothschild	Microelectron. Eng. **9,** 27 (*1989*)
8072	Sidegating Reduction for GaAs Integrated Circuits by Using a New Buffer Layer	F.W. Smith C.L. Chen G.W. Turner M.C. Finn L.J. Mahoney M.J. Manfra A.R. Calawa	Proc. Intl. Electron Devices Meeting, San Francisco, California, 11-14 December 1988, p. 838
8262A	Passive Mode Locking of a $Ti:Al_2O_3$ Laser with a Nonlinear Coupled Cavity	J. Goodberlet* J. Wang* J.G. Fujimoto* P.A. Schulz S.R. Henion	Proc. OSA Topical Meeting on Tunable Solid State Lasers, North Falmouth, Massachusetts, 1-3 May 1989, p. 16

---

* Author not at Lincoln Laboratory.

8265	A Theoretical and Experimental Comparison of Directly and Externally Modulated Fiber-Optic Links	C.H. Cox, III L.M. Johnson G.E. Betts	1989 IEEE MTT-S Intl. Micro-wave Symposium Digest II, Long Beach, California, 13-15 June 1989, p. 689, DTIC AD-A209967
8317	Excited-State Absorption in Ti:YAlO$_3$	K.F. Wall R.L. Aggarwal C.P. Khattak*	Proc. OSA Topical Meeting on Tunable Solid State Lasers, North Falmouth, Massachusetts, 1-3 May 1989, p. 238
8321	Large-Area Uniform OMVPE Growth for GaAs/AlGaAs Quantum-Well Diode Lasers with Controlled Emission Wavelength	C.A. Wang H.K. Choi M.K. Connors	J. Electron. Mater. **18,** 695 (1989)
8531	Schottky-Barrier Infrared Detec-tors and Focal Plane Arrays	B-Y. Tsaur	Proc. 1989 Intl. Electronic Imaging Exposition and Confer-ence, Boston, Massachusetts, 2-5 October 1989, p. 600

* * * * *

UNPUBLISHED REPORTS

Journal Articles

JA No.

| 6046 | PtSi Schottky-Barrier Focal Plane Arrays for Multispectral Imaging in Ultraviolet, Visible, and Infrared Spectral Bands | B-Y. Tsaur
C.K. Chen
J.P. Mattia | Accepted by IEEE Electron Device Lett. |
| 6322 | Low-Temperature Laser-Deposi-tion of Tungsten by Silane- and Disilane-Assisted Reactions | J.G. Black
S.P. Doran
M. Rothschild
D.J. Ehrlich | Accepted by Appl. Phys. Lett. |

---

* Author not at Lincoln Laboratory

6336	Programmable, Four-Channel, 128-Sample, 40-Ms/s Analog-Ternary Correlator	S.C. Monroe D.R. Arsenault K.E. Thompson A.L. Lattes	Accepted by IEEE J. Solid-State Circuits
6352	The Extinction Ratio in Optical Two-Guide Coupler $\Delta\beta$ Switches with Asymmetric Detuning	J.P. Donnelly L.A. Molter* G.S. Hopcraft* R.E. Smith* H.A. Haus*	Accepted by IEEE J. Quantum Electron.
6367	Reduced-Confinement GaAlAs Tapered Waveguide Antenna Grown by Molecular Beam Epitaxy	W.D. Goodhue D.E. Bossi M.C. Finn R.H. Rediker J.W. Bales	Accepted by J. Vac. Sci. Technol. B
6368	Femtosecond Measurements of the Nonresonant Nonlinear Index in AlGaAs	M.J. LaGasse* K.K. Anderson C.A. Wang H.A. Haus* J.G. Fujimoto*	Accepted by Appl. Phys. Lett.
6384	Calculation of the Intersubband Absorption Strength in Ellipsoidal Valley Quantum Wells	E.R. Brown S.J. Eglash	Accepted by Phys. Rev. B
6393	Observation of Maker Fringes and Estimation of $\chi^{(3)}$ Using Picosecond Nondegenerate Four-Wave Mixing in AlGaAs Waveguides	H.Q. Le D.E. Bossi K.B. Nichols W.D. Goodhue	Accepted by Appl. Phys. Lett.
6403	Gimbal for Aligning Laser and Lenslet Arrays for Coherent Operation in an External Cavity	J.W. Caunt V. Diadiuk	Accepted by Appl. Opt.
6405	GaInAsP/InP Buried-Heterostructure Surface-Emitting Diode Laser with Monolithic Integrated Bifocal Microlens	Z.L. Liau J.N. Walpole L.J. Missaggia D.E. Mull	Accepted by Appl. Phys. Lett.

* Author not at Lincoln Laboratory.

Meeting Speeches*

---

* Titles of meeting speeches are listed for information only. No copies are available for distribution.
† Author not at Lincoln Laboratory.

MS No.

8475	Visible-Wavelength Laser Photo-deposition of Cobalt Interconnects	M. Rothschild J.H.C. Sedlacek D.J. Ehrlich D.C. Shaver S.M. Bittenson* D. Edwards, Jr.* N.P. Economou*	
8491	Modeling of Localized Melting of Thin Si Films in Zone-Melting-Recrystallization	J.S. Im* J.D. Lipman* I.N. Miaoulis* C.K. Chen C.V. Thompson*	1989 Fall Meeting of the Materials Research Society, Boston, Massachusetts, 27 November-2 December 1989
8495	Measurements of the Surface Resistance of HTS Thin Films from 0.5 to 40 GHz	J. Steinbeck* D.E. Oates A.C. Anderson	
8759	Nuclear Magnetic Resonance Spectroscopy in the Study of Diamond Thin Films	K.M. McNamara* K.K. Gleason* M.W. Geis	
8402C, E	Homoepitaxial Diamond Films	M.W. Geis	IEEE Electron Device Society, Meeting, Boston Chapter, Lincoln Laboratory, Lexington, Massachusetts, 13 December 1989; Seminar, University of Southern California, Los Angeles, California, 26 January 1990
8445A	Optical Interconnections	D.Z. Tsang	IEEE/Lasers and Electro-optics Society Meeting, Dallas Chapter, Dallas, Texas, 15 November 1989
8452A	Solid State Laser Radars	A. Sanchez	
8485	Advances in Diode Laser Pumped Solid-State Lasers	T.Y. Fan	Lasers '89, New Orleans, Louisiana, 3-8 December 1989
8702	Two-Dimensional Semiconductor Diode Laser Arrays	J.N. Walpole	

* Author not at Lincoln Laboratory.

MS No.

8460	External-Cavity Coherent Operation of InGaAsP Buried-Heterostructure Laser Array	V. Diadiuk Z.L. Liau J.N. Walpole J.W. Caunt	
8551	Fabrication of Microlenses in Compound Semiconductors and Monolithic Integration with Diode Lasers	Z.L. Liau J.N. Walpole V. Diadiuk D.E. Mull L.J. Missaggia	SPIE OE/LASE'90, Los Angeles, California, 14-19 January 1990
8534A	Optical Interconnections for Digital Systems	D.Z. Tsang	Computer Society Meeting, Dallas, Texas 15 November 1989
8558A	Superconductive Microwave Devices and Circuits	R.S. Withers	IEEE Aerospace and Electronic Systems Society Meeting, Boston Chapter, Wayland, Massachusetts, 14 December 1989
8558B	Superconductive Microwave Devices and Circuits	R.S. Withers	Seminar on Microwaves and Electronics, University of Massachusetts, Amherst, Massachusetts, 7 December 1989
8563A	Analog Signal Correlator Design and Operation	J.B. Green	Hitachi Central Research Laboratory, Tokyo, Japan 5 December 1989
8588	High-T_c Superconducting Analog Circuits	R.W. Ralston	2nd Intl. Symposium on Superconductivity, Tsukuba, Ibaraki, Japan, 14-17 November 1989
8622	CCD Sensors for Space Surveillance	B.E. Burke D. Harrison	RADC Electro-optical Space Surveillance Conference, Griffiss AFB, New York, 14-16 November 1989

MS No.

| 8647 | Bulk Growth of InP Crystals | G.W. Iseler | American Association for Crystal Growth Evening Meeting, Bridgewater, New Jersey, 30 November 1989 |
| 8656 | Silylation Processes for 193-nm Excimer Laser Lithography | M.A. Hartney | IEEE Workshop on Lithography, New Orleans, Louisiana, 29 January 1990 |

ORGANIZATION

SOLID STATE DIVISION

A.L. McWhorter, *Head*
I. Melngailis, *Associate Head*
E. Stern, *Associate Head*
J.F. Goodwin, *Assistant*

D.J. Ehrlich, *Senior Staff*
N.L. DeMeo, Jr., *Associate Staff*
J.W. Caunt, *Assistant Staff*

SUBMICROMETER TECHNOLOGY

D.C. Shaver, *Leader*
M. Rothschild, *Assistant Leader*

Astolfi, D.K.	Hartney, M.A.
Craig, D.M.	Horn, M.W.
Dennis, C.L.	Kunz, R.R.
Doran, S.P.	Lyszczarz, T.M.
Efremow, N.N., Jr.	Maki, P.A.
Forte, A.R.	Melngailis, J.[†]
Gajar, S.A.*	Pang, S.W.
Geis, M.W.	Sedlacek, J.H.C.
Goodman, R.B.	Uttaro, R.S.

QUANTUM ELECTRONICS

A. Mooradian, *Leader*
P.L. Kelley, *Associate Leader*
A. Sanchez-Rubio, *Assistant Leader*

Aggarwal, R.L.	Jeys, T.H.
Barch, W.E.	Korn, J.A.
Belanger, L.J.	Lacovara, P.
Cook, C.C.	Le, H.Q.
Daneu, V.	Menyuk, N.[†]
DeFeo, W.E.	Nabors, C.D.
DiCecca, S.	Ochoa, J.R.
Dill, C.D., III	Schulz, P.A.
Fan, T.Y.	Seemungal, W.A.
Hancock, R.C.	Sharfin, W.F.
Henion, S.R.	Sullivan, D.J.
Hotaling, T.C.	Wall, K.F.
Hsu, L.*	Zayhowski, J.J.

ELECTRONIC MATERIALS

A.J. Strauss, *Leader*
B-Y. Tsaur, *Associate Leader*
H.J. Zeiger, *Senior Staff*

Anderson, C.H., Jr.	Eglash, S.J.	McGilvary, W.L.
Button, M.J.	Fahey, R.E.	Nechay, B.A.
Chen, C.K.	Finn, M.C.	Nitishin, P.M.
Choi, H.K.	Iseler, G.W.	Pantano, J.V.
Clark, H.R., Jr.	Kolesar, D.F.	Tracy, D.M.
Connors, M.K.	Krohn, L., Jr.	Turner, G.W.
Delaney, E.J.	Mastromattei, E.L.	Wang, C.A.
	Mattia, J.P.*	

---

* Research Assistant
[†] Part Time

APPLIED PHYSICS

R.C. Williamson, *Leader*
D.L. Spears, *Assistant Leader*
R.H. Rediker, *Senior Staff*

Aull, B.F.
Bailey, R.J.
Barwick, D.S.*
Betts, G.E.
Bossi, D.E.*
Corcoran, C.J.*
Cox, C.H., III
Diadiuk, V.
Donnelly, J.P.
Ferrante, G.A.
Groves, S.H.
Harman, T.C.
Hovey, D.L.
Johnson, L.M.
Liau, Z.L.

Lind, T.A.
Missaggia, L.J.
Mull, D.E.
O'Donnell, F.J.
Palmacci, S.T.
Palmateer, S.C.
Pheiffer, B.K.*
Rauschenbach, K.
Reeder, R.E.
Roussell, H.V.
Shiple, S.D.*
Tsang, D.Z.
Walpole, J.N.
Woodhouse, J.D.
Yee, A.C.

ANALOG DEVICE TECHNOLOGY

R.W. Ralston, *Leader*
R.S. Withers, *Associate Leader*
T.C.L.G. Sollner, *Assistant Leader*
R.M. Lerner, *Senior Staff*[†]

Anderson, A.C.
Arsenault, D.R.
Bhushan, M.
Boisvert, R.R.
Brogan, W.T.
Denneno, A.P.
Fitch, G.L.
Green, J.B.
Hamm, J.M.
Holtham, J.H.
Lattes, A.L.
Lichtenwalner, D.J.*

Lyons, W.G.
Macedo, E.M., Jr.
Minnick, R.G.
Munroe, S.C.
Oates, D.E.
Sage, J.P.
Seaver, M.M.
Shih, B.S.*
Slattery, R.L.
Westerheim, A.C.*
Whitley, D.B.
Yu-Jahnes, L-S.*

MICROELECTRONICS

R.A. Murphy, *Leader*
E.D. Savoye, *Associate Leader*
B.B. Kosicki, *Assistant Leader*
R.W. Chick, *Senior Staff*

Actis, R.
Bales, J.W.*
Bergeron, N.J.
Bozler, C.O.
Brown, E.R.
Burke, B.E.
Calawa, A.R.
Chen, C.L.
Chiang, A.M.
Chuang, M.L.*
Clifton, B.J.
Cooper, M.J.
Crenshaw, D.L.*
Daniels, P.J.
Doherty, C.L., Jr.
Dolat, V.S.

Donahue, T.Y.
Durant, G.L.
Felton, B.J.
Gladden, D.B.‡
Goodhue, W.D.
Gray, R.V.
Gregory, J.A.
Hollis, M.A.
Huang, C.M.
Hurley, E.T.
Johnson, B.W.
Johnson, K.F.
LaFranchise, J.R.
Lincoln, G.A., Jr.
Mahoney, L.J.
Manfra, M.J.
Mathews, R.H.

McGonagle, W.H.
McIntosh, K.A.
McMorran, R.A.
Mountain, R.W.
Nichols, K.B.
Parker, C.D.
Percival, K.A.
Pichler, H.H.
Rabe, S.
Rathman, D.D.
Reich, R.K.
Reinold, J.H., Jr.
Smith, F.W.*
Vera, A.
Wilde, R.E.
Young, D.J.

---

* Research Assistant
[†] Part Time
‡ Staff Associate

1. ELECTROOPTICAL DEVICES

1.1 REDUCED-CONFINEMENT ANTENNAS FOR GaAlAs INTEGRATED OPTICAL WAVEGUIDES

Integrated optoelectronic circuits frequently incorporate components such as electrooptic modulators and Y-junctions that require waveguides with a small mode size for efficient device operation. When coupling into free space, however, a large mode size is desirable at the device output endface in order to obtain a highly directional far-field beam. Optical horn antennas, for example, have been used to produce a lateral increase in the size of a guided mode, thereby reducing the lateral far-field beam divergence [1,2]. Preliminary results are described on monolithically integrated reduced-confinement GaAlAs waveguide antennas potentially capable of increasing the size of a guided mode in both the transverse and lateral dimensions. The concept of a reduced-confinement antenna has been applied at microwave frequencies since the 1940s in the dielectric polyrod antenna [3]. More recently, similar structures have been demonstrated at optical frequencies both in sir :le-mode fibers [4] and in Ti:LiNbO$_3$ waveguides [5] for fiber coupling.

We have produced these antennas for use at GaAs laser wavelengths, e.g., 0.88 μm, using a novel molecular beam epitaxy (MBE) growth technique [6,7]. This method allows us to grow a single-mode structure in which a tapered waveguide film, varying longitudinally in both thickness and Al concentration, is sandwiched between two uniform lower-index cladding layers. Near the output endface of the waveguide, the transverse confinement of the guided mode is reduced by decreasing the film thickness and, what is more important, by decreasing the refractive index difference between the film and cladding layers. Using this structure, we have obtained reductions of > 35 percent in the transverse far-field beam divergence for radiation emitted from single-mode slab waveguides.

A reduced-confinement antenna is shown schematically in Figure 1-1. The details of the MBE growth technique used to produce this device are as follows. The GaAs substrate wafer is bonded with indium to a mounting block which has a top surface that is slightly recessed in several regions [6]. The regions of the wafer that are in direct thermal contact with the unrecessed portions of the mounting block are conductively heated, while the regions that are located above a recess are radiatively heated. The radiatively heated regions have a lower surface temperature than the conductively heated regions. For surface temperatures below 650°C, the sticking coefficients of both Ga and Al on GaAs are essentially independent of temperature. Above 650°C, however, the sticking coefficient of Ga decreases continuously with increasing temperature [8,9], and this results in increased Al concentrations and decreased growth rates for GaAlAs films grown by MBE at successively higher temperatures. Thus, for surface temperatures greater than 650°C, a temperature gradient across the wafer surface produces a spatial variation in the relative amounts of Ga and Al that are incorporated into the waveguide film, as well as a spatial variation in the waveguide film thickness.

For the device shown in Figure 1-1, a uniform 1.8-μm-thick Ga$_{0.785}$Al$_{0.215}$As lower cladding layer is first grown at temperatures between ~ 555 and 580°C, for which the sticking coefficients are nsensitive to growth-temperature variations. The temperature of the mounting block is then increased and a tapered GaAlAs waveguide film is grown. For the film shown in Figure 1-1, the substrate surface temperature ranges from ~ 680 to 720°C. The resulting waveguide film varies from 0.52-μm-thick
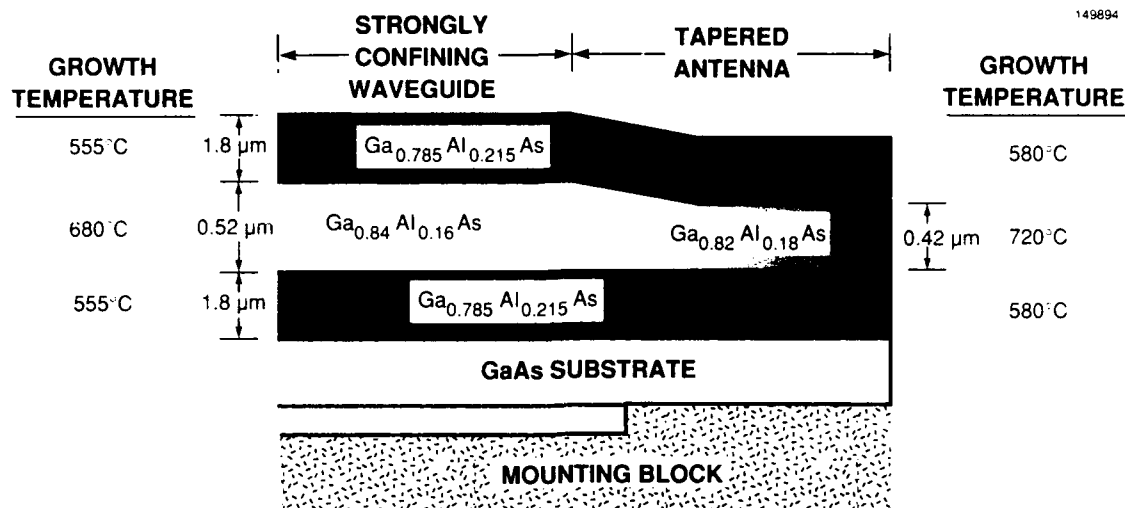
Figure 1-1. Cross-sectional profile of a reduced-confinement GaAlAs tapered slab-waveguide antenna. The material compositions and film thicknesses were measured by Auger electron spectroscopy.

$Ga_{0.84}Al_{0.16}As$ in the cooler region to 0.42-μm-thick $Ga_{0.82}Al_{0.18}As$ in the warmer region. Finally, the mounting block temperature is reduced to ~ 580°C and an upper cladding layer, identical in composition and thickness to the lower cladding layer, is grown. The layer thicknesses and compositions, which are indicated in Figure 1-1, were measured by Auger electron spectroscopy. The length of the tapered transition is between 1 and 2 mm using current growth procedures; however, shorter taper lengths should be obtained through the use of more sophisticated techniques to produce the substrate temperature gradient, such as laser heating.

The tapered slab-waveguide antenna shown in Figure 1-1 is designed for single-mode operation at a wavelength of 0.88 μm. In the cooler growth region, there is a difference of 0.055 in the AlAs mole fraction between the 0.52-μm-thick waveguide film and the cladding layers. The result is a strongly confining single-mode optical waveguide in this region, for which the confinement parameter, $V = kh(n^2 - n_c^2)^{1/2} = 1.45$, where k is the magnitude of the wave vector, h is the film thickness, and n_f and n_c are the refractive indices of the film and cladding, respectively. The region grown at higher substrate surface temperatures, however, exhibits a difference in AlAs mole fraction of only 0.035, and the waveguide film thickness is only 0.42 μm. Hence, this section of the waveguide is much less optically confining ($V = 0.93$).

The data points and dashed line in Figure 1-2(a) show the far-field intensity profile measured for the antenna of Figure 1-1 along the direction perpendicular to the wafer surface. For comparison, the measured far-field profile for a nontapered device that has a 0.52-μm-thick $Ga_{0.84}Al_{0.16}As$ waveguide film along its entire length is shown in Figure 1-2(b). Both measurements are for transverse-electric (TE) polarized light from a GaAs diode laser. Radiation from the tapered antenna waveguide exhibits a 10.0° full width at half-maximum (FWHM) far-field beam divergence, a 36-percent reduction from the 15.7° FWHM beam divergence obtained for the nontapered waveguide.

2
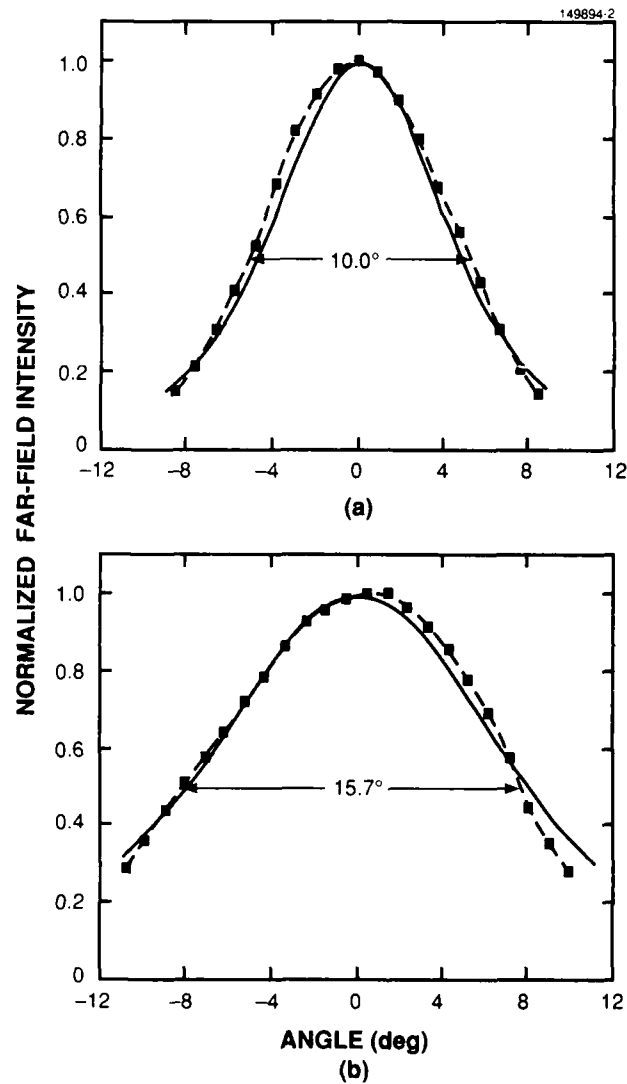
Figure 1-2.   Normalized far-field intensity profiles for (a) tapered (reduced-confinement) and (b) nontapered GaAlAs slab waveguides. The data points and dashed lines indicate the experimentally measured profiles, while the solid lines indicate the theoretically predicted profiles based on the Auger data.
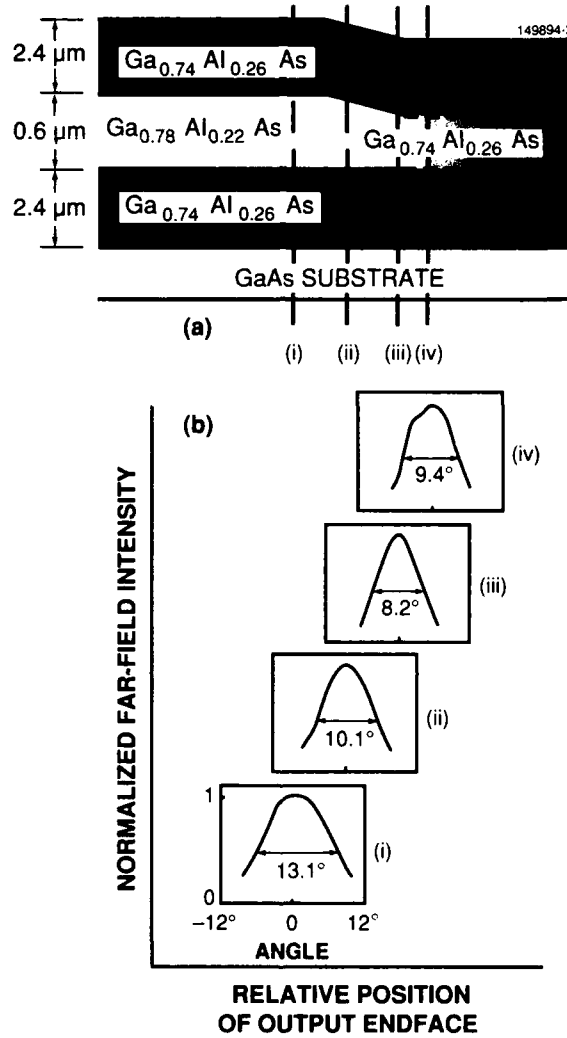
Figure 1-3.   (a) Cross-sectional profile of a reduced-confinement structure that tapers from a buried symmetric slab waveguide to uniform material. The dashed vertical lines indicate the locations of the cleaved output endfaces of samples (i) through (iv). (b) Experimentally measured far-field profiles for samples (i) through (iv).

4

Using Auger data for both the strongly confining and weakly confining regions of the waveguide in Figure 1-1, we have calculated the guided-mode parameters and electric-field amplitude profiles at the output endfaces of both the tapered and nontapered waveguide devices. According to these calculations, the width of the guided-mode intensity varies from 0.71 μm FWHM in the strongly confining waveguide region to 0.97 μm FWHM in the weakly confining structure, an increase of 37 percent. The analytically determined electric-field profiles at the device output endfaces are then propagated to the far field through a Fourier transform. The theoretically predicted far-field intensity profiles, which are shown by the solid lines in Figure 1-2, are in close agreement with the experimentally observed profiles.

To examine the limits on the performance of reduced-confinement antennas, we have grown the tapered-waveguide structure shown in Figure 1-3(a). This device tapers from a symmetric slab waveguide in the cooler growth region to uniform material (no waveguide structure) in the warmer growth region. The structure has been cleaved into a series of samples whose output endfaces intersect the waveguide antenna at various positions along the taper length, as indicated by the dashed vertical lines in Figure 1-3(a). The measured far-field profiles for these devices are shown in Figure 1-3(b). The non-tapered device (i) with its uniform 0.60-μm-thick $Ga_{0.78}Al_{0.22}As$ waveguide film, exhibits a $13.1°$ FWHM far-field beam divergence. As the location of the antenna endface progresses through the tapered transition, the divergence steadily decreases, eventually reaching a minimum value at (iii) of $8.2°$ FWHM. This $8.2°$ divergence is a 37-percent reduction from the divergence for the nontapered waveguide. The output endface of the longest sample (iv) lies beyond the tapered transition, in the region of the wafer where the structure is no longer guiding. The increase in the far-field divergence to $9.4°$ FWHM for this device is consistent with the expected leakage of the wave into the higher-index GaAs substrate.

The minimum beam divergence of $8.2°$ FWHM in Figure 1-3(b) can be interpreted as follows. As the GaAs laser radiation propagates through the tapered transition, the waveguide structure becomes significantly less confining and the width of the guided mode increases until it approaches 5.4 μm, the total thickness of the transparent guiding and cladding layers. The lower boundary of this transparent epitaxial window is the absorbing higher-index GaAs substrate. As a bench mark for comparison with our experimental measurements, we have calculated the theoretical far-field radiation profile for a 5.4-μm-wide slit that is uniformly illuminated by a plane wave. The central far-field lobe of this calculated $[(\sin x)/x]^2$ intensity pattern is $8.2°$ FWHM. Although the exact agreement is probably fortuitous, this result indicates that the observed $8.2°$ FWHM far-field beam divergence is consistent with the minimum beam divergence that can be expected for this particular device.

In conclusion, reductions of > 35 percent in the transverse far-field optical beam divergence have been achieved through the use of reduced-confinement GaAlAs tapered slab-waveguide antennas, which are produced using a novel MBE growth technique. Typically, beams emitted from GaAlAs waveguide and laser devices are highly divergent along the direction perpendicular to the wafer surface [10]. The one-dimensional reduced-confinement structure is not only effective in reducing this transverse beam divergence, but is also compatible with techniques for reducing the lateral beam divergence.

D.E. Bossi   W.D. Goodhue

M.C. Finn   K. Rauschenbach

J.W. Bales   R.H. Rediker

1.2   HIGH-SENSITIVITY 1.3-GHz BANDPASS INTERFEROMETRIC MODULATOR

Integrated optical modulators are a key component of externally modulated analog links [11]. In most cases, analog link performance can be improved by increasing the modulator sensitivity. In a previous report [12], we showed by analysis that impedance-matched lumped-element modulators can have significantly higher response than traveling-wave devices for a range of electrode lengths, depending on the modulation frequency. We have demonstrated an impedance-matched LiNbO$_3$ lumped-element interferometric modulator for operation at 1.3 μm. With an electrode length of 5 mm, the effective V$_\pi$ (the voltage change required for full on-off modulation) at 1.3 GHz is 2.6 V, which is much less than the estimated effective V$_\pi$ of 9.8 V for a traveling-wave device with the same electrode length.

A lumped-element interferometric intensity modulator, as illustrated in Figure 1-4, can be modeled electrically as a series RLC circuit. The capacitance is proportional to the electrode length. For small-signal sinusoidal modulation at the half-power point, the modulation depth is proportional only to the electrode current I and is independent of the electrode length. The electrode current and response of a lumped-element modulator are maximized by using a nondissipative matching circuit to couple all of the available RF power from the source to the electrode series resistance. Nondissipative matching from a 50-Ω source to a frequency-dependent complex electrode impedance can be achieved for bandpass applications. A conventional 50-Ω shunt-resistor matching circuit results in broadband performance but substantially reduces the peak modulator sensitivity.
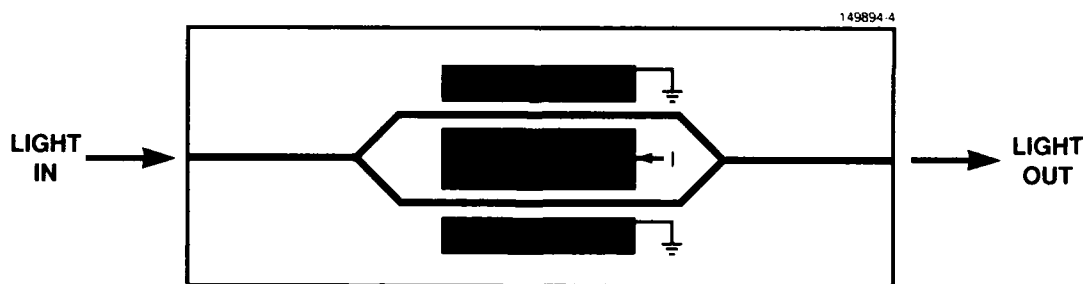
Figure 1-4.   Schematic illustration of an integrated-optical interferometric intensity modulator.

An experimental device was fabricated for single-mode 1.3-μm operation with TE polarization on Y-propagating X-cut LiNbO$_3$. The electrode length L was 5 mm and the V$_\pi$L product referring to the actual electrode voltage was 35 V-mm. An equivalent electrode RLC circuit was determined from S$_{11}$ measurements. At 1.3 GHz the electrode impedance is 3.8 – j11.5 Ω. With a matching circuit consisting only of a shunt inductance L$_m$ = 1.55 nH (Figure 1-5), 98 percent of the available power from a 50-Ω source at 1.3 GHz is delivered to the modulator.

The small-signal response shown in Figure 1-6 was measured using the swept-frequency technique on both the impedance-matched device and an identical broadband device with the shunt inductor

6
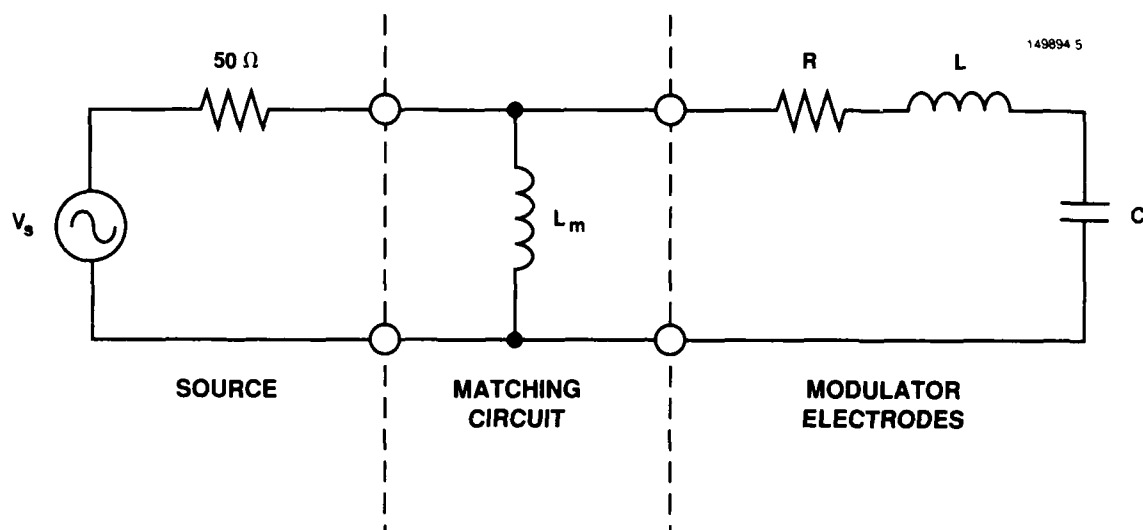
Figure 1-5. Equivalent circuit of the impedance-matched modulator showing the source, matching circuit, and electrode model. The electrode parameter values are R = 3.8 Ω, L = 3.2 nH, and C = 3.1 pF.
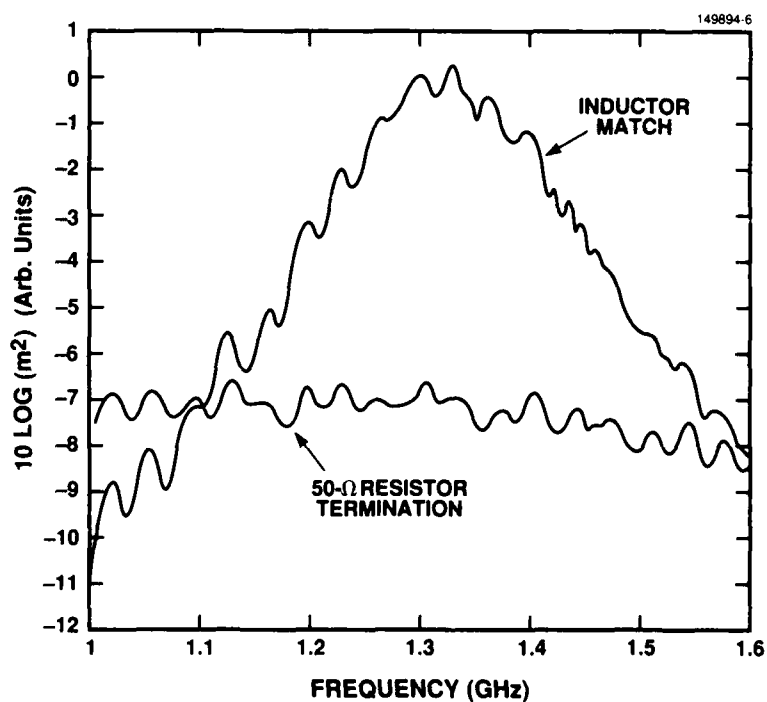
Figure 1-6. Measured small-signal modulation depth m of the impedance-matched and broadband modulators, for a fixed level of RF source power.

7

replaced by a 50-Ω resistive termination. For the matched and broadband devices, the results indicate that the effective V_π (from a 50-Ω source) at 1.3 GHz was 2.6 and 5.8 V and the 3-dB bandwidth was 220 MHz and 1.9 GHz, respectively. A comparable traveling-wave modulator with an effective V_π of 2.6 V at 1.3 GHz would require an electrode length of $\geq$ 19 mm.

<div align="right">
L.M. Johnson
H.V. Roussell
</div>

REFERENCES

1. A.F. Milton and W.K. Burns, *IEEE J. Quantum Electron.* **QE-13**, 828 (1977).

2. R.H. Rediker, T.A. Lind, and B.E. Burke, *J. Lightwave Technol.* **6**, 916 (1988).

3. G.E. Mueller and W.A. Tyrell, *Bell Syst. Tech. J.* **26**, 837 (1947).

4. S. Lacroix, R. Bourbonnais, F. Gonthier, and J. Bures, *Appl. Opt.* **25**, 4421 (1986).

5. P.G. Suchoski, Jr. and R.V. Ramaswamy, *J. Lightwave Technol.* **LT-5**, 1246 (1987).

6. W.D. Goodhue, J.J. Zayhowski, and K.B. Nichols, *J. Vac. Sci. Technol. B* **6**, 846 (1988).

7. D.E. Bossi, W.D. Goodhue, and R.H. Rediker, *Integrated and Guided-Wave Optics Tech. Dig.* (Optical Society of America, Washington, D.C., 1989), pp. 80-83.

8. R. Fischer, J. Klem, T.J. Drummond, R.E. Thorne, W. Kopp, H. Morkoç, and A.Y. Cho, *J. Appl. Phys.* **54**, 2508 (1983).

9. J. Ralston, G.W. Wicks, and L.F. Eastman, *J. Vac. Sci. Technol. B* **4**, 594 (1986).

10. B. Goldstein, M. Ettenberg, N.A. Dinkel, and J.K. Butler, *Appl. Phys. Lett.* **47**, 655 (1985).

11. G.E. Betts, L.M. Johnson, C.H. Cox, III, and S.D. Lowney, *IEEE Photon. Technol. Lett.* **1**, 404 (1989).

12. Solid State Research Report, Lincoln Laboratory, MIT (1989:2), p. 1.

2. QUANTUM ELECTRONICS

2.1 Ti:Al$_2$O$_3$ MASTER-OSCILLATOR/POWER-AMPLIFIER SYSTEM

We have designed, assembled, and operated a longitudinally pumped, multistage Ti:Al$_2$O$_3$ master-oscillator/power-amplifier system to produce pulsed (10 Hz), tunable radiation from 750 to 850 nm. We have obtained 200-ns, single-frequency output with 0.38 J/pulse at 800 nm. This system is composed of three major subsystems: (1) a CW Ti:Al$_2$O$_3$ master oscillator, (2) a Ti:Al$_2$O$_3$ amplifier and (3) frequency-doubled Nd:YAG pump lasers. In this report, the system architecture and some preliminary measurements are described.

The master oscillator, which is a CW Ti:Al$_2$O$_3$ single-frequency ring laser [1] pumped by a CW Ar-ion laser, can be tuned from ~ 750 to 850 nm. The Ti:Al$_2$O$_3$ laser operates in a TEM$_{00}$ mode, and a similar laser had a measured frequency stability of 2 MHz over a 10-s time interval. At the peak of the gain profile this oscillator provides a signal of ~ 0.5 W. A broadband isolator [2] consisting of a Faraday rotator and a compensating polarization rotator provides 30 dB of isolation over the tuning range of the master oscillator.

The Ti:Al$_2$O$_3$ amplifier consists of four stages: a four-pass preamplifier, a two-pass amplifier, a single-pass amplifier, and a final two-pass amplifier, as shown schematically in Figure 2-1. A broadband isolator is positioned between stages 1 and 2, and also between stages 2 and 3. Pockels cells between stages 1 and 2 are used to gate as well as to temporally shape the signal beam intensity. The pump lasers, described below, had a repetition rate of 10 Hz, which determined the pulse rate of the Ti:Al$_2$O$_3$ amplifier system.

Each amplifier stage consists of a Ti:Al$_2$O$_3$ crystal cut at Brewster's angle to minimize reflection losses. The signal and pump beams propagate almost collinearly (~ 1° difference) and are polarized along the c-axis of the crystal (p polarization) to maximize the gain. The length of each crystal is chosen so that > 95-percent of the pump beam is absorbed. Each stage is pumped using random binary phase plates (RBPP) [3] to smooth irregularities in the pump beam intensity profiles, and the pumping is from both sides to maximize the energy absorbed while avoiding damage.

The signal beam was observed to drift as a result of changes in the room environment, warm-up of the Ar-ion pump laser and Ti:Al$_2$O$_3$ master oscillator, and mechanical tuning of the master oscillator. The time scale of the drift caused by environmental and warm-up changes was on the order of minutes. To facilitate the signal-beam alignment, two-dimensional, position-sensing detectors with accuracy within 10 μm were used to ensure that any changes in the direction or position of the signal beam could be corrected using two mirrors. Two samples of the signal beam were obtained 1.55 m apart. The accuracy with which the beam position could be sensed resulted in an angular accuracy of ~ 7 μrad, which over a 10-m path length (the distance from the master oscillator to the output of the fourth amplifier stage) corresponds to a displacement of ~ 65 μm.

The preamplifier is schematically depicted in the lower portion of Figure 2-1. The signal beam makes four passes through the Ti:Al$_2$O$_3$ amplifier crystal and is coupled into and out of the preamplifier using a broadband isolator. At the completion of the second pass, the beam is reflected back onto itself

149894 7

OUTPUT

532-nm PUMP
BEAMS

TI:SAPPHIRE
CRYSTALS

SIGNAL
BEAM

2-PASS AMPLIFIER

SINGLE-PASS AMPLIFIER

ISOLATOR

ISOLATOR

2-PASS AMPLIFIER

POCKELS CELL

ISOLATOR

4-PASS AMPLIFIER

Figure 2-1.   Schematic of the Ti:Al$_2$O$_3$ master-oscillator/power-amplifier system.

from a mirror of 1-m focal length. At the completion of the fourth pass, the beam enters the broadband isolator and is then rejected by the isolator, which provides the output coupling. The average diameter of the signal beam in this stage is 1.5 mm. Lenses of 40-cm focal length and RBPP with elements 150 × 150 μm are used to produce a pump beam of 2-mm diameter at the face of the Ti:Al$_2$O$_3$ crystal. The preamplifier is pumped with a commercially available frequency-doubled, Q-switched Nd:YAG laser.

Pumping the Ti:Al$_2$O$_3$ preamplifier crystal with 225 mJ and using a CW signal-beam power of 180 mW (at λ = 800 nm), we have obtained 4- to 6-mJ, ~ 100-ns pulses. The four-pass gain calculated from these values is 2 to 3 × 10^5. Figure 2-2(a) shows a density plot of the beam profile at the output of the preamplifier, with the darker shading representing higher intensity. This profile was taken at a distance corresponding to the input to the second amplifier stage. Figure 2-2(b) shows Gaussian fits to the data taken through the centroid of the data along the horizontal and vertical axes. From the Gaussian fits, it is apparent that very little distortion of the signal beam occurs in the preamplifier.

(a)   (b)
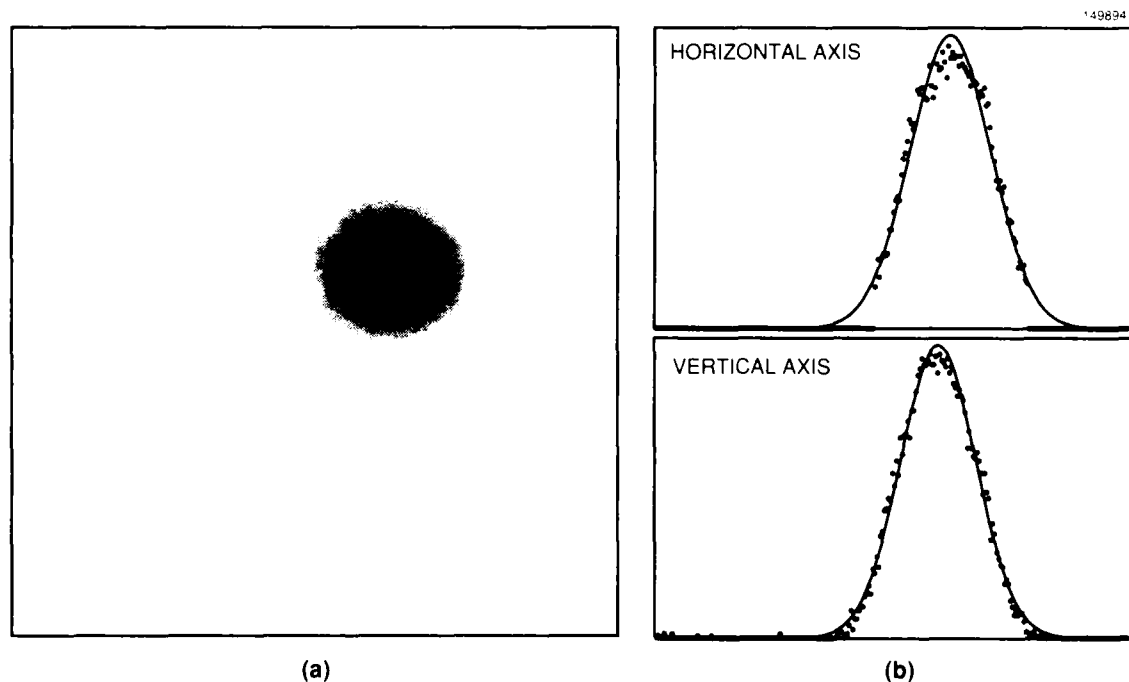
Figure 2-2.   Preamplifier output. (a) Density plot of the beam profile, with darker shading representing higher intensity. (b) Beam profiles along the horizontal and vertical axes taken through the centroid of the data (solid lines), with Gaussian fits to the data (dotted lines).

The power amplifier portion of the Ti:Al$_2$O$_3$ amplifier system consists of the remaining three amplifier stages. Prior to the second amplifier stage, the signal beam is expanded by 1.3 times. Between stages 2 and 3 the signal beam is expanded by 2.0 times and between stages 3 and 4 by 1.3 times. Table 2-1 lists the incident pump energy on each crystal face, the RBPP element dimensions, the focal length of the lens used to image the far field at the Ti:Al$_2$O$_3$ amplifier crystals, and the pump beam diameter ($1/e^2$) at the Ti:Al$_2$O$_3$ crystals for the four stages. It should be noted that the Ti:Al$_2$O$_3$ amplifier crystals are pumped from both sides, so the total pump energy for each crystal is twice the value shown. Typical signal-beam energies for stages 2 through 4 were 10 to 20, 40 to 80, and 300 to 350 mJ, respectively, depending on the alignment of the system.

TABLE 2-1

Incident Pump Energy, RBPP Element Dimensions, Lens Focal Length, and Pump Beam Diameter for the Four Amplifier Stages of the TiAl$_2$O$_3$ Amplifier System

Stage	Incident Pump Energy (mJ)	RBPP Element Dimensions (μm)	Focal Length of Lens (cm)	Pump Beam Diameter ($1/e^2$) at Crystal (mm)
1	113	150 × 150	40	1.99
2	188	100 × 100	40	2.98
3	338	75 × 75	40	3.97
4	525	75 × 75	50	4.97

The power amplifier is pumped with a custom Nd:YAG laser system consisting of a Q-switched mode-locked oscillator, a common three-stage amplifier chain, and four parallel two-stage power amplifier chains resulting in four output beams at 1.06 μm, as shown schematically in Figure 2-3. This pump system provides a macropulse 180 ns in duration consisting of 100-ps mode-locked pulses spaced 10 ns apart. The macropulse repetition rate is 10 Hz. The total average output power at $\lambda = 1.06$ μm was as high as 110 W. Frequency doubling of the pump radiation from 1.06 to 0.532 μm was accomplished using KD*P doubling crystals. The doubling efficiency achieved was as high as 38 percent, and was 30 percent routinely. Since the output of the custom Nd:YAG laser system is in the form of four separate laser beams, four separate frequency doublers were used.

12

Q-SWITCHED MODE-LOCKED Nd:YAG OSCILLATOR

☑|☐|☑ ISOLATOR   ([BEAM EXPANDER

█ AMPLIFIER   ✒ MIRROR

▯ POLARIZATION
   ROTATOR   ◥ BEAMSPLITTER
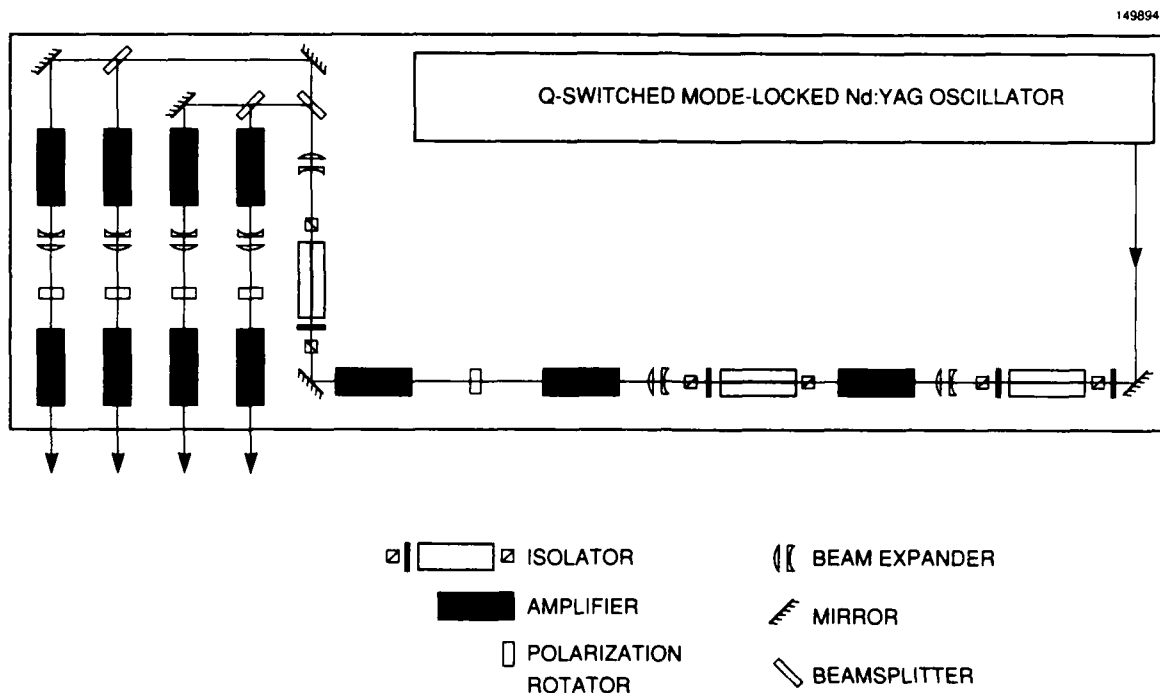
Figure 2-3. Schematic of the custom Nd:YAG pump laser system from which the power is delivered in four separate beams.

In summary, we have designed and constructed a Ti:Al$_2$O$_3$ master-oscillator/power-amplifier system, and pulse energies up to 380 mJ at λ = 800 nm have been obtained. Further measurements of wavelength tuning, near- and far-field beam profiles, and amplified spontaneous emission have been made and will be reported separately.

K.F. Wall   P. Lacovara
P.A. Schulz   A. Walther
R.A. Aggarwal   V. Daneu
A. Sanchez

2.2   SELF-STARTING PASSIVE MODE LOCKING OF A DIODE-PUMPED Nd:YAG LASER

The recent discovery of self-starting mode locking of a Ti:Al$_2$O$_3$ laser [4] by additive-pulse mode locking has led to speculation that other lasers might be mode locked in the same way. We have now achieved passive mode locking of a diode-pumped Nd:YAG laser using this technique, without the need for external amplitude or phase modulation. A stable train of 1.7-ps pulses is produced with an average output power of 25 mW. We believe that these are the shortest pulses generated in a mode-locked Nd^{3+} laser to date. These results demonstrate the viability of self-starting additive-pulse mode locking for ultrashort-pulse, diode-pumped solid state lasers.

A schematic diagram of the mode-locked, diode-pumped Nd:YAG laser is shown in Figure 2-4. The laser uses a novel diode-pumping scheme [5] that matches the pump spot size to the laser mode by combining beams to achieve more symmetric aperture filling. The Nd:YAG laser was pumped with three 0.5-W diode arrays that were temperature controlled to tune their emission wavelength to the Nd:YAG absorption band at 808 nm. Each laser array output was collimated, and the resulting beams were stacked in the dimension in which they were diffraction limited. By using a pair of orthogonal cylindrical lenses, the beams were focused into a 4-mm-long, antireflection-coated Nd:YAG crystal.
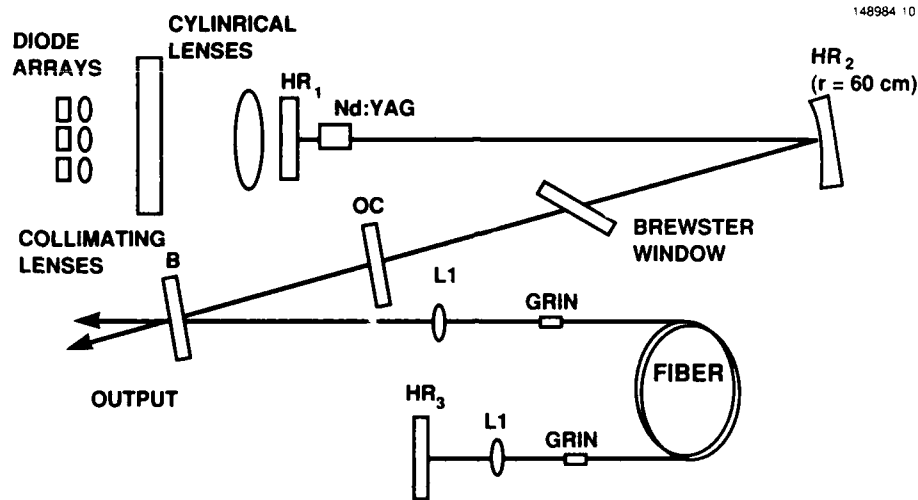
Figure 2-4.   Schematic of diode-pumped Nd:YAG laser. Three diode arrays are used as the pump source. The main laser cavity is formed by a high-reflecting end mirror (HR$_1$), a folding mirror (HR$_2$) with r = 60 cm, and an output coupler (OC). The external cavity consists of a beamsplitter (B), optical fiber, and retroreflecting mirror (HR$_3$).

The Nd:YAG main laser cavity consisted of a dichroic, flat end mirror with high reflectivity at 1.064 μm and high transmission at 810 nm, a spherical turning mirror (r = 60 cm), and a flat 14-percent transmitting mirror that functioned as the output coupler. Mirror separations were adjusted to obtain stable operation with an overall optical length of 1.09 m, corresponding to a round-trip frequency of 137 MHz. Since additive-pulse mode locking requires interference of the feedback from the external cavity with the main laser cavity, the polarization of the laser emission was controlled by a Brewster window placed inside the main laser cavity to obtain linear polarization. Without the external cavity, the Nd:YAG laser had a threshold of 670-mW diode-pump power and produced a maximum CW output of 250 mW at 1.1-W pump power.

The external coupled cavity was formed by a beamsplitter, optical fiber, and retroreflecting mirror. The fraction of the main laser output that was directed into the external cavity was determined by the beamsplitter. Measurements were performed using beamsplitter reflectivities of 90 or 70 percent. The light reflected from the beamsplitter was collimated with an 18-cm best-form lens before being coupled

into a single-mode optical fiber. In order to reduce stray reflections that would interfere with the self-starting mode locking process, the incident beam was coupled into the fiber using a graded-index lens (0.23 pitch) that was antireflection coated on one side and coupled to the fiber with index-matching fluid on the other. The fiber was single mode and had a core diameter of 7 μm. Typical coupling efficiency to the fiber was ~ 80 percent. An identical optical arrangement was used to couple out of the end of the fiber, and the resulting beam was retroreflected back through the fiber. The beam could also be retroreflected by a mirror placed in contact with the fiber end; however, the former arrangement was preferred because it was less susceptible to damage.

The choice of fiber length and intensity coupled into the fiber controls the nonlinear phase shift produced on the field in the external cavity, which in turn controls the magnitude of the intensity-dependent reflectivity. The nonlinear phase shift and hence the amplitude of the intensity-dependent reflectivity will scale as the product $n_2 I L_f$, where n_2 is the nonlinear index of refraction of the fiber, I is the intensity in the fiber, and L_f is the fiber length. Experiments confirmed that the intensity threshold for mode locking was inversely proportional to the fiber length.

Different fiber lengths ranging from 83 to 155 cm were used for these measurements. For a given fiber length, the time of flight of a pulse in the external cavity was adjusted to be an integral multiple of the time of flight in the main laser cavity. This ensured that pulses which were reinjected from the external cavity would be synchronized with pulses in the main cavity. A length adjustment to within 7 μm was required to maintain a timing mismatch less than 0.5 ps. The length of the external cavity was also adjusted with a piezoelectric translator (PZT) attached to one of the mirrors in order to interferometrically control the relative cavity lengths to within 0.1 μm.

Self-starting additive-pulse mode locking was achieved using the external cavity for a range of cavity parameters. The shortest pulses were obtained using a beamsplitter with 90-percent reflectivity and a fiber length of 83 cm with an external cavity length twice the main cavity length. The power coupled into the fiber (single pass) was 100 W and the output power was 25 mW. The threshold for observing the mode locking was approximately 80 to 100 mW of power coupled into the fiber. By appropriately adjusting the external cavity length, stable trains of pulses were generated. Figure 2-5 shows a background-free, second-harmonic autocorrelation trace of the pulse. The pulse duration is 1.7 ps full width at half-maximum (FWHM) assuming a sech pulse shape. The spectrum of the pulse was measured using a grating spectrometer and an optical multichannel analyzer. The FWHM of the bandwidth was 0.67 nm. Thus, the pulses had a time-bandwidth product of 0.30, which is at the Fourier limit.

Scaling of operating parameters can be carried out in order to evaluate design trade-offs between self-starting, output power, and pulse duration. Increasing the fiber length from 83 to 155 cm approximately doubles the nonlinear phase change at a given intensity. By using a beamsplitter with 90-percent reflectivity, the threshold for self-starting was reduced to 35 mW of power in the fiber. However, the pulse durations were increased to 2.3 ps because of dispersive broadening in the fiber. The increased nonlinear phase shift from the increased fiber length can also be traded off against the Q of the external cavity and the laser output power. Decreasing the reflectivity of the beamsplitter to 70 percent resulted in a self-starting threshold of 85 mW, which was comparable to the value obtained using an 83-cm fiber

15
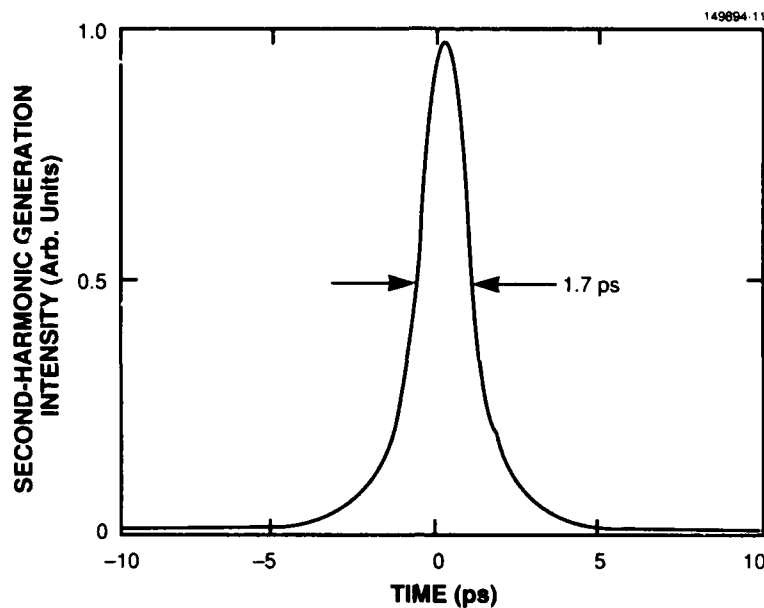
Figure 2-5. Autocorrelation of self-starting additive-pulse mode-locked laser output showing a pulse duration of 1.7 ps (assuming sech pulse shape).

with a beamsplitter reflectivity of 90 percent. However, operating at full power produced a 60-mW output compared with 25 mW for the former case. It should also be possible to increase the output power by decreasing loss other than from beamsplitter transmission in the external cavity.

In the limit of low dispersion, self-starting additive-pulse mode locking is analogous to fast saturable-absorber mode locking. For saturable-absorber mode locking, the pulse width is inversely proportional to the gain bandwidth, rather than inversely proportional to the square root of gain bandwidth as in active mode locking. Consequently, much shorter pulses are realizable for additive-pulse mode locking than for active mode locking. Even shorter pulse durations can be anticipated in Nd:YLF or Nd:glass where the gain bandwidth is broader.

J. Goodberlet*   J. Jacobsen*

J.G. Fujimoto*   T.Y. Fan

P.A. Schulz

*Department of Electrical Engineering and Computer Science and Research Laboratory of Electronics, Massachusetts Institute of Technology, Cambridge, Massachusetts.

2.3 EFFICIENT COUPLING OF MULTIPLE DIODE LASER ARRAYS TO AN OPTICAL FIBER

While diode lasers are efficient sources of radiation, methods of coupling these devices to an optical fiber have been inadequate. Here, we demonstrate that three high-power diode arrays can be efficiently coupled to a multimode optical fiber by geometric multiplexing [5]. In principle, many more than three arrays can be used and tens of watts of power could be obtained from a single fiber with incoherent multiple-diode-array input, which should allow diode lasers to be used in applications that require high power and a convenient delivery system.

A schematic of an experiment using three commercial GaAlAs diode laser arrays is shown in Figure 2-6. Each diode array is collimated with a lens. The beams pass through a prism beam expander to
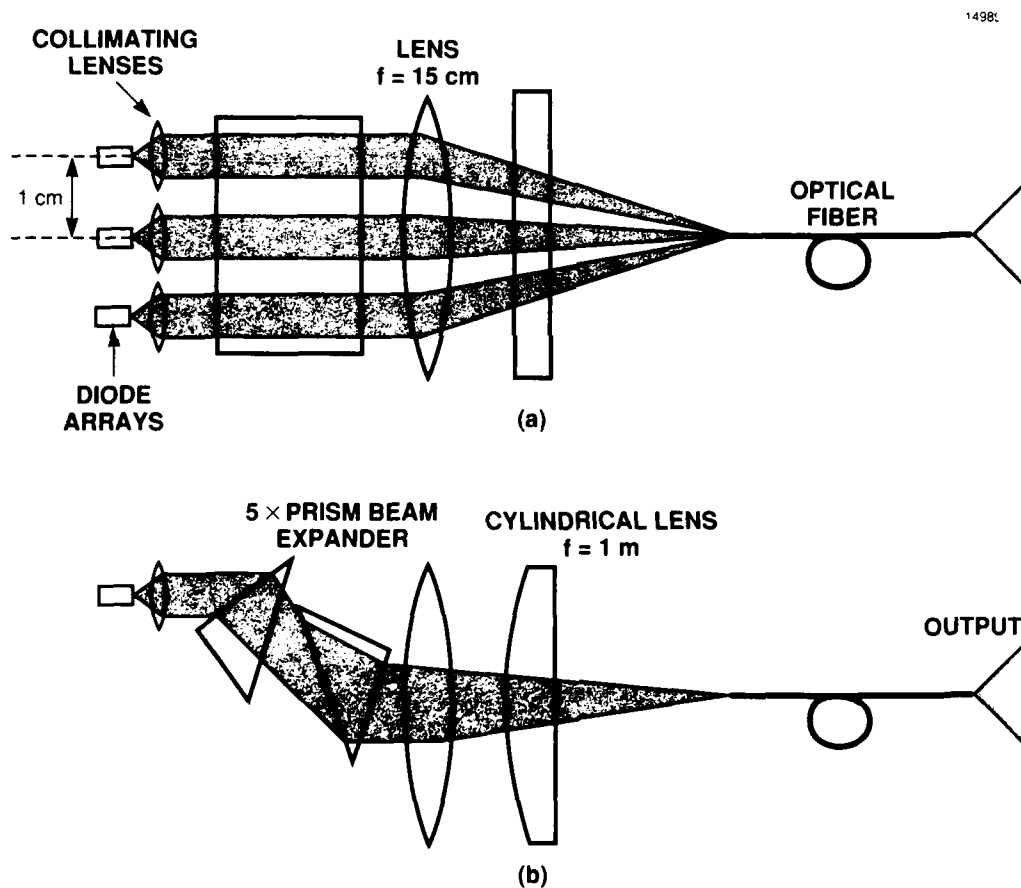
Figure 2-6. Schematic of multiple diode laser arrays coupled to a multimode fiber in planes (a) perpendicular and (b) parallel to the junction.

enlarge the beams ~ 5 times in the plane parallel to the junctions of the arrays. The combined beam is focused into an optical fiber with a 200-μm core and 0.37 numerical aperture using a lens of 15-cm focal length, with a 1-m cylindrical lens to correct for a small amount of astigmatism. In a preliminary experiment, power at the output of the fiber was 465 mW, which is 52 percent of the 892-mW power incident on the input face. The coupling efficiencies for each array operating separately were 47, 54 and 53 percent for the top, middle and bottom arrays, respectively. It should be possible to improve the coupling efficiency with antireflection coatings on the fiber input and output and with the use of better coupling optics.

For efficient coupling to a multimode fiber, the radiation must be focused to a spot smaller than the core and its convergence angle must be inside a cone angle given by the fiber's numerical aperture. The principle of conservation of radiance for the input beam and the fiber characteristics set a limit on the input beam quality for efficient coupling to the fiber [6,7]. A beam can be efficiently coupled to a multimode fiber as long as its beam quality (expressed in number of times diffraction limited) is better than a critical beam quality of the fiber BQ_c, given by

$$BQ_c = \frac{\pi d NA}{2\lambda} \quad .$$
(2.1)

Here, d is the fiber core diameter, NA is its numerical aperture, and λ is the wavelength.

We have calculated the number of sources that can be coupled to a single fiber in the case of geometric multiplexing based on the characteristics of the diode array output beam and the optical fiber used in the above experiment and Equation (2.1). The result indicates that it should be possible to couple over 100 of these arrays efficiently into this multimode fiber, which would lead to tens of watts of power at the fiber output. A basic scaling law derived from the analysis is that the number of identical sources that can be coupled efficiently into a multimode fiber is proportional to the square of the product of the core diameter and numerical aperture.

The increased power that can be obtained by coupling of multiple sources into an optical fiber could lead to new uses of diode laser sources in industrial and medical applications. Another application is in pumping solid state lasers; by coupling multiple sources into a single fiber, the brightness at the output can be higher than with the use of fiber bundles in which each diode source is coupled to an individual fiber. This technique may also be useful for wavelength division multiplexing of large numbers of sources in applications where modal dispersion effects are not important.

<div align="right">T.Y. Fan</div>

2.4 THERMAL AND ABSORPTIVE PROPERTIES OF LiB$_3$O$_5$

A long-pulse-length sodium-resonance source having 0.5-J energy per pulse at 0.589 μm and 10-Hz pulse repetition frequency has been obtained by sum-frequency mixing the 1.064- and 1.319-μm Nd:YAG laser radiation in lithium iodate (LiIO$_3$) [8]. Despite this, the search for an alternative sum-frequency-mixing crystal continues, because of the extremely narrow acceptance angle and large walkoff in LiIO$_3$ as well as its known proclivity to fatigue, which is manifested by sudden catastrophic damage to the crystal after successful operation for a time period varying from several minutes to many hours.

For this reason we have begun to study the frequency conversion properties of lithium triborate (LiB_3O_5, commonly referred to as LBO), a recently discovered nonlinear optical material [9]. It is transparent from 160 nm to 2.6 μm and has an effective nonlinear susceptibility for frequency doubling that is approximately half that of $LiIO_3$. At short pulse lengths ($\tau_p = 0.1$ ns) LBO is believed to have the highest damage threshold of any nonlinear optical crystal measured to date [9]. It remains to be seen whether this high damage threshold carries over to long-pulse-length radiation ($\tau_p = 100$ μs).

An uncoated crystal of LBO measuring 3 × 3.4 × 11.7 mm, grown in mainland China, was obtained for study. It was oriented for noncritical phase matching, with the irradiating beam directed along the X-axis. Initial experiments were carried out to determine the temperature and thermal sensitivity of LBO for noncritical frequency doubling of 1.06 and 1.32 μm, and for frequency summing of 1.06 and 1.32 μm. The results are shown in Figure 2-7. They indicate a significant temperature sensitivity that increases with increasing frequency. However, the thermal bandwidth at these conversion frequencies appears to be sufficiently broad to permit thermal control, even at high-average-power levels, in contrast to the situation in $KNbO_3$ and $LiNbO_3$. The occurrence of a peak temperature for summing 1.06 and 1.32 μm which is slightly above ambient indicates that one can conveniently control the temperature to ensure near-peak operation with noncritical phase matching, thereby ensuring a large acceptance angle and essentially zero walkoff.
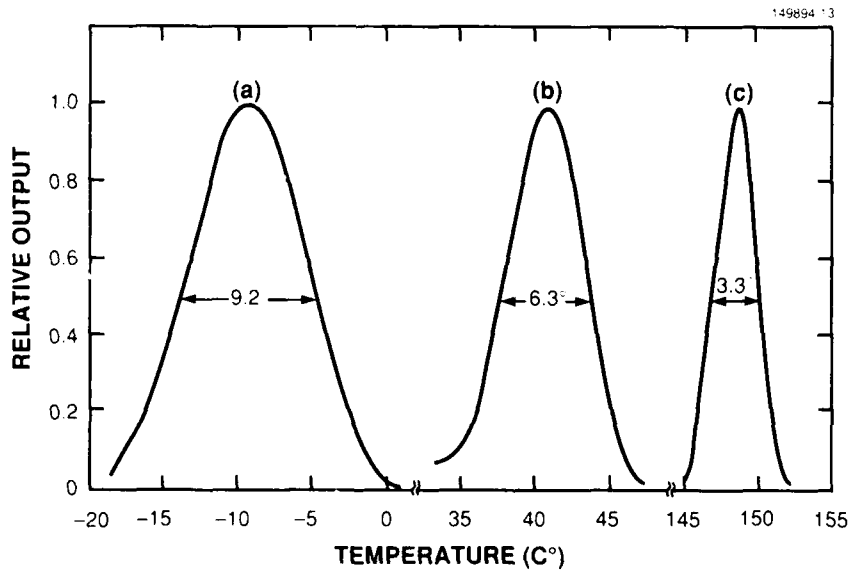
Figure 2-7. Noncritical phase-matching temperature and thermal bandwidths in LiB_3O_5 with radiation directed along the X-axis for (a) frequency doubling 1.32 μm, (b) frequency summing 1.06 and 1.32 μm, and (c) frequency doubling 1.06 μm.

The ability of LBO to retain its high damage threshold under long-pulse-length and high-average-power conditions must ultimately depend on the material having low optical absorption at the frequencies involved. We used the laser calorimetry technique described by Fan and DeFeo [10] to study the absorption of LBO at 1.32, 1.06 and 0.53 μm. The absorption coefficient α is given by

$$\alpha = \frac{\Delta T c_p m}{L P \tau} \quad , \tag{2.2}$$

where ΔT is the temperature shift upon removal of power P (internal to the sample), c_p is the specific heat of LBO, m and L are the mass and length of the sample, respectively, and τ is the time constant of the exponential temperature decrease. The absorption determination was complicated by the existence of a major scattering center within the LBO crystal. Although the crystal appeared to be clear, the presence of the scattering center could be either observed directly when illuminated by visible radiation at 0.53 μm, or looked at with an IR viewer at 1.06 μm. To determine the intrinsic absorption values of LBO given below, it was essential that the laser radiation avoid the scattering center since illumination of the scattering center increases the temperature variation ΔT by over an order of magnitude. All factors in Equation (2.2) are measured in the course of the experiment, except for c_p, which is unknown for LBO. On the basis of c_p values of various lithium- and boron-containing oxides [11] a probable value of $c_p = 1.3$ J/gm K was chosen for use in Equation (2.2).

The resultant values of the absorption coefficient obtained for LBO, with a probable error of ~ 30 percent, were 1.2×10^{-3} cm^{-1} at 1.32 μm, 1.8×10^{-3} cm^{-1} at 1.06 μm, and 1.7×10^{-3} cm^{-1} at 0.53 μm. These values indicate that the intrinsic optical absorption in LBO is comparable to that in LiIO$_3$, and is significantly lower than in KTP or LiNbO$_3$ [12]. These results are encouraging. However, other samples will need to be investigated to establish if the presence of a major scattering center in our sample is indicative of a serious quality control problem involved in the growth of LBO crystals.

N. Menyuk
J. Korn

2.5 MECHANICAL BEAM SCANNING FOR OPTICAL MIXING IN NONLINEAR CRYSTALS

For high-efficiency generation of the optical harmonics, high intensities are required in the interaction volume. In most practical applications this high-intensity radiation stresses the nonlinear crystal, and damage considerations are important. For short-pulse operation, as when radiation from Q-switched lasers is employed, fast optical damage mechanisms determine the limitations. For CW or long-pulse (> 10 μs) operation, localized heating of the mixing crystal due to absorption may impose further limitations on performance. Such heating may result in loss of phase matching or mechanical fracture of the crystal. Localized heating of the crystal may be alleviated by mechanically scanning the interacting radiation through the nonlinear crystal, so as to distribute the heat in a volume that is several times larger than the instantaneous mixing volume. Ways in which the interaction region for harmonic mixing can be mechanically scanned through a nonlinear crystal with sufficient speed to alleviate localized heating have

been examined, and a practical experiment that demonstrates the principles involved has been carried out. Because it is the simplest case, only second-harmonic generation will be described; however, the underlying concepts can equally be applied to sum- and difference-frequency generation.

As a typical second-harmonic generation geometry, consider the type I interaction in $LiIO_3$ for 1.06-μm radiation, sketched in Figure 2-8; for simplicity, it is assumed that proper phase matching is achieved at normal incidence of the fundamental beam. As is well known [13], for second-harmonic generation to occur coherently along the crystal thickness T, the input laser beam has to be contained within the acceptance angle, which can be quite narrow in the plane of the figure; for example, for a 1-cm-thick $LiIO_3$ crystal, the tolerance is about 0.34 mrad. The angle in the plane normal to the figure is much less critical. Depending on the crystal employed, a particular orientation of the crystallographic X- and Y-directions may also be required. If the laser beam is moved to distribute the heat, the above geometric conditions must be satisfied during the scan.
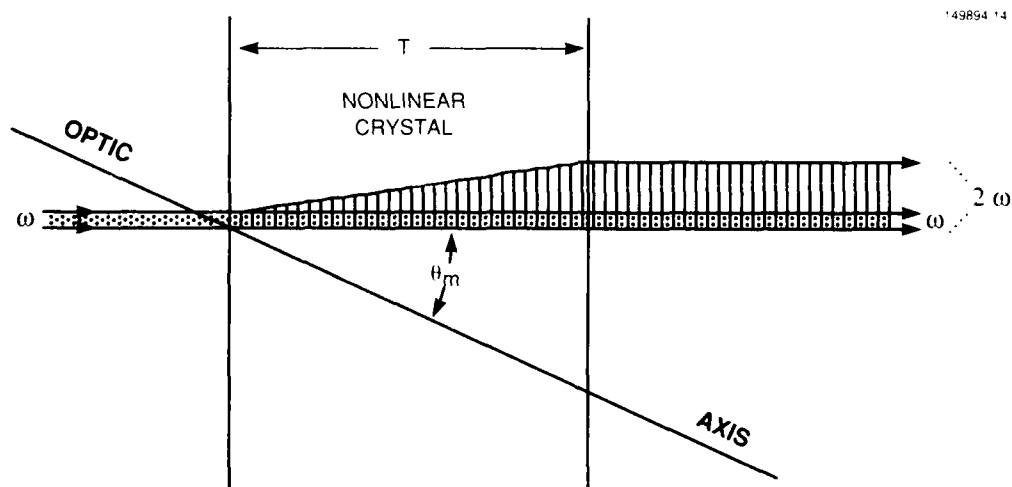
Figure 2-8. Illustration of second-harmonic generation.

A very simple way of implementing a pure translation of a beam of radiation involves the use of a rotating flat mirror and a lens [14]. A stationary beam is reflected by a mirror onto a converging lens. As the mirror rotates around a point in the focal plane of the lens, the beam refracted by the lens moves parallel to itself. This is illustrated in Figure 2-9 for three orientations of the spinning mirror (M_1). Strictly, the motion is an exact translation only if M_1 rotates around the center of the incoming beam; in practice, it is quite easy to keep the direction constant within a small fraction of a milliradian. Collimation of the scanned beam, so as to achieve a focus in the nonlinear crystal, can be adjusted by suitable optics (spherical or cylindrical) placed before the mirror. For reasonable angles of incidence, the state of polarization of the scanned beam is maintained during the scan. It should be noted that a parabolic mirror or any suitable combination of reflective-refractive optics can be used in place of the lens of Figure 2-9.

21
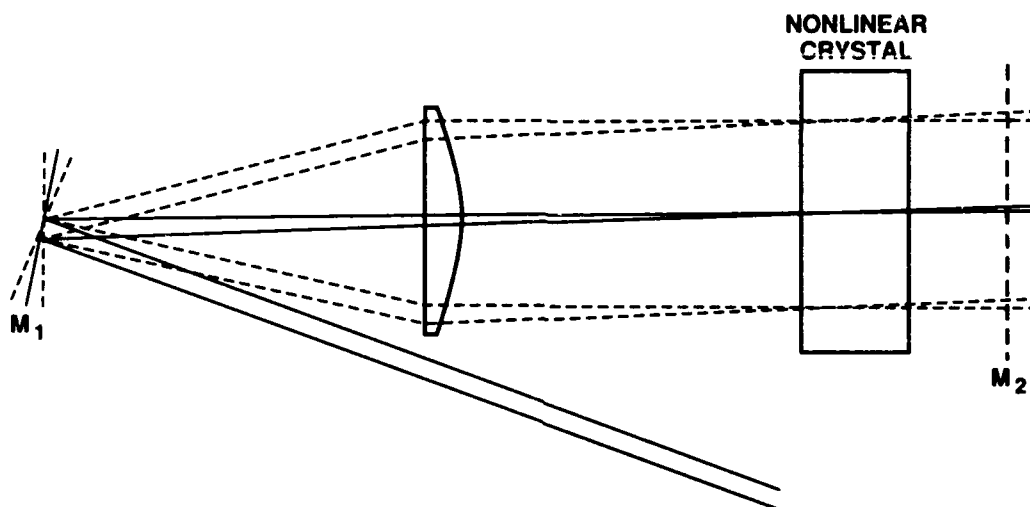
Figure 2-9.   Schematic of the configuration for rapid translation of laser radiation through a nonlinear crystal while maintaining phase matching. The laser radiation is reflected from a spinning mirror (M_1) and then propagates along a conical path to a lens that collimates the radiation along the M_1-lens axis. Subsequently, the laser radiation enters a nonlinear crystal that produces second-harmonic radiation. The latter radiation may then be retroreflected from a flat mirror (M_2), which is placed after the mixing crystal, and separated from the input laser radiation after reflection from M_1.

To apply the concept to second-harmonic generation, the doubling crystal is placed at the focus of the moving beam (a distance f behind the lens in the case of Figure 2-9, which shows a collimated incoming beam). The harmonic output can then be sent to suitable optics to obtain a stationary output beam. In some cases, it should be easy to achieve this result in a compact design, by just retroreflecting the second-harmonic-generated beam from a flat mirror (M_2) placed a short distance past the mixing crystal. Separation of the second harmonic from the fundamental can easily be achieved by using dichroic or polarizing beamsplitters, or by spatially offsetting the second-harmonic-generated beam returning to M_1 through a small tilt in M_2. In this arrangement, only one rotating component, M_1, is required to generate and undo the beam scan.

The choice of mechanism used to impart motion to the spinning mirror depends on the required scanning speed and whether operation is continuous or pulsed. For continuous operation, it is very easy to obtain a near-circular scan by mounting M_1 (Figure 2-9) on the shaft of a motor, with a small angle δ between the normal axis of mirror rotation and the motor axis [14]. (An exactly circular scan is generated if the stationary input beam is directed along the lens axis; however, because of the geometry [Figure 2-9] there is a small ellipticity, which is of no consequence.) If Ω_M denotes the motor angular speed, the scan speed is $\Omega_M f \tan 2\delta$, along a circle of diameter $2f \tan 2\delta$. As an example, a 5-cm-diam. circle can be scanned at 63 m/s with a mirror rotating at 24,000 rpm. At this speed the radiation will travel 6.3 mm in

22

100 μs. For pulsed operation, a discontinuous scan (synchronized to the input beam pulses) can offer both faster sweep and better utilization of the volume of the nonlinear material. By referring again to Figure 2-9, it can be seen that if the axis of rotation of the mirror is contained in its plane, twice the full angular speed of the motor is imparted to the deflected beam. The linear scan speed, therefore, increases by the factor 2/tan 2δ over the expression given above. For long-pulse operation, it then becomes quite feasible to stretch a single pulse over several centimeters of crystal. An extension to a rectangular raster scan can easily be devised, and this could be of considerable interest for high-power applications.

The circular scanning technique has been demonstrated to maintain second-harmonic-generation phase matching over the full scan of the laser beam. A 1.06-μm laser beam was reflected from a mirror that was spinning at 68 Hz. The axis of the cone scanned by the laser beam was aligned with the optical axis of a lens of 1-m focal length, which was placed ~ 1 m from the spinning mirror. The 1.06-μm beam described a 2-cm-diam. circle at the lens position. By careful positioning of this lens it was possible to obtain a very nearly cylindrical scan of the laser beam around the optical axis of the lens. The laser beam then described a 2-cm-diam. circle at the 3-cm-long $LiIO_3$ crystal. A focusable beam-expanding telescope was inserted along the path of the incoming 1.06-μm laser beam. Careful adjustment of this telescope made the divergence of the scanned laser beam less than the minimum acceptance angle of the nonlinear crystal.

The acceptance angle of a 3-cm-long $LiIO_3$ crystal for 1.06-μm second-harmonic generation is 0.11 mrad in the plane perpendicular to the laser beam polarization vector and 16 mrad in the plane containing the polarization vector. This asymmetry in the angular acceptance of the $LiIO_3$ crystal provides a convenient means for measuring the sensitivity of the collimation of the laser beam to the position of the lens. For example, if the lens is too close to (or far from) the spinning mirror, then the laser beam will rotate about the surface of a diverging (or converging) cone and will alternately go in and out of the phase-matching acceptance angle of the $LiIO_3$ crystal. When the beam is moving parallel to the polarization vector, then a slight deviation (> 0.02 mrad) of the laser beam from the phase-matching condition will result in reduced second-harmonic generation. When the beam is moving perpendicular to the polarization vector, then a deviation up to 2.8 mrad will result in negligible change in the second-harmonic generation. Since the laser beam passes through the angle-sensitive plane two times per revolution, the variation in second-harmonic power occurs at two times the frequency of rotation of the mirror. The variation in second-harmonic power as a function of lens position is shown in Figure 2-10. As can be seen, proper placement of the lens resulted in less than 2-percent variation of the second-harmonic generation, indicating that the laser beam rotated about a cone with less than about 0.02-mrad divergence. In addition, a ± 0.5-cm change in the lens position resulted in less than a 10-percent variation in second-harmonic generation.

V. Daneu
T.H. Jeys
J. Korn
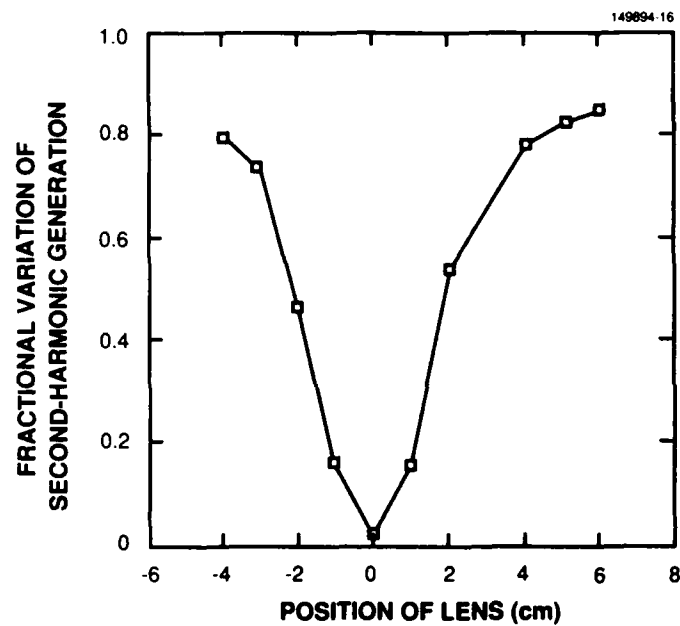
Figure 2-10. Variation in second-harmonic power as a result of spinning of the fundamental radiation through a circular path in the LiIO$_3$ crystal, as a function of the position of the collimating lens.

REFERENCES

1. P.A. Schulz, *IEEE J. Quantum Electron.* **24**, 1039 (1988).

2. P.A. Schulz, *Appl. Opt.* **28**, 4458 (1989).

3. Solid State Research Report, Lincoln Laboratory, MIT (1989:3) p. 10.

4. J. Goodberlet, J. Wang, J.G. Fujimoto, and P.A. Schulz, *Opt. Lett.* **14**, 1125 (1989).

5. T.Y. Fan, A. Sanchez, and W.E. DeFeo, *Opt. Lett.* **14**, 1057 (1989).

6. M.C. Hudson, *Appl. Opt.* **13**, 1029 (1974).

7. D.H. McMahon, *J. Opt. Soc. Am.* **65**, 1479 (1975).

8. Solid State Research Report, Lincoln Laboratory, MIT (1989:4), p. 18.

9. C. Chen, Y. Wu, A. Jiang, B. Wu, G. You, R. Li, and S. Lin, *J. Opt. Soc. Am.* B **6**, 616 (1989).

10. Solid State Research Report, Lincoln Laboratory, MIT (1989:1), p. 29.

11. Y.S. Touloukian and E.M. Buyko, *Specific Heat–Nonmetallic Solids*, Vol. 5 of *Thermophysical Properties of Matter: The TPRC Data Series*, edited by Y.S. Touloukian and C.Y. Ho (IFI/Plenum, New York, 1970).

12. D.J. Gettemy, W.C. Harker, G. Lindholm, and N.P. Barnes, *IEEE J. Quantum Electron.* **24**, 2231 (1988).

13. J.E. Midwinter and F. Zernike, *Applied Nonlinear Optics* (Wiley, New York, 1973).

14. C.Calì, V. Daneu, and S. Riva-Sanseverino, *Opt. Acta* **27**, 1267 (1980).

3. MATERIALS RESEARCH

3.1 InGaAs/AlGaAs STRAINED SINGLE-QUANTUM-WELL DIODE LASERS

Strained quantum-well InGaAs/AlGaAs lasers, in which the InGaAs active layer is thin enough for the strain to be elastically accommodated, are currently of considerable interest [1-7] because the emission wavelength can be extended to ~ 1.1 μm, compared with a long-wavelength limit of ~ 0.9 μm for GaAs/AlGaAs lasers. Potential applications include pumping Er^{3+}-doped fiber amplifiers [8] at 0.98 μm and obtaining blue-green laser emission by frequency doubling. Since the compressive strain in the InGaAs layer splits the degenerate valence band, thereby reducing the effective density of states, lower threshold current densities J_{th} have been predicted for the strained lasers compared with unstrained lasers [9,10]. However, the observed reduction has not been as great as expected. The lowest J_{th} value previously reported [4] for InGaAs/AlGaAs lasers is 114 A/cm^2 for a cavity length L of 1540 μm, compared with 85 A/cm^2 reported [11] for GaAs/AlGaAs lasers for L = 3000 μm. In addition, InGaAs lasers with emission wavelengths around 1 μm have had lower differential quantum efficiencies η_d and characteristic temperatures T_0 than GaAs devices. Here, we report InGaAs/AlGaAs graded-index separate-confinement heterostructure single-quantum-well (GRIN-SCH SQW) lasers emitting at 1.02 μm that have J_{th} values as low as 65 A/cm^2 for L = 1500 μm. Values of η_d as high as 90 percent have been measured for L = 300 μm. Between 25 and 45°C, T_0 = 178 K for L = 1500 μm, comparable to values obtained for GaAs lasers.

The laser structure was grown by organometallic vapor phase epitaxy in a low-pressure vertical rotating-disc reactor [12] using $Ga(CH_3)_3$, $Al(CH_3)_3$, $In(CH_3)_3$, AsH_3, H_2Se and $Zn(CH_3)_2$. The device structure, shown in Figure 3-1, consists of the following layers: 1-μm-thick n-$Al_{0.7}Ga_{0.3}As$ cladding
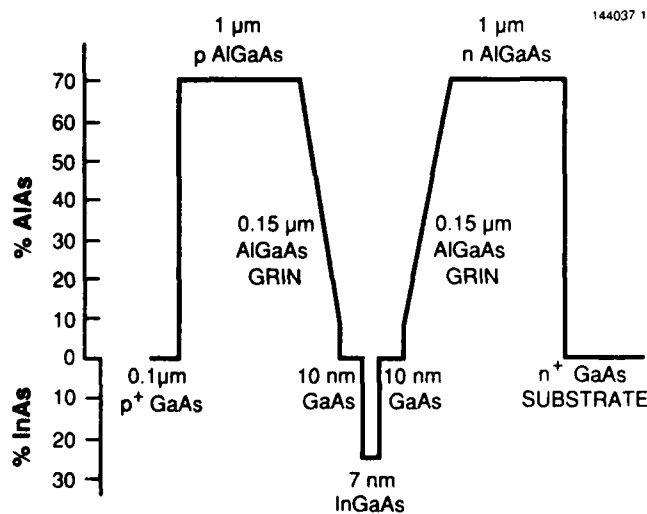
Figure 3-1. Structure of InGaAs/AlGaAs GRIN-SCH SQW diode laser.

layer, 0.15-μm-thick n-AlGaAs confining layer (AlAs mole fraction linearly graded from 0.7 to 0.08), 10-nm-thick GaAs bounding layer, 7-nm-thick $In_{0.25}Ga_{0.75}As$ active layer, 10-nm-thick GaAs bounding layer, 0.15-μm-thick p-AlGaAs confining layer (AlAs mole fraction graded from 0.08 to 0.7), 1-μm-thick p-$Al_{0.7}Ga_{0.3}As$ cladding layer, and 0.1-μm-thick p^+-GaAs contacting layer. The AlGaAs layers were grown at 800°C, and the InGaAs layer was grown at 640°C. The surface morphology was extremely smooth with no texture seen under a Nomarski interference microscope. As discussed below, the thin GaAs layers bounding the InGaAs layer are very important for obtaining smooth interfaces, reducing J_{th}, and increasing η_d. The composition of the active layer was found by using room-temperature photoluminescence measurements to determine the bandgap of a thick InGaAs layer grown under the same conditions on a separate GaAs substrate and applying the expression given by Kolbas et al. [13] for the relationship between the bandgap and InAs mole fraction of InGaAs alloys.

The characteristics of broad-stripe lasers either 100 or 300 μm wide were measured using 200-ns pulses at 10 kHz. The emission wavelength was ~ 1.02 μm, very close to the value calculated by Kolbas et al. [13] for a 7-nm-thick $In_{0.25}Ga_{0.75}As$ active layer. Light output measurements were made using a calibrated Si detector. Figure 3-2 shows J_{th} as a function of L for 100-μm-wide lasers. The value of J_{th} decreases monotonically from ~ 175 A/cm^2 for L = 300 μm to ~ 65 A/cm^2 for L = 1500 μm, then remains constant. These low values are believed to be the result of the compressive strain in the active layer as well as tight optical confinement and good interfaces. Plotting J_{th} vs 1/L yields a straight line with slope corresponding to a gain coefficient of 0.085 cm μm A^{-1}, compared with 0.069 cm μm A^{-1} reported by Welch et al. [7] for InGaAs/AlGaAs lasers with InAs mole fractions of 0.1 and 0.2.
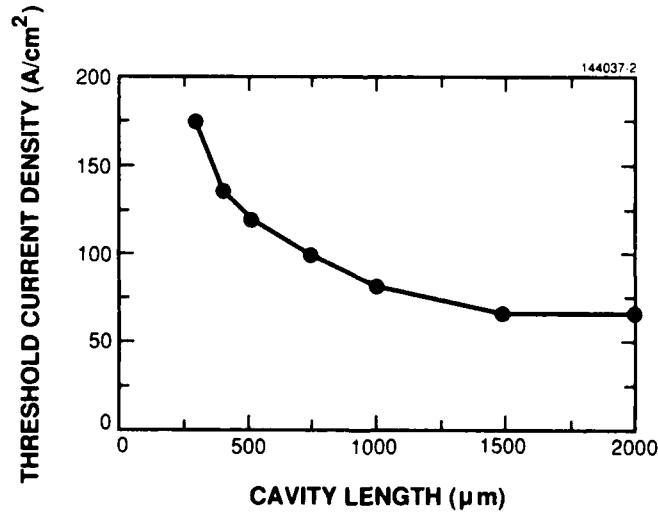
Figure 3-2. Threshold current density J_{th} of InGaAs/AlGaAs diode lasers as a function of cavity length L.

For the 100-μm-wide lasers, η_d decreases from 90 to 50 percent as L is increased from 300 to 2000 μm. Figure 3-3 shows the dependence of η_d^{-1} on L. The straight line drawn through the points yields a value of ~ 100 percent for the internal quantum efficiency η_i. The value of the internal loss coefficient α calculated from the slope of this line is ~ 5 cm^{-1}, compared with values of 2 to 3 cm^{-1} that we obtain for our best GaAs/AlGaAs GRIN-SCH SQW lasers [12], the structure of which is designed to reduce losses due to free-carrier absorption in the AlGaAs cladding layers. The temperature dependence of threshold current measured for InGaAs/AlGaAs lasers between 25 and 45°C yields T_0 values of 178, 159 and 137 K for $L = 1500$, 1000 and 300 μm, respectively. The values of T_0 obtained from data between 45 and 65°C are 30 to 40 K lower.
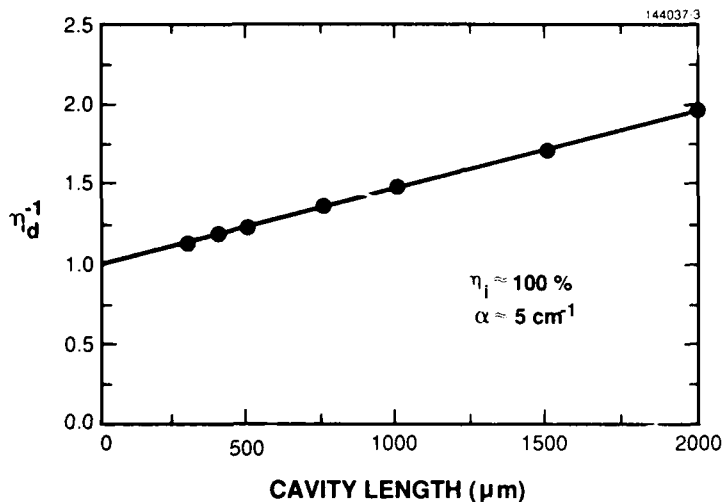
Figure 3-3. Reciprocal differential quantum efficiency η_d^{-1} of InGaAs/AlGaAs diode lasers as a function of cavity length L.

For CW operation, several devices were mounted junction side down on a copper heat sink with indium solder. The light output was measured with a thermopile detector. Figure 3-4 shows the light output vs current for an uncoated 300-μm-wide laser with $L = 1000$ μm. The maximum output power is 1.6 W per facet, limited by temperature rise. The value of η_d is about 31 percent per facet, and the power conversion efficiency is as high as 47 percent. It should be possible to achieve significantly higher power efficiencies by decreasing L and modifying the structure to reduce internal loss.

To investigate the effect of the GaAs bounding layers on laser performance, we fabricated InGaAs/AlGaAs lasers with $L = 500$ μm from three GRIN-SCH SQW structures that differed only in the bounding layer thickness t. Two of these structures had $t = 5$ and 10 nm, respectively, while the third had no bounding layers. In other respects the three structures were like the one shown in Figure 3-1, except that the Al$_x$Ga$_{1-x}$As confining layers had x graded from 0.2 to 0.7, rather than from 0.08 to 0.7. The surface morphology was excellent for the structure with $t = 10$ nm, but was not as smooth for $t = 5$ nm and still worse for the structure without bounding layers. The operating characteristics of the lasers with

29
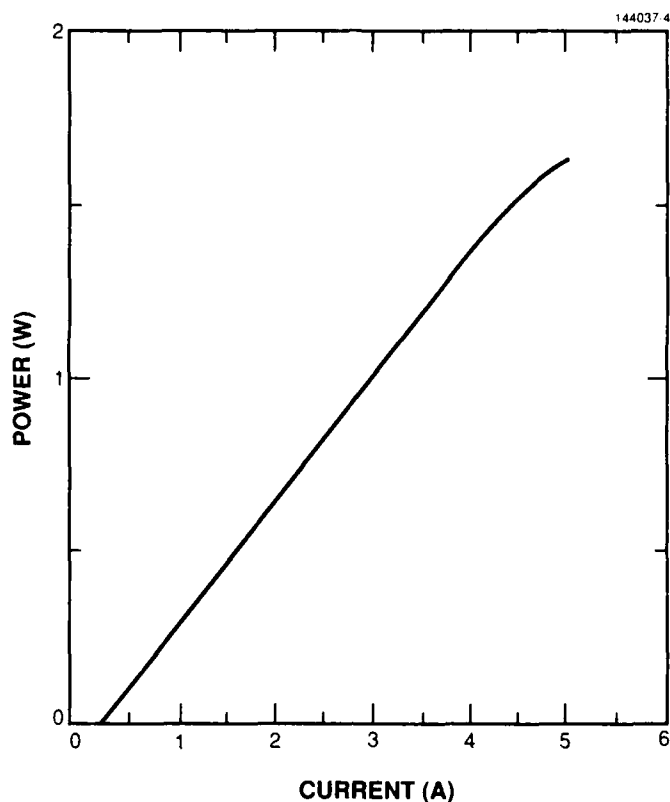
Figure 3-4. Light output vs current for an InGaAs/AlGaAs laser 300 μm wide with L = 1000 μm.

t = 5 and 10 nm did not differ greatly from each other, with J_{th} = 150 and 125 A/cm^2, respectively, and with η_d = 74 and 80 percent, respectively. For the lasers without GaAs bounding layers, however, J_{th} rose sharply to 550 A/cm^2 and η_d fell to only 46 percent. In addition, the emission wavelength shifted from ~ 1.02 μm for the lasers with GaAs bounding layers to ~ 0.97 μm for those without the layers, as a result of the increase in J_{th} and the associated increase in band filling. It is clear that the bounding layers have played an important role in achieving the excellent performance of our strained-layer InGaAs/AlGaAs lasers. In an earlier study [2] of such lasers, incorporation of GaAs bounding layers reduced the value of J_{th} by about 50 percent.

H.K. Choi
C.A. Wang

3.2 CONDITIONS FOR ATOMIC LAYER EPITAXY OF GaAs USING OMVPE

In conventional growth of binary compound semiconductors by such techniques as molecular beam epitaxy and organometallic vapor phase epitaxy (OMVPE), the substrate is exposed simultaneously to the sources of the two constituent elements. In atomic layer epitaxy (ALE), the substrate is exposed alternately to the two sources in such a manner that epitaxial growth takes place by the deposition of alternating monolayers of the elements [14]. Since this technique permits precise control of epilayer thickness and composition, it is being widely investigated for the growth of complex structures like quantum wells and superlattices. In addition, the method is of interest for heteroepitaxial growth in lattice-mismatched systems, where an initial two-dimensional growth step at low temperature is frequently used in order to avoid island formation.

In the case of the II-VI compounds, ALE is inherently a self-limiting process, since both the group II and group VI elements are so volatile at epitaxial growth temperatures that only one group II atom can be deposited per surface group VI atom, and vice versa. In the case of ZnSe, for example, one monolayer is the maximum quantity of Zn that can be deposited on a ZnSe substrate by unlimited exposure to a Zn source in the absence of a Se flux, and similarly one monolayer of Se is the maximum that can be deposited by unlimited exposure to a pure Se flux. Consequently, ALE of the II-VI compounds can be accomplished over a broad range of substrate temperatures and without close control of the quantity of either element per exposure, provided that the quantity in each case is sufficient for the deposition of a complete monolayer.

For the III-V compounds, in contrast, ALE is not fully self-limiting. Although deposition of the volatile group V elements As and P is generally limited to one monolayer if there is no flux of the group III element, the volatility of the group III elements Al, Ga and In is so low that in general the deposition of these elements can exceed one monolayer even if there is no group V flux. Therefore, the method requires establishment of specific growth conditions under which group III deposition is limited to one monolayer per exposure. In this study, we have determined such conditions for ALE growth of GaAs by OMVPE at temperatures ranging from 425 to 500°C.

The experiments were performed in a vertical rotating-disk reactor that yields GaAs epilayers of highly uniform thickness when used for conventional OMVPE growth [12]. The process gases are introduced through a stainless steel mesh to ensure uniform flow into the reactor tube. A pressure- and flow-balanced vent-run system is used to permit rapid switching from one gas to another without pressure surges. For this study, the susceptor rotation rate was 20 rpm. Trimethylgallium (TMG) and 100-percent arsine (AsH_3) were used as the sources of Ga and As, respectively, and H_2 was used as the carrier gas. The operating pressure was 0.2 atm and the H_2 flow rate was 10 slm. Under these conditions the average gas residence time in the reactor is less than 1 s.

The substrates used for epilayer growth were undoped semi-insulating (100) GaAs wafers tilted 2° toward (110). To begin a growth run, an etch-stop layer of $Al_{0.5}Ga_{0.5}As$ was first grown by the conventional simultaneous-exposure procedure at a substrate temperature of 800°C, using trimethylaluminum (TMA) as the Al source. The TMG and TMA were switched out while maintaining the AsH_3 flow, and the temperature was reduced to the value selected for GaAs growth. The GaAs epilayer was then grown by a series of deposition cycles, in each of which the substrate was exposed alternately to TMG and AsH_3. After exposure to each source gas, the reactor was purged with pure H_2 for a period of 3 s, which

was long enough in relation to the gas residence time for the reactor tube to be cleared of that source before the other was introduced. For the AsH_3 exposures, AsH_3 was injected into the H_2 stream for 5 s at a flow rate of 25 sccm. In preliminary experiments, it was found that this procedure produced sufficient As deposition so that the GaAs growth rate R was not limited by the AsH_3 exposure. After completion of GaAs growth, a portion of the wafer was masked with wax, the bare GaAs was removed by etching with H_2O_2 down to the AlGaAs layer, and the step height was measured by Dektak profiling. To obtain R in monolayers per growth cycle, the step height was divided by 0.283 nm, the thickness of a GaAs monolayer, and then by the number of growth cycles.

In each series of growth experiments, the substrate temperature was kept constant, and R was measured as a function of the TMG exposure parameters. In one type of experiment, the TMG injection time per exposure was fixed and the flow rate of TMG into the carrier gas stream (which determines the TMG concentration in the reactor) was varied. In a second type, the flow rate was fixed and the injection time was varied. For experiments of the first type with a fixed injection time of 3 s, Figure 3-5 shows R as a function of TMG flow rate at temperatures from 425 to 500°C. At each flow rate, R increases monotonically with increasing temperature. At the three lowest temperatures, R has become approximately constant when the flow rate reaches 3 sccm, with a value well below 1 monolayer/cycle. At 450, 460 and 475°C, although the data are less extensive, it is clear that the initial rate of increase in R with increasing flow rate is not maintained up to 3 sccm. At the higher two temperatures, R exceeds 1 monolayer/cycle at 3 sccm.
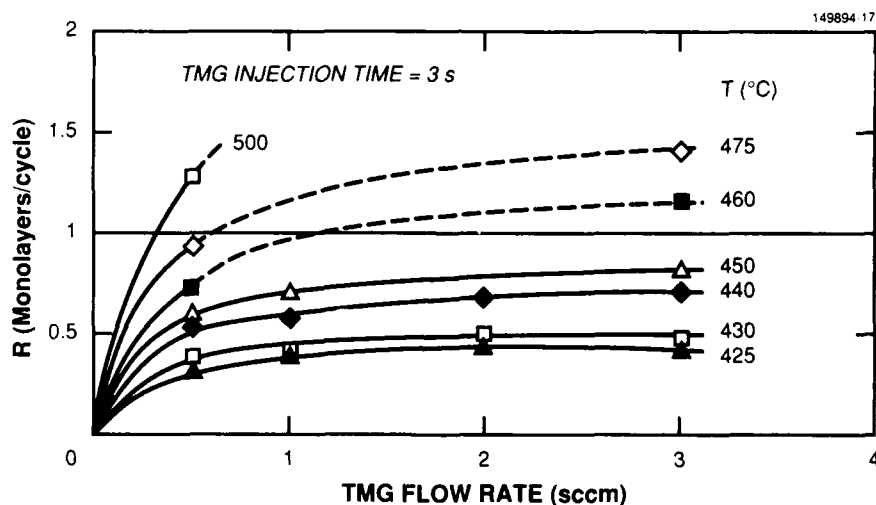
Figure 3-5. Growth rate R vs TMG flow rate for alternating-exposure growth of GaAs with a TMG injection time of 3 s.

The data in Figure 3-5 for the lower temperatures show that the concentration of TMG obtained at a flow rate of 3 sccm is high enough so that it is not the factor limiting the value of R, while the data for the higher temperatures show that this concentration is sufficient to yield R values of 1 monolayer/cycle or above if the Ga deposition rate determined by the temperature is high enough. In a second set of
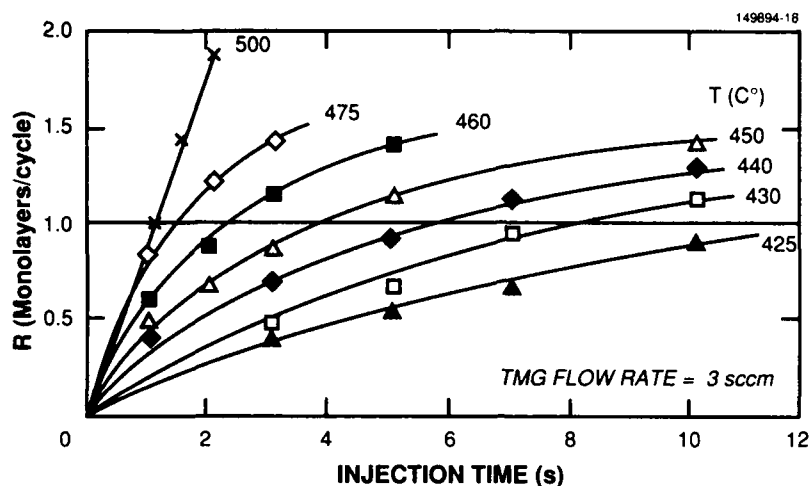
Figure 3-6. Growth rate R vs TMG injection time for alternating-exposure growth of GaAs with a TMG flow rate of 3 sccm.
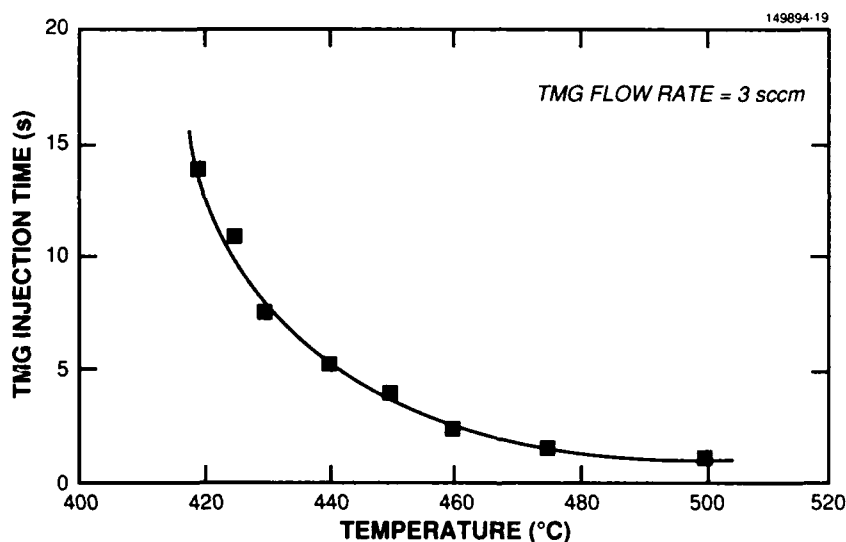
Figure 3-7. TMG injection time required for R = 1 monolayer/cycle vs temperature for alternating-exposure growth of GaAs with a TMG flow rate of 3 sccm.

experiments, which was designed to establish conditions for ALE over the whole temperature range, the flow rate was therefore fixed at 3 sccm, and R was measured as a function of the TMG injection time. The results are shown in Figure 3-6. At each temperature, with increasing injection time R increases to more than 1 monolayer/cycle without saturating, and for a given injection time R increases monotonically with increasing temperature. The injection time that yields R = 1 monolayer/cycle, as obtained by interpolation from the curves drawn in Figure 3-6, is plotted against temperature in Figure 3-7. The time

33

decreases from 14 s at 420°C to 1 s at 500°C. The injection time required for ALE at any temperature within this range can be read off the curve through the data points.

C.A. Wang
D.M. Tracy

REFERENCES

1. D. Feketa, K.T. Chan, J.M. Ballantyne, and L.F. Eastman, *Appl. Phys. Lett.* **49**, 1659 (1986).

2. W. Stutius, P. Gavrilovic, J.E. Williams, K. Meehan, and J.H. Zarrabi, *Electron. Lett.* **24**, 1494 (1988).

3. L.E. Eng, T.R. Chen, S. Sanders, Y.H. Zhuang, b ⁷hao, and Y. Yariv, *Appl. Phys. Lett.* **55**, 1378 (1989).

4. D.P. Bour, R.U. Martinelli, D.B. Gilbert, L. Elbaum, and M.G. Harvey, *Appl. Phys. Lett.* **55**, 1501 (1989).

5. K.J. Beernink, P.K. York, J.J. Coleman, R.G. Waters, J. Kim, and C.M. Wayman, *Appl. Phys. Lett.* **55**, 2167 (1989).

6. A. Larsson, J. Cody, and R.J. Lang, *Appl. Phys. Lett.* **55**, 2268 (1989).

7. D.F. Welch, W. Streifer, C.F. Schaus, S. Sun, and P.L. Gouley, *Appl. Phys. Lett.* **56**, 10 (1990).

8. K. Suzuki, Y. Kimura, and M. Nakazawa, *Appl. Phys. Lett.* **55**, 2573 (1989).

9. A.R. Adams, *Electron. Lett.* **22**, 249 (1986).

10. E. Yablonovitch and E.O. Kane, *J. Lightwave Technol.* **LT-4**, 504 (1986).

11. H.Z. Chen, A. Ghaffari, H. Morkoç, and A. Yariv, *Appl. Phys. Lett.* **51**, 2094 (1987).

12. C.A. Wang, H.K. Choi, and M.K. Connors, *J. Electron. Mater.* **18**, 695 (1989).

13. R.M. Kolbas, N.G. Anderson, W.D. Laidig, Y. Sin, Y.C. Lo, K.Y. Hsieh, and Y.J. Yang, *IEEE J. Quantum Electron.* **24**, 1605 (1988).

14. T. Suntola, *Mater. Sci. Rpt.* **4**, 261 (1990).

4. SUBMICROMETER TECHNOLOGY

4.1 PLASMA-DEPOSITED AMORPHOUS CARBON FILMS
AS PLANARIZATION LAYERS

Planarization techniques to reduce topography are essential for advanced device fabrication, both to improve step coverage for multiple-level metallization and to reduce the depth-of-field limitations in high-resolution lithography. We have developed a dry planarization process utilizing plasma-deposited amorphous carbon (a-C:H) films. This method exhibits excellent planarizing effects over long distances. Carbon films 2.5 μm thick have been shown to reduce the height of 1.5-μm steps to less than 0.2 μm for 400-μm-wide features.

The deposition was carried out in a conventional 13.56-MHz RF-powered parallel-plate plasma-enhanced chemical vapor deposition (PECVD) system. The characteristics of the films depend on the deposition conditions, including source gas composition, RF power, degree of ion bombardment, temperature, pressure, and electrode spacing. Films providing long-range planarization are ones that flow over surface topography during deposition. Figure 4-1 shows a scanning electron micrograph (SEM) of a typical planarizing film, which was deposited at 25°C using toluene as the source gas with a self-induced dc bias voltage of –10 V.

149894-20

|← 10 µm →|
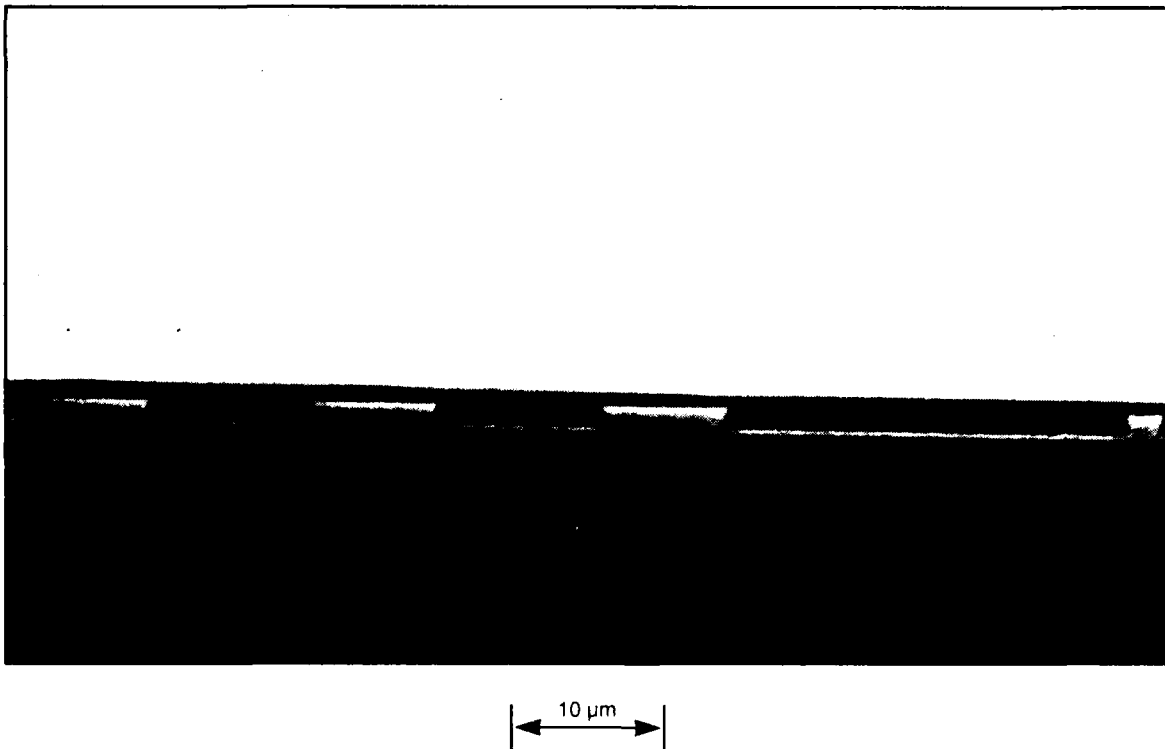
Figure 4-1. SEM of 1.5-µm-high SiO₂ steps planarized with a 2.5-µm-thick PECVD a-C:H film.

A wide variety of precursor gases have been evaluated, but only those with a high carbon-to-hydrogen ratio exhibit good planarization characteristics. The films were deposited at power densities ranging from 60 to 550 mW/cm^2 and at pressures varying from 500 to 950 mTorr. The combination of low power and high pressure minimizes both the degree of dissociation in the gas phase and the amount of cross-linking in the films, resulting in low-viscosity a-C:H films and a high degree of planarization. The substrate temperature also has a pronounced effect on the film characteristics. Figure 4-2 shows two films deposited under identical conditions except for a difference in substrate temperature. The a-C:H layer deposited at 25°C is nearly perfectly planar, while the one deposited at 80°C is conformal.
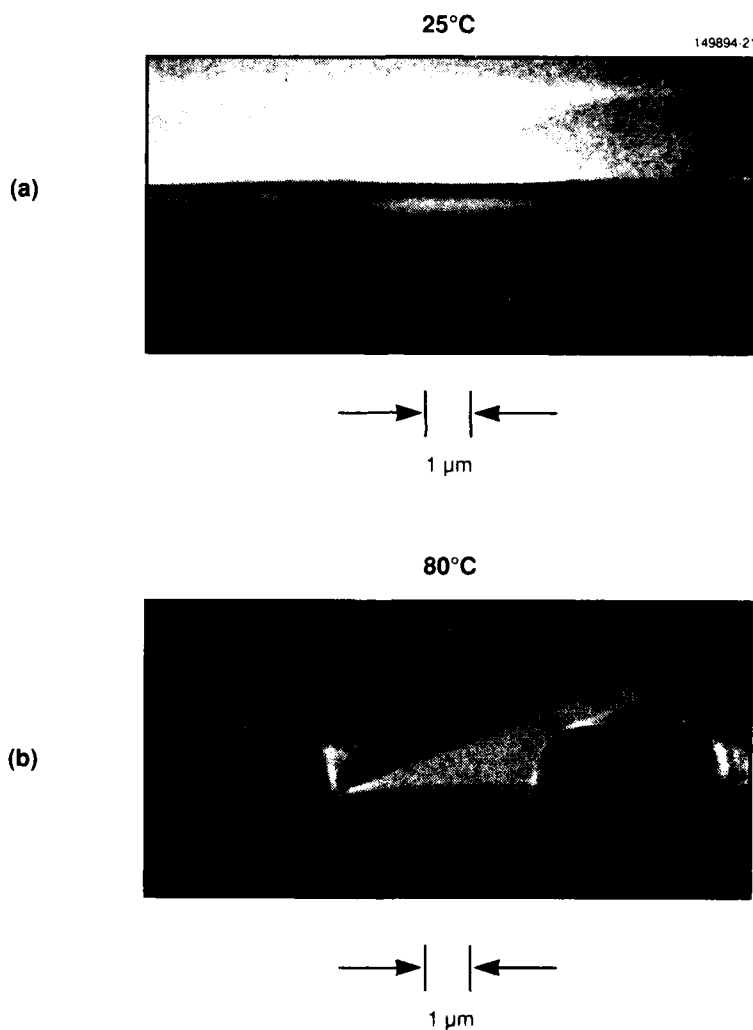
Figure 4-2. Effect of substrate temperature on the planarizing properties of the PECVD a-C:H shown by films deposited over 1.5-μm-high steps at (a) 25°C (planarizing) and (b) 80°C (conformal).

36

A hardening process may be required after deposition, depending on the subsequent processing steps. This entails heating the films at temperatures between 100 and 350°C and/or exposing them to a high-pressure (500 to 950 mTorr), low-power (< 5 W) inert-gas plasma for a period of 0.25 to 2 h. The most effective hardening scheme incorporates both a very low power N_2 gas discharge and elevated temperatures, and results in a planarizing layer 30 times harder than an as-deposited film. The relative hardness is determined by the force necessary to cause a visible indentation with a submicrometer stylus. This process also removes volatile compounds and induces cross-linking, making the hardened film less soluble in common organic solvents. A loss of thickness accompanies the hardening, but the degree of planarization remains the same, which is attributed to thermal reflow of the films during the process.

Our method provides several advantages over commonly used dry planarization techniques. The deposition of the planar films can be carried out at room temperature, which is substantially lower than that used in thermal reflow techniques [1,2]. Compared with the bias-sputter deposition technique [3-5], this process minimizes potential radiation damage through low ion-bombardment energy (10 V), and has the fast deposition rate (300 nm/min) necessary for high throughput. Our technique also has several advantages over conventional spin-on methods [6]. Plasma-deposited films show no radial dependence of planarization related to the centrifugal force during spinning. In addition, plasma-deposited layers have both a higher degree and longer distance of planarization than conventional spin-on layers. Figure 4-3
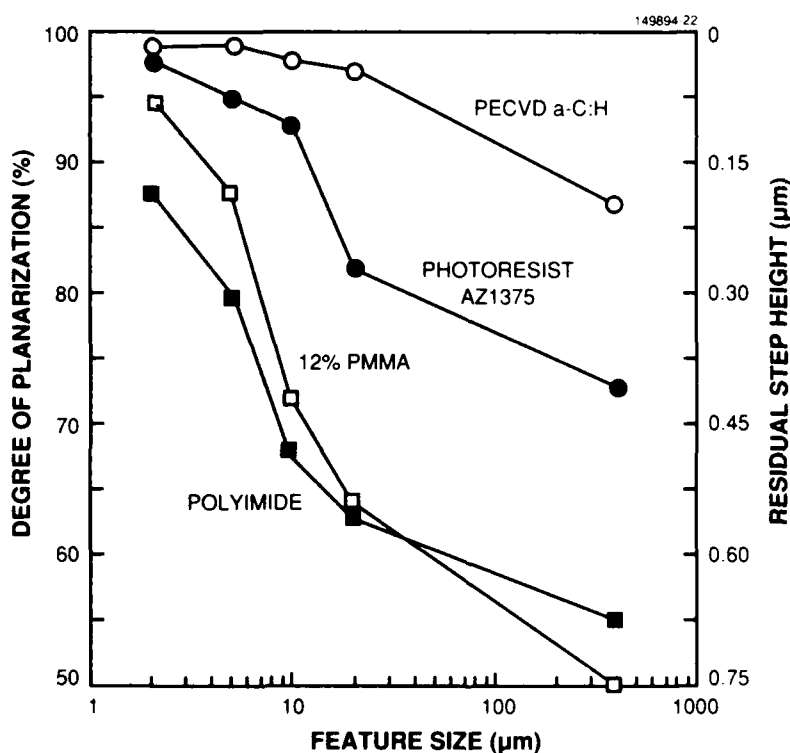
Figure 4-3. Comparison of the planarizing properties of PECVD a-C:H films with those of three spun-on organic materials. The initial step height was 1.5 μm, and the planarizing film thickness was 3 μm. The degree of planarization drops with increasing feature size for all tested materials, but the PECVD film has the highest degree of planarization (> 85 percent), even for 400-μm-wide features.

37

0.05-µm-THICK IMAGING LAYER

2.0-µm-THICK PLANARIZING LAYER

1.0-µm-HIGH OXIDE STEP

(a)

|← 1 µm →|

0.05-µm-THICK IMAGING LAYER

2.5-µm-THICK PLANARIZING LAYER

1.0-µm-HIGH OXIDE STEP

(b)

|← 1 µm →|
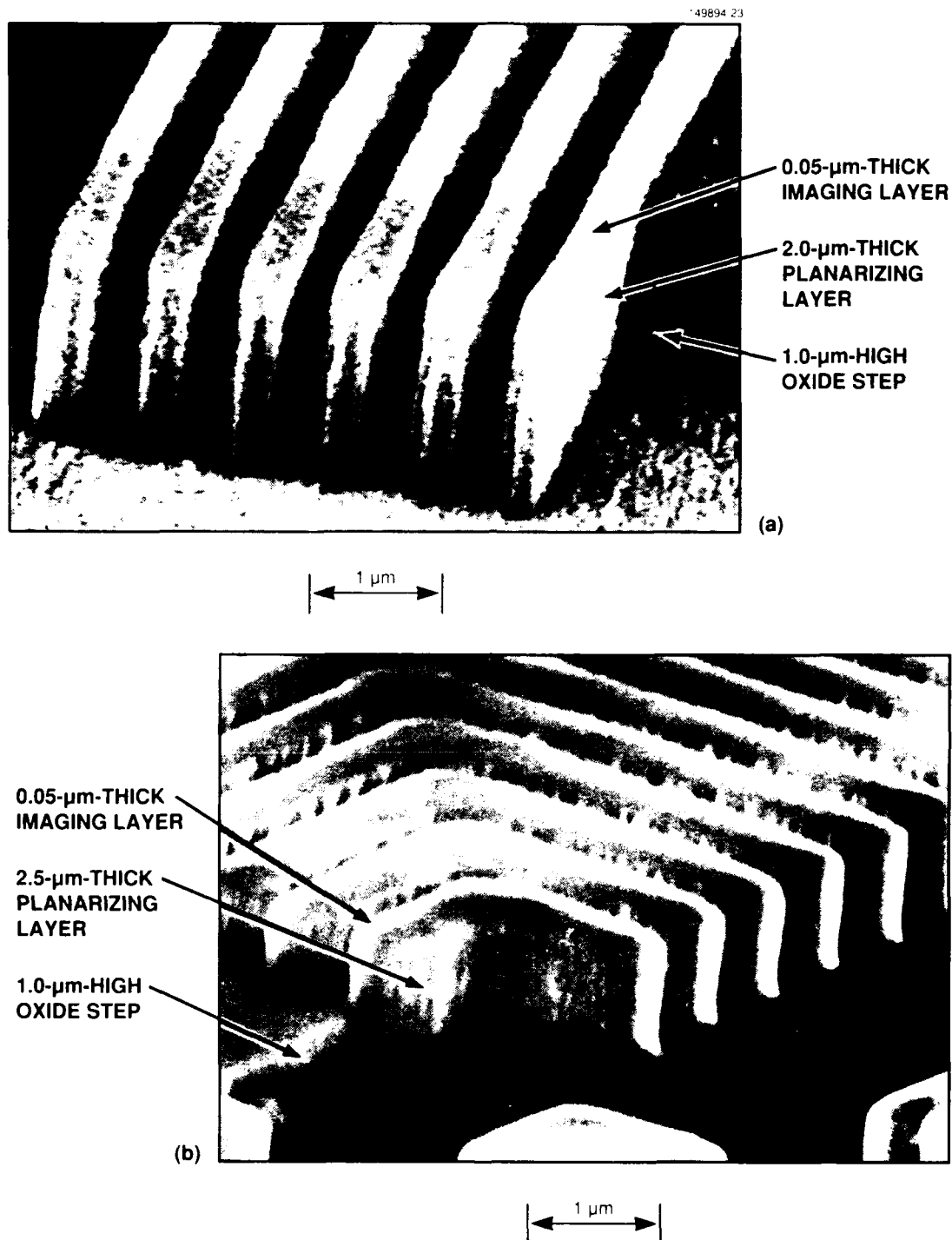
Figure 4-4.   SEMs showing the use of PECVD a-C:H films as planarizing layers in a bilayer resist system for 193-nm submicrometer photolithography. The imaging layers were Si-containing 0.05-µm-thick films deposited on the planarizing layer by (a) spin-on from a solution and (b) PECVD. The imaging layers were then patterned in projection with 193-nm laser radiation, and the pattern was transferred by O_2 RIE at 150-V self-bias.

38

illustrates this effect by comparing the degree of planarization of the PECVD a-C:H films with that of spun-on novolac resist, PMMA, and polyimide, as a function of feature size. Note that the PECVD films retain ~ 85-percent planarization even for the largest features tested (400 μm), whereas that of the spun-on films is between 50 and 75 percent.

The PECVD planarization layers have been used in conjunction with both wet- and dry-deposited inorganic imaging layers in a bilayer resist scheme for excimer laser projection lithography. These a-C:H films are compatible with the imaging layers. They exhibit no thermal or mechanical stress during lithographic exposure, and have excellent adhesion during O_2 reactive ion etching (RIE). Their etch rate in O_2 RIE is similar to that of novolac resists, and they provide better than 40 to 1 selectivity when used with an inorganic imaging layer. Patterns have been defined in inorganic imaging layers using 193-nm projection lithography and transferred through the planarizing layer using O_2 RIE; SEMs of these structures are shown for spun-on and dry-deposited inorganic imaging layers in Figures 4-4(a) and 4-4(b), respectively. The a-C:H planarizing layers were deposited over 1.5-μm-deep oxide steps, and the patterns in the inorganic imaging layers were transferred through the planarizing layer by O_2 RIE at 150-V self-bias.

S.W. Pang
M.W. Horn
R.B. Goodman

4.2 HOMOEPITAXIAL DIAMOND THIN FILMS

Electronic devices in which the semiconducting material is diamond instead of the more commonly used silicon have potentially unique properties, such as high-frequency, high-power operation. However, the fabrication of such devices requires significant process development at several critical stages. A fabrication sequence of an enhancement-mode, recessed-channel metal-oxide-semiconductor field-effect transistor (MOSFET) is shown in Figure 4-5. The important fabrication steps include growth of device-quality undoped and heavily doped homoepitaxial diamond, diamond etching, deposition of a high-quality SiO_2 insulation layer, and formation of ohmic contacts. Techniques for diamond etching [7] and formation of ohmic contacts [8,9] have been developed for years, and are believed not to be limiting factors for the proposed device. Growth of device-quality homoepitaxial diamond [10-12] and the formation of a high-quality SiO_2 layer are comparatively recent developments. The electrical properties of SiO_2 films deposited on diamond have been characterized and are discussed elsewhere [13]. The growth of homoepitaxial diamond is reported here.

A schematic drawing of the diamond growth system is shown in Figure 4-6. It consists of a carbonized 0.5- to 2-mm-diam. tungsten filament placed about 0.5 to 1 cm above a carbon table that holds the diamond substrate. The substrate is kept at a temperature in the range of 750 to 900°C. The gas mixture consists of 3-percent acetone in H_2 at a total pressure of 150 Torr. When doped films are grown, $B(OCH_3)_3$ is added to the gas at an estimated concentration of 5000 ppm, just below that which results in the formation of boron carbide on polycrystalline diamond films. The $B(OCH_3)_3$ is obtained from a saturated solution of B_2O_3 in CH_3OH, through which argon is bubbled and fed into the growth system

INSULATING DIAMOND
SUBSTRATE

STARTING MATERIAL

10^{21} BORON cm^{-3}
UNDOPED

**SEMICONDUCTING
EXPITAXIAL DIAMOND**

DIAMOND ETCHING

SiO$_2$
149894 25

GATE OXIDE

OHMIC
CONTACT
GATE
SOURCE
METAL

**METALLIZATION AND
OHMICS**
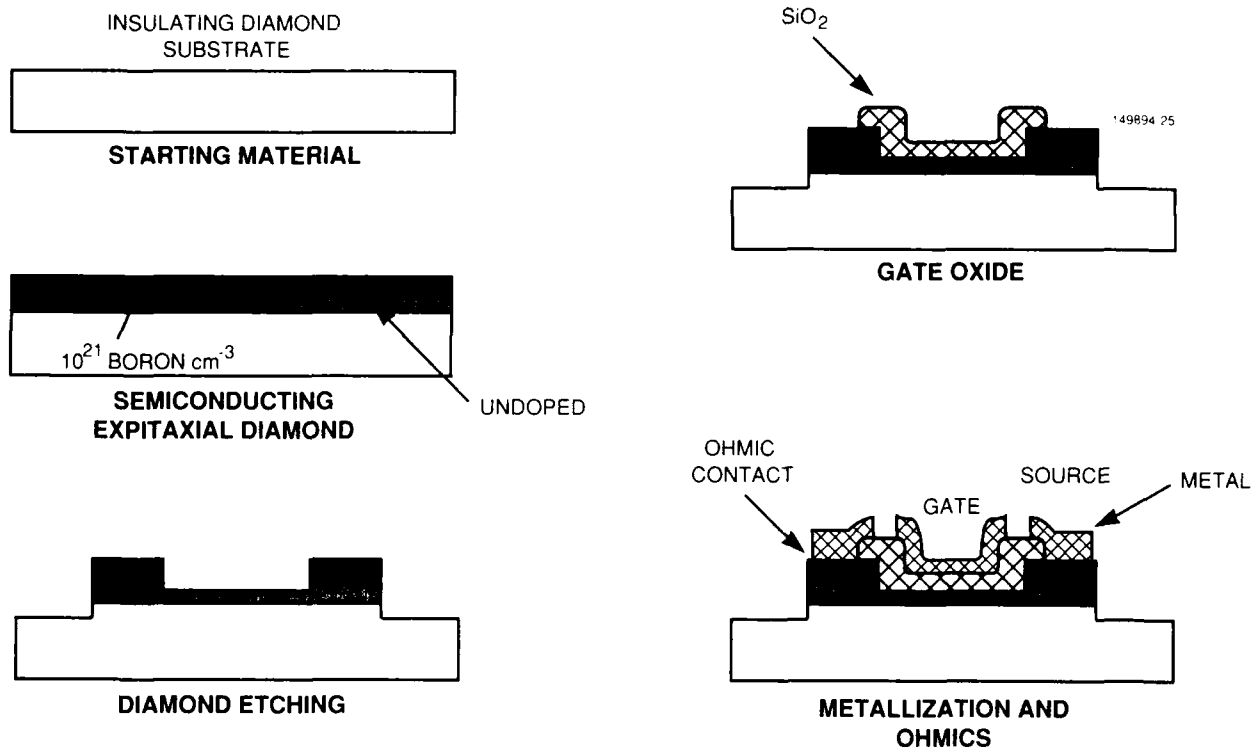
Figure 4-5.   Fabrication sequence of an enhancement-mode, recessed-channel diamond MOSFET.

H$_2$, (CH$_3$)$_2$ CO, B(OCH$_3$)$_3$

149894 26

0.5 - TO 2-mm TUNGSTEN WIRE
2100 TO 2300°C

750 TO 900°C
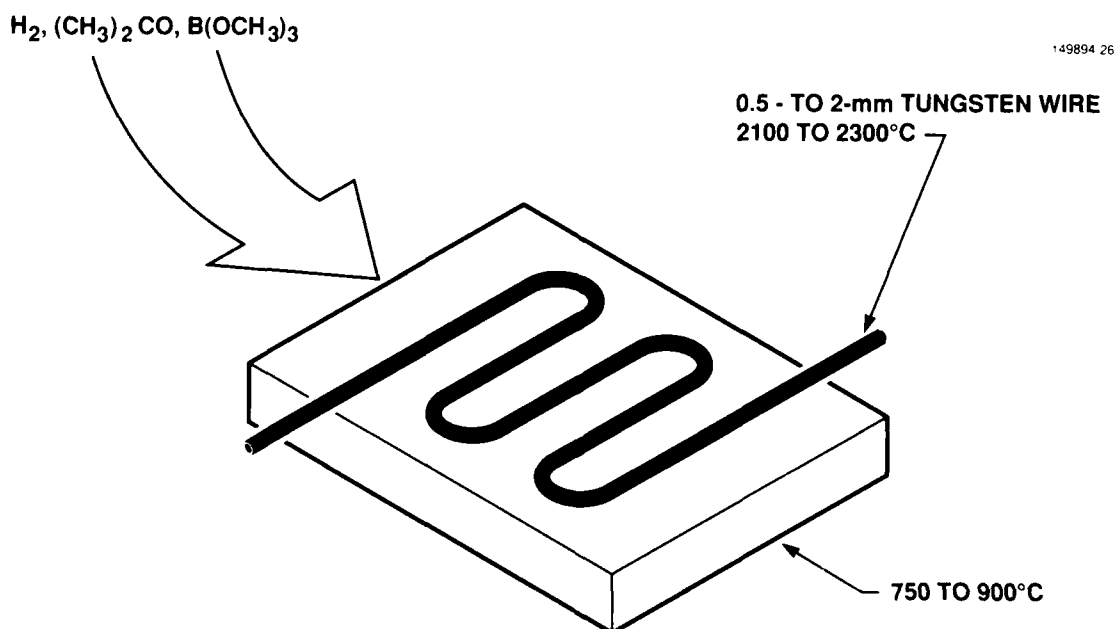
Figure 4-6.   Schematic drawing of the diamond growth system.

40

[14]. The lightly doped layers are obtained without the addition of $B(OCH_3)_3$, and the residual boron from previous experiments dopes the diamond. Figure 4-7 shows the surface morphology of the lightly and heavily doped epitaxial diamond films deposited on substrates oriented along the three principal crystal axes. Under the deposition conditions reported here, only lightly doped films on (100)-oriented substrates have acceptable surface morphology for devices. Heavily doped diamond films on both (100)- and (110)-oriented substrates have acceptable morphology.
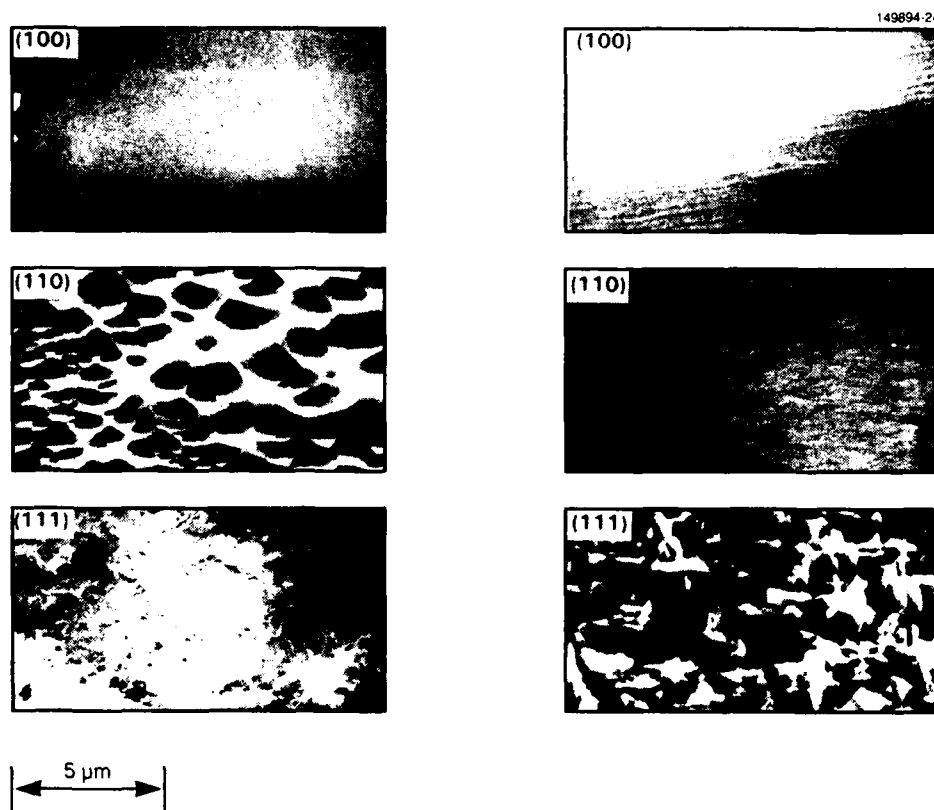
Figure 4-7. SEMs of lightly doped (left) and heavily doped (right) homoepitaxial diamond films. The substrate crystal orientations are indicated in the top left corners.

The epitaxial films have been characterized crystallographically, electrically, and by secondary ion mass spectrometry (SIMS). All films are epitaxial as determined by x-ray diffraction and reflection-electron diffraction. Only heavily doped (111)-oriented films show any indication of twinning as determined by x-ray diffraction. After epitaxial growth the diamond films were thinned from the back by ArF laser ablation [15] and ion-beam-assisted etching [7] and then examined by transmission electron microscopy. The lightly doped films on (100) substrates are defect free except for a few dislocations, with a

41

density $< 10^8$ cm^{-2}, while lightly doped (110)-oriented films contain a large number of dislocations, 5×10^{10} cm^{-2}. The dislocation density of heavily doped films on both (100)- and (110)-oriented substrates is $< 10^9$ cm^{-2}. Other impurities found at lower concentrations are molybdenum at 5×10^{17} cm^{-3} and nickel at 10^{17} cm^{-3}. The molybdenum is an impurity in the tungsten wire, and the nickel is from the stainless steel heat shields in the growth chamber. Table 4-1 summarizes the results of the epitaxial growth.

TABLE 4-1

Boron Concentration, Growth Rate, Room-Temperature Resistivity, and Resistivity-Temperature Activation Energy of Homoepitaxial Diamond Films for the Three Principal Crystal Axes

Substrate Orientation	Boron Concentration (cm^{-3})	Growth Rate (μm h^{-1})	Resistivity at 25°C (Ω cm)	Activation Energy (eV)
(100)	5 3 10^{18}	1.3	7.4 × 10^3	0.39
(110)	10^{19}	6.8	1.7 × 10^3	0.32
(111)	—	1.8	3.1 × 10^2	0.30
(100)	10^{21}	6.6	1.9 × 10^{-2}	< 2 3 10^{-3}
(110)	2 3 10^{21}	14	3.4 × 10^{-3}	< 2 3 10^{-3}
(111)	10^{22}	—	< 2 × 10^{-4}	< 2 3 10^{-3}

In summary, diamond transistors have the potential of higher-frequency, higher-power operation than is attainable with Si or GaAs. The high resistance of lightly doped diamond need not limit the performance of a properly designed device. One such device, the enhancement-mode etched-gate MOSFET, requires the growth of low-resistivity homoepitaxial films, diamond etching, ohmic contact formation, and growth of a device-quality SiO$_2$ layer on the diamond. The growth of both low-resistivity homoepitaxial films and device-quality SiO$_2$ layers on semiconducting diamond have been demonstrated.

M.W. Geis

REFERENCES

1. W.E. Armstrong and D.L. Tolliver, *J. Electrochem. Soc.* **128**, 423 (1981).

2. W. Kern, *RCA Rev.* **34**, 655 (1973).

3. C.Y. Ting, V.J. Vivalda, and H.G. Schaefer, *J. Vac. Sci. Technol.* **15**, 1105 (1978).

4. T. Mogami, M. Morimoto, H. Okabayashi, and E. Nagasawa, *J. Vac. Sci. Technol. B* **3**, 857 (1985).

5. B. Singh, O. Mesker, and D. Devlin, *J. Vac. Sci. Technol. B* **5**, 567 (1987).

6. L.E. Stillwagon, *Solid State Technol.* **30** (6), 67 (1987).

7. N.N. Efremow, M.W. Geis, D.C. Flanders, G.A. Lincoln, and N.P. Economou, *J. Vac. Sci. Technol. B* **3**, 416 (1985).

8. K.L. Moazed, R. Nguyen, and J.R. Zeider, *IEEE Electron Device Lett.* **7**, 350 (1988).

9. M.W. Geis, M. Rothschild, R.R. Kunz, R.L. Aggarwal, K.F. Wall, C.D. Parker, K.A. McIntosh, N.N. Efremow, J.J. Zayhowski, D.J. Ehrlich, and J.E. Butler, *Appl. Phys. Lett.* **55**, 2295 (1989).

10. B.V. Derjaguin, B.V. Spitsyn, A.E. Goridetsky, A.P. Zakharov, L.L. Bouilov, and A.E. Sleksenko, *J. Cryst. Growth* **31**, 44 (1975).

11. M. Kamo, Y. Sato, S. Matsumoto, and N. Setaka, *J. Cryst. Growth* **62**, 642 (1983).

12. M.W. Geis, *Proc. SDIO/IST-ONR Diamond Technology Initiative Symp.* (Crystal City, Va., 1989).

13. M.W. Geis, J.A. Gregory, and B.B. Pate, *IEEE Trans. Electron Devices*, to be published.

14. K. Okano, H. Naruki, Y. Akiba, T. Kurosu, M. Iida, Y. Hirose, and T. Nakamura, *Jpn. J. Appl. Phys.* **28**, 1066 (1989).

15. M. Rothschild, C. Arnone, and D.J. Ehrlich, *J. Vac. Sci. Technol. B* **4**, 310 (1986).

16. A.T. Collins, *Semicond. Sci. Technol.* **4**, 605 (1989).

5. MICROELECTRONICS

5.1 ENERGY-BAND MODEL OF SEMI-INSULATING GaAs GROWN BY MBE AT LOW SUBSTRATE TEMPERATURE

There has been considerable interest in a new GaAs material grown by molecular beam epitaxy (MBE) at low substrate temperature for use as a buffer layer in GaAs integrated circuits [1] and for optical generation of subpicosecond electrical pulses [2]. To achieve the desired insulating characteristics, the low-temperature (LT) GaAs is grown at 200°C and annealed *in situ* at 600°C for 10 min under an arsenic overpressure. Reported here is the first semiquantitative energy-band model to describe the electron and hole conduction in this material.

Some of the characterization techniques and results used to develop the physical model of as-grown and annealed LT GaAs are shown in Table 5-1. Auger electron spectroscopy [3], particle-induced *x*-ray emission [4], and analytical electron microscopy [5] all confirm that LT GaAs is nonstoichiometric with about 1-at.% excess As, both as grown and after annealing. Reflection high-energy electron diffraction [4], *x*-ray diffraction [6], and He ion channeling [4] indicate that the unannealed material is disordered and has a lattice constant slightly larger (~ 0.1 percent) than that of high-quality GaAs. This disorder disappears after annealing even though the 1-at.% excess As remains.

There is no near-bandgap or deep-level photoluminescence in either the as-grown or annealed samples. However, a 1.2-eV peak is observed in the photoluminescence spectrum of a Si-doped GaAs epitaxial layer grown on a LT GaAs [4] epitaxial layer; the peak has been attributed to a Ga vacancy (V_{Ga}) complexed with a Si donor (Si_{Ga}) [7]. This result suggests that Ga vacancies present in the LT GaAs layer outdiffuse into the Si-doped layer during growth.

The IR absorption data for LT GaAs indicate that a very high concentration of deep-donor levels is located ~ 0.75 eV from the edge of the conduction band. The concentration of these levels is less in annealed than in as-grown LT GaAs, but is still unusually high. The IR absorption coefficient α at a photon wavelength λ of 1 μm is 10,000 cm^{-1} and 1000 cm^{-1} for as-grown and annealed LT GaAs, respectively. Electron paramagnetic resonance (EPR) [5] data show a higher concentration (~ 5 × 10^{18} cm^{-3}) of singly ionized arsenic antisite defects in as-grown LT GaAs than reported previously for any GaAs material [6]. This concentration is below the EPR detection limit (1 × 10^{18} cm^{-3}) in the thin annealed LT GaAs layer. Raman scattering measurements [8] of as-grown LT GaAs layers show peaks at 258, 223, 200, 175 and 80 cm^{-1}, in addition to an unusual peak at 47 cm^{-1}, which has only been reported once before in a GaAs Raman spectrum [9]. In annealed LT GaAs only the 223-cm^{-1} peak, attributed to As interstitial (As$_i$) defects, remains. The 200- and 258-cm^{-1} peaks are characteristic of bulk As and are attributed to As microclusters. The 80- and 175-cm^{-1} peaks are attributed to defect-activated first-order Raman scattering and are indicative of disorder.

Temperature-dependent conductivity and Hall-effect measurements are very different for as-grown and annealed LT GaAs. In the temperature range from ~ 180 to 270 K the conductivity of as-grown LT GaAs can be fitted either by a temperature-activated behavior of the form exp ($-E_{h1}/kT$) or by a temperature dependence of the form exp [$-(T_{01}/T)^{0.25}$]. The temperature-activated behavior is consistent with nearest-neighbor hopping [10,11], with an activation energy E_{h1} of ~ 0.17 eV. The exponential

TABLE 5-1

Summary of Material Characterization Parameters of LT GaAs

Technique	Result	
	As-Grown	**Annealed**
Auger Electron Spectroscopy	~1 at.% excess As	~1 at.% excess As
Particle-Induced X-Ray Emission	~1 at.% excess As*	~1 at.% excess As*
Analytical Electron Microscopy	~1 at.% excess As[†]	~1 at.% excess As[†]
Reflection High-Energy Electron Diffraction	Single crystal <3 μm; polycrystalline >3 μm‡	Single crystal <3 μm; polycrystalline >3 μm‡
X-Ray Diffraction	Dilated lattice constant	Normal lattice constant
He Ion Channeling	Highly disordered	Slightly disordered
Photoluminescence	No near-bandgap or deep-level emission	No near-bandgap or deep-level emission
IR Absorption	$\alpha = 10{,}000$ cm^{-1} at $\lambda = 1$ μm	$\alpha = 1{,}000$ cm^{-1} at $\lambda = 1$ μm
Raman Scattering	Peaks at 47, 80, 175, 200, 223 and 358 cm^{-1}	Peak at 223 cm^{-1}
Electron Paramagnetic Resonance	$[As_{Ga}^+] \approx 5 \times 10^{18}$ cm^{-3}	$[As_{Ga}^+] < 10^{18}$ cm^{-3}
Hall Effect and Conductivity σ	For $T < 120$ K, $\sigma \propto \exp[-(T_{01}/T)^{0.25}]$ $(T_{01}^{0.25} \approx 140$ K$^{0.25})$ $\mu \approx 1$ cm^2/V·s For 120 K $< T < 300$ K, $\sigma \propto \exp(-E_{h1}/kT)$ $(E_{h1} \approx 0.17$ eV) or $\sigma \propto \exp[-(T_{01}/T)^{0.25}]$ $(T_{01}^{0.25} \approx 140$ K$^{0.25})$ $\mu \approx 1$ cm^2/V·s For $T > 325$ K, $\sigma \propto \exp(-E_a/kT)$ $(E_a \approx 0.75$ eV) $\mu \approx 1000$ cm^2/V·s	For 100 K $< T < 300$ K, $\sigma \propto \exp(-E_{h2}/kT)$ $(E_{h2} \approx 0.04$ eV) or $\sigma \propto \exp[-(T_{02}/T)^{0.25}]$ $(T_{02}^{0.25} \approx 50$ K$^{0.25})$ $\mu \approx 1$ cm^2/V·s For $T > 325$ K, $\sigma \propto \exp(-E_a/kT)$ $(E_a \approx 0.75$ eV) $\mu \approx 1000$ cm^2/V·s

* As excess decreases monotonically with growth temperature.

† Nonuniform As distribution.

‡ For growth at 200° C.

dependence of the conductivity on $T^{-0.25}$ is consistent with variable-range hopping [10,11], where $T_{01}^{0.25} \approx 140$ $K^{0.25}$. Calculations of single-carrier mobility indicate that in this temperature range the mobility $\mu \approx 1$ $cm^2/V \cdot s$, which is consistent with hopping, but we cannot determine which of the two hopping mechanisms is operative. Below 180 K the carrier mobility remains approximately 1 $cm^2/V \cdot s$ and the conductivity can be fitted only by the exp $[-(T_{01}/T)^{0.25}]$ form, where again $T_{01}^{0.25} \approx 140$ $K^{0.25}$. Above 325 K, the conductivity of as-grown LT GaAs varies as exp $(-E_a/kT)$ with activation energy $E_a = 0.75$ eV and $\mu \approx 1000$ $cm^2/V \cdot s$.

For annealed LT GaAs at temperatures less than ~ 300 K, the conductivity can be fitted equally well by an activated process of the form exp $(-E_{h2}/kT)$ where $E_{h2} \approx 0.04$ eV or by a temperature-dependent process of the form exp $[-(T_{02}/T)^{0.25}]$ where $T_{02}^{0.25} \approx 50$ $K^{0.25}$. As was the case for the as-grown material, $\mu \approx 1$ $cm^2/V \cdot s$ for temperatures less than ~ 300 K. Above 325 K, the temperature dependence of the conductivity of annealed LT GaAs is identical to that of as-grown LT GaAs. For both as-grown and annealed LT GaAs the exponential dependence of the conductivity on T^{-1} is attributed to nearest-neighbor hopping for $T < 300$ K, and to excitation from deep levels to the conduction band for $T > 325$ K.

Figures 5-1 and 5-2 show the semiquantitative density of states and energy band diagram for as-grown and annealed LT GaAs, respectively. The conduction and valence band edges, E_c and E_v, are modeled as identical to those of high-purity GaAs with no band tailing in either band, since none of the characterization measurements have shown evidence for band tailing. The intrinsic energy level E_i is at roughly the center of the bandgap. The energy distribution of the density of states is shown in Figure 5-1(a) for as-grown LT GaAs. From the IR absorption measurements we infer that the density of neutral As antisite–related (As_{Ga}^0-related) defects is about 10^{20} cm^{-3} in as-grown LT GaAs; from the EPR measurements we know that about 5 percent of these defects (~ 5 × 10^{18} cm^{-3}) are singly ionized As_{Ga}-related (As_{Ga}^+-related) defects. The large As_{Ga}-related defect density is depicted as a band in the center of the bandgap (E_c – 0.75 eV). Since only a fraction of the As_{Ga}-related defects are ionized, the Fermi level E_f must be positioned above the middle of the As_{Ga}-related defect band. In Figure 5-1(a), the As_{Ga}^+-related defects are depicted as a lighter shade of gray than the As_{Ga}^0-related defects.

The Mott theory of nearest-neighbor hopping associates the measured activation energy with the width of the defect band in which the hopping occurs [10,11]. Therefore, if nearest-neighbor hopping is the physically operative mechanism in the temperature range from ~ 180 to 270 K, the fit to the as-grown LT GaAs conductivity data yields a value of 0.17 eV for the width of the As_{Ga}-related defect band. For two reasons, we hypothesize that an acceptor concentration of approximately 5 × 10^{18} cm^{-3} must be present in the material. First, the low carrier mobility (~ 1 $cm^2/V \cdot s$) obtained from the conductivity data indicates that for temperatures less than 300 K a hopping conduction mechanism, not free-carrier conduction in the valence or conduction band, is operative. Second, since the electrons from the As_{Ga}^+-related defects are not in the conduction band, they must be bound to compensating acceptors. Because the acceptor concentration in MBE-grown GaAs that is attributable to background impurities is typically of the order of 10^{15} cm^{-3}, impurities alone cannot accommodate the electrons (~ 5 × 10^{18} cm^{-3}) from the As_{Ga}^+ related centers. The strong peak at 47 cm^{-1} in the as-grown LT GaAs Raman spectrum has been tentatively identified as V_{Ga} [8]. For this reason the compensating acceptor is believed to be a V_{Ga} complex, depicted at E_A in Figure 5-1(a). An example of such a V_{Ga} acceptor complex is the V_{Ga}-Si_{Ga} defect discussed above that is known to form an acceptor level in n-GaAs [7].

As $_I$ (Ion Channeling, RS)

As PRECIPITATES (RS)

0.17 eV (Conductivity)

ENERGY

E_c

E_F

E_I

E_A

E_v

$\left[As_{Ga}^{+}\right] \cong 5 \times 10^{18}$ cm^{-3} (EPR)

$\left[As_{Ga}^{0}\right] \cong 10^{20}$ cm^{-3} (IR)

$\left[V_{Ga}\right] \cong 5 \times 10^{18}$ cm^{-3} (RS,EPR,PL)

0.34 eV (PL)

DENSITY OF STATES

(a)

R_3

E_c

R_1

R_2

E_I

E_A

E_v

POSITION

(b)
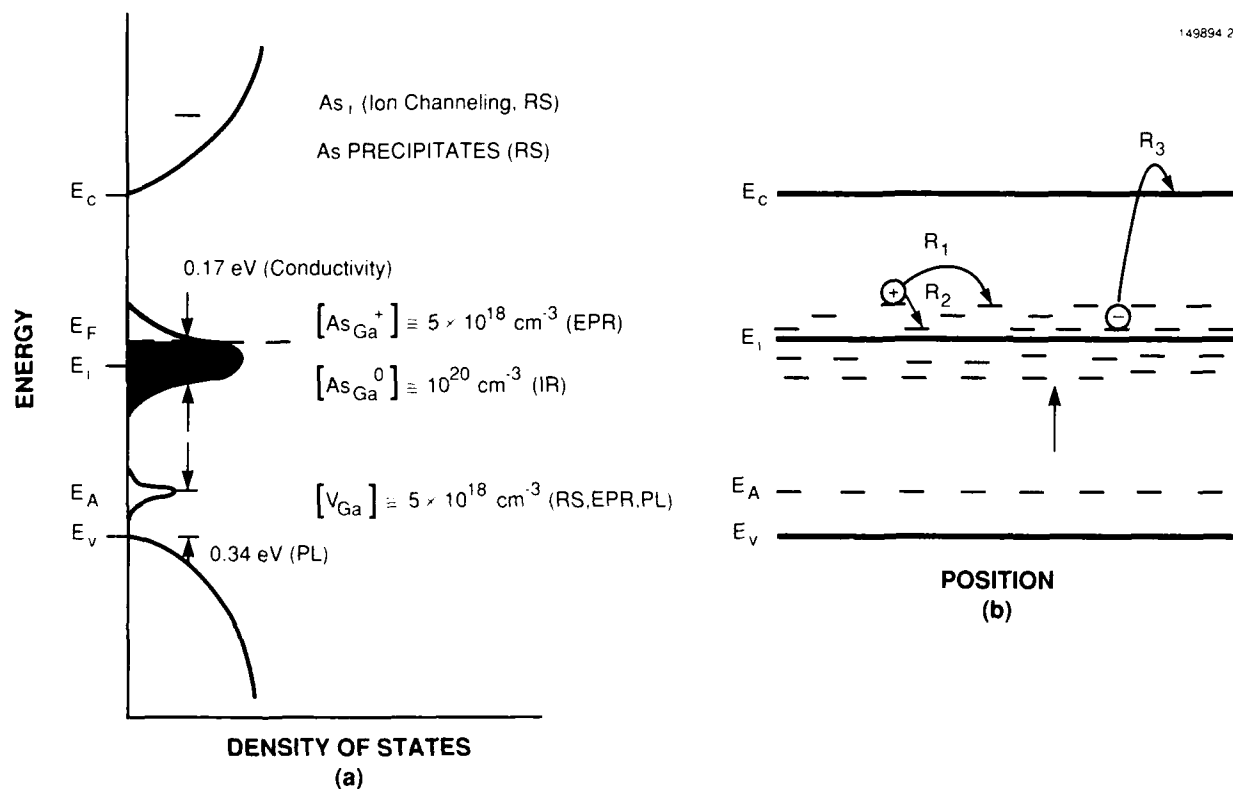
Figure 5-1. Preliminary model for as-grown LT GaAs illustrating (a) semiquantitative density of states and (b) band diagram. The techniques used to identify the defects are shown in parentheses in (a). PL indicates photoluminescence; RS indicates Raman scattering measurements; and R_1, R_2 and R_3 refer to the three conduction mechanisms discussed in the text.

ENERGY

As_i (Ion Channeling, RS)

E_c

0.04 eV (Conductivity)

E_F

$\left[As_{Ga}^+\right] < 10^{18}\ cm^{-3}$ (EPR)

E_i

$\left[As_{Ga}^0\right] \cong 10^{19}\ cm^{-3}$ (IR)

E_A

$\left[V_{Ga}\right] < 10^{18}\ cm^{-3}$ (RS,EPR,PL)

E_v

0.34 eV (PL)

DENSITY OF STATES
(a)

E_c

R_3

R_1

R_2

E_i

E_A

E_v

POSITION
(b)

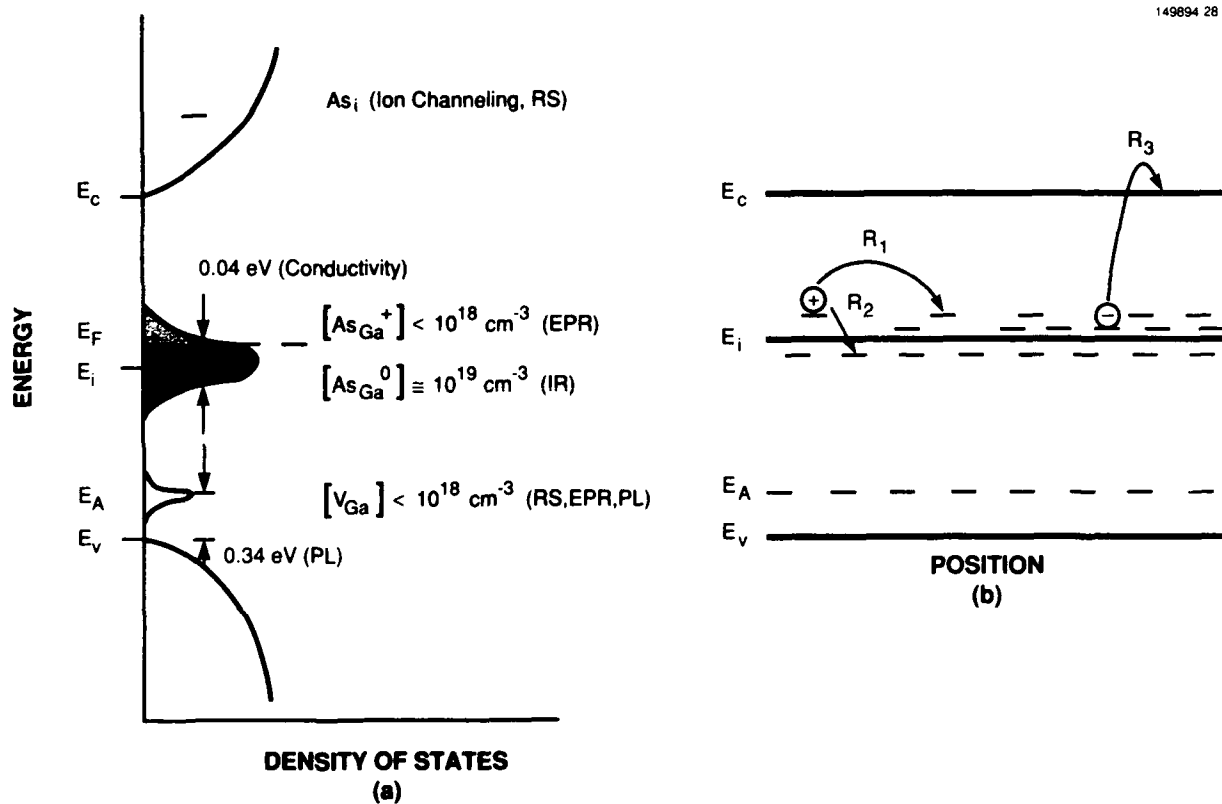Figure 5-2.   Preliminary model for LT GaAs annealed in situ at 600°C for 10 min illustrating (a) semiquantitative density of states and (b) band diagram. The techniques used to identify the defects are shown in parentheses in (a). PL indicates photoluminescence; RS indicates Raman scattering measurements; and R_1, R_2 and R_3 refer to conduction mechanisms discussed in the text.

49

The 1-at.% excess As observed in several characterization measurements, the ion-channeling data, and the Raman scattering data lead to the conclusion that high concentrations of As_I are present in as-grown LT GaAs. Theoretical calculations indicate that the As_I defect should be a donor with an energy level degenerate with the conduction band [4]. This level is indicated in Figure 5-1(a). However, the electrons from these donor levels must also be compensated by acceptors since the Fermi level is in the middle of the bandgap. This fact implies either that the acceptor density is sufficient to compensate the As_I donors or that the As_I defects are complexed with some other lattice defect to form a neutral pair. It is possible that the compensating acceptors are complexes of V_{Ga} and As_I.

The electrical conductivity data of as-grown LT GaAs can be explained by the charge carrier conduction paths shown in the band diagram of Figure 5-1(b). The As_{Ga}-related defect band is depicted as a series of closely spaced discrete energy levels. At low temperatures the conduction mechanism is hole hopping, as depicted by paths R_1 and R_2. Path R_1 symbolizes variable-range hopping and path R_2 represents nearest-neighbor hopping [10]. The hopping species are holes as inferred from the sign of the Hall coefficient. At elevated temperatures (> 325 K) the electrons can ionize from the As_{Ga}^{0}-related centers to the conduction band where they become free carriers. This process is depicted as R_3.

The density of states and energy band diagram of LT GaAs grown at 200°C and annealed *in situ* at 600°C for 10 min are shown in Figure 5-2. Annealing the LT GaAs reduces the crystal disorder, as reflected in the Raman scattering, IR absorption and conductivity measurements. The lattice constant relaxes back to that of GaAs, and the backscattered yield measured by ion channeling decreases. This model is similar to that shown in Figure 5-1 for the as-grown material, but in this case the defect concentrations are substantially lower. From the IR absorption measurements, the As_{Ga}^{0}-related defect density is calculated to be ~ 10^{19} cm^{-3}. Assuming that nearest-neighbor hopping is the physically operative conduction mechanism for annealed LT GaAs at temperatures less than ~ 300 K, we can associate the reduction in the activation energy from 0.17 to 0.04 eV with a commensurate narrowing of the As_{Ga}-related defect band. We have not been able to measure the concentration of the As_{Ga}^{+}-related defect in LT GaAs but know that such defects must be present, since holes are necessary for the hopping conduction mechanism in the As_{Ga}-related defect band. Because the sign of the Hall coefficient indicates that holes are responsible for the measured conductivity, E_f is positioned above the middle of the band, as in Figure 5-1(a). As in the as-grown material, the As_{Ga}^{+}-related defects require a comparable density of compensating acceptors. Although the 47-cm^{-1} Raman peak was not detected in annealed LT GaAs, it is possible that a smaller concentration of V_{Ga}-related acceptors remains. The Raman scattering measurements indicate that the As microprecipitates are removed during the annealing process while the As_I defects remain. The variable-range and nearest-neighbor hopping mechanisms are illustrated by paths R_1 and R_2, respectively, and path R_3 depicts conduction by free electrons, as in Figure 5-1(b). The high resistivity, high breakdown strength, and extremely short minority carrier lifetime of annealed LT GaAs are attributed to the very high density of partially ionized As_{Ga}-related defects located at the center of the GaAs bandgap. The energy band models presented here are consistent with the electronic and optical phenomena observed in these crystals and should present a sound basis for further study of these materials.

F.W. Smith
A.R. Calawa

5.2 INVESTIGATION OF DOPING PROFILE IN Si PBTs FOR HIGH-POWER OPERATION

The effects of variations in doping profiles along the direction of current flow in Si permeable base transistors (PBTs) have been investigated. Previously, we reported the fundamental trade-off between the unity-current-gain frequency f_T and the breakdown voltage V_B for both uniform and nonuniform doping profiles for emitter-up Si PBTs [12]. These profiles are easily obtainable using conventional ion implantation and epitaxial techniques. In this report, the comparison between uniform and nonuniform doping profiles is extended to large-signal performance using a simple class A power analysis following the methods of Kushner [13]. Both the current-voltage (I-V) characteristics and doping profiles are shown in Figure 5-3 together with the assumed load lines. The maximum collector voltage (point C) is limited by avalanche breakdown to 20 V for the uniformly doped device as shown in part (a) and to 30 V for the nonuniformly doped device as shown in part (b) [12]. For class A operation this limits the dc supply voltage (point B) of the uniformly and nonuniformly doped devices to 10 and 15 V, respectively. The maximum collector current I_{max} (point A) is chosen to maximize the output power P_{out} for the uniformly doped device, and the identical I_{max} is chosen for the nonuniformly doped device to simplify the comparison. By assuming a device active area of 4.6×10^{-5} cm^2 (I_{max} = 0.6 A), output powers of 2.25 and 1.5 W for the nonuniformly and uniformly doped devices, respectively, were obtained.

The calculation of large-signal gain G (= P_{out}/P_{in}) is difficult because the input power P_{in} requires precise knowledge of the device equivalent input circuit (including parasitics) and the operating frequency. The relative P_{in} of the two devices is determined from knowledge of the base-voltage swing and average input capacitance along the load lines indicated in Figure 5-3, and assumes the unknown parasitics of the two devices are identical. The smaller base-voltage swing for the uniformly doped device is somewhat offset by its larger average input capacitance, so the input power levels for both devices are within approximately 5 percent of each other. The lower average input capacitance associated with the nonuniformly doped device is consistent with the fact that f_T remains high over its entire voltage range as was shown in the earlier report [12]. If the uniformly doped device is assumed to have a gain G of 14 dB, which is typical for these devices at L-band frequencies, then G calculated for the nonuniformly doped device is approximately 15.7 dB. Note that the nonuniformly doped device has a larger G despite its higher output conductance. This is due to the larger P_{out} achievable with the nonuniformly doped device and is in contrast to the lower maximum small-signal gain one might expect for a device with higher conductance.

The power-added efficiency η_{add} for a class A amplifier can be calculated from the following equation:

$$\eta_{add} = 50 \frac{V_{supply} - V_{sat}}{V_{supply}} \frac{G-1}{G} \quad , \tag{5.1}$$

where V_{sat} is defined by the points designated A on the I-V characteristics of Figure 5-3. Note that V_{sat} is slightly larger for the nonuniformly doped device because of its higher on-resistance. From Equation (5.1), values for η_{add} of 40 and 43 percent are obtained for the uniformly and nonuniformly doped devices, respectively. If I_{max} for the nonuniformly doped device is chosen to provide maximum output
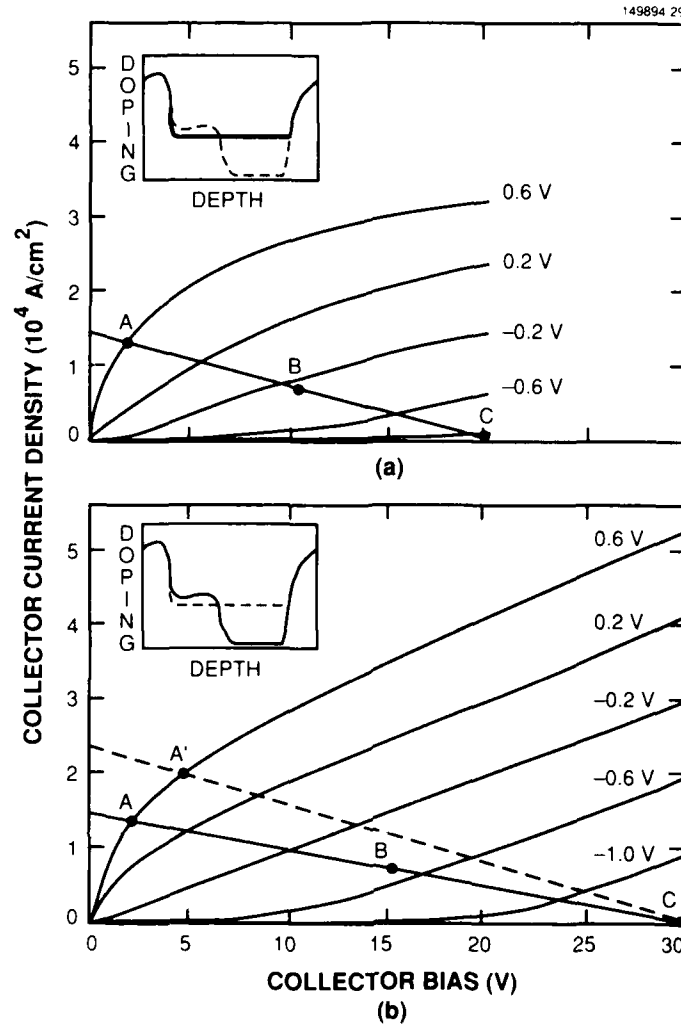
Figure 5-3. Simulated I-V characteristics of (a) uniformly doped and (b) nonuniformly doped etched-emitter PBTs. Load lines in (a) through point A and in (b) through point A' (dashed line) correspond to the maximum output power obtainable for the two devices in class A operation. The second load line in (b) through point A is for the same value of I_{max} as in (a), enabling a comparison of power, power-added efficiency and gain for the two devices.

power [point A' in Figure 5-3(b)] [14], the same analysis yields P_{out} = 2.5 W and G = 16 dB. In addition, the nonuniformly doped device should operate at higher frequencies, because it has a higher average f_T than the uniformly doped device.

<div align="right">D.D. Rathman</div>

5.3 CCD IMAGER WITH INTEGRATED SIGNAL PROCESSORS

A full-fill-factor charge-coupled device CCD (64 × 64) imager with prototype integrated analog signal processors has been fabricated. By combining simple charge-domain, analog signal processors in a parallel, pipelined architecture, an integrated signal processor that performs a simple edge-detection algorithm in real-time has been realized. In particular, object edges in an image can be identified by computing the LoG (Laplacian of Gaussian) of the image [15], which was implemented by convolving the image with a 7 × 7-element mask. The extent of the convolution mask can be increased without decreasing the processor or imager throughput. The parallel, pipelined architecture can be extended to the implementation of nonlinear image filters by proper modification of the processing elements. With a serial output clock rate of 10 MHz, the signal processor is capable of operation at 1000 frames/s. Furthermore, this signal processing capability is implemented with standard CCD technology, without decreasing the fill factor (fraction of on-focal-plane silicon area dedicated to image sensing) of the imager, without significantly increasing power dissipation, and with only a 15-percent increase in chip area. Integration of signal-processing capability with CCD imagers is especially useful for machine vision and robotics applications where real-time image analysis is essential. This prototype device demonstrates the feasibility and potential computational power of incorporating signal processors directly on the imaging device.

Many image-processing algorithms and machine-vision tasks consist of calculations or operations performed on spatially localized neighborhoods. Therefore, the highly parallel nature of these algorithms can be effectively exploited if they are performed directly on the imaging device before the parallel structure of the data is disrupted by serial data output. The parallel, pipelined architecture (Figure 5-4) provides a balance of computational speed, internal clock rate, internal storage, and I/O bandwidth without degrading the imager fill factor. As all columns of image pixel data are shifted simultaneously, local interactions between neighboring column elements are directly performed in parallel. As row values are sequentially clocked through the processor, local interactions between neighboring row elements are similarly performed by using delay elements. This architecture is able to efficiently implement linear convolutions that are separable and recursively defined. It is also suitable for certain types of nonlinear filtering operations that perform image segmentation, a basic machine-vision task.

A photomicrograph of the chip is shown in Figure 5-5. A 4-μm, double-polysilicon, double-metal CCD process was used. The chip is 6.5 × 5.9 mm. For simplicity, a standard frame-transfer imager with 70 × 70-μm pixel size was fabricated. The imager actually occupies 4.5 × 4.5 mm with the signal processor being only 4.5 × 0.65 mm. While the size of the implemented imager and processor was determined by 4-μm design rules, this prototype integrated imager and signal processor is easily scalable and implementable into larger imaging arrays and for more sophisticated image-processing applications. Electrical input capability was incorporated into the device to facilitate initial testing. Functionality of each component of the device was demonstrated. More detailed device testing is in progress, including direct optical sensing and processing.

W. Yang
A.M. Chiang

PARALLEL OUTPUTS

ROW PROCESSORS

COLUMN PROCESSORS

PARALLEL INPUTS

149894 30
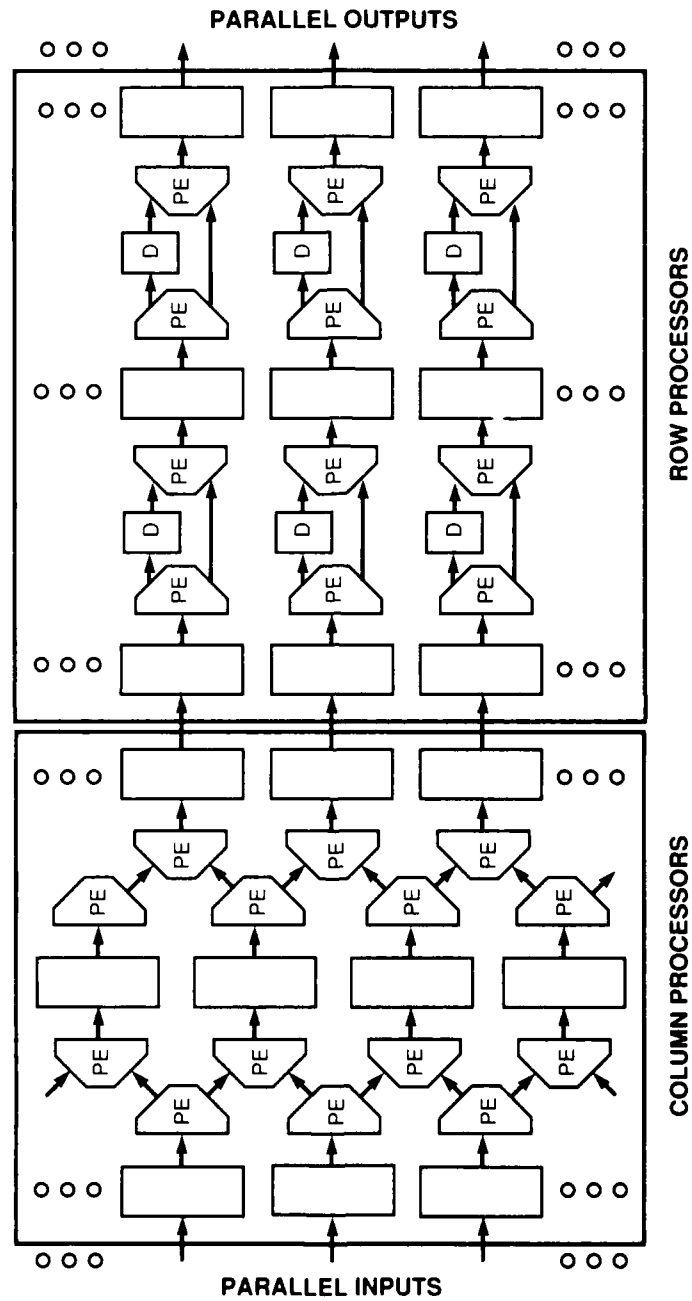
Figure 5-4. Parallel, pipelined processor architecture. Rectangles represent pixel data storage. PE indicates processing element, and D indicates delay.

54

FULL-FILL-FACTOR
CCD IMAGER
(64 × 64)

CCD
PROCESSORS

149894-31
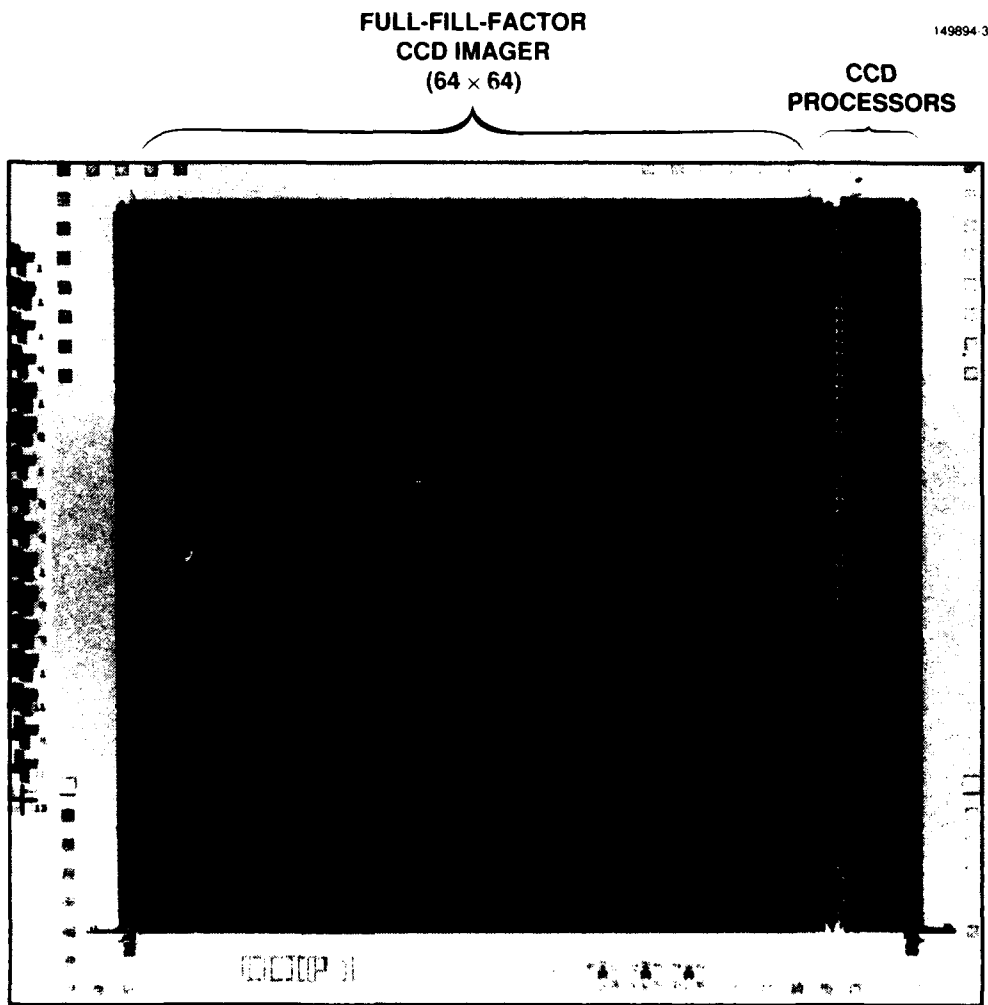
Figure 5-5. *Photomicrograph of the CCD imager and signal processor. Die size is 6.5 × 5.9 mm. A 64 × 64 imager with 70 × 70-μm pixel size has an overall size of 4.5 × 4.5 mm. The prototype signal processor is 4.5 × 0.65 mm or about 15 percent of the imager size.*

REFERENCES

1. F.W. Smith, A.R. Calawa, C.L. Chen, M.J. Manfra, and L.J. Mahoney, *IEEE Electron Device Lett.* **9**, 77 (1988).

2. F.W. Smith, H.Q. Le, V. Diadiuk, M.A. Hollis, A.R. Calawa, S. Gupta, M. Frankel, D.R. Dykaar, G.A. Mourou, and T.Y. Hsiang, *Appl. Phys. Lett.* **54**, 890 (1989).

3. F.W. Smith, C.L. Chen, G.W. Turner, M.C. Finn, L.J. Mahoney, M.J. Manfra, and A.R. Calawa, *IEEE Int. Electron Devices Mtg. Tech. Dig.* (IEEE, New York, 1988), p. 383.

4. F.W. Smith, Ph.D. thesis, MIT (1990).

5. M. Kaminska, E.R. Weber, Z. Liliental-Weber, R. Leon, and Z. Rek, *J. Vac. Sci. Technol. B* **7**, 710 (1989).

6. M. Kaminska, Z. Liliental-Weber, E.R. Weber, T. George, J.B. Kortright, F.W. Smith, B-Y. Tsaur, and A.R. Calawa, *Appl. Phys. Lett.* **54**, 1881 (1989).

7. E.W. Williams, *Phys. Rev.* **168**, 922 (1968).

8. R.S. Berg, N. Mavalvala, F.W. Smith, and A.R. Calawa, submitted to *Phys. Rev. B*.

9. M. Holtz, R. Zallen, O. Brafman, and S. Matteson, *Phys. Rev. B* **37**, 4609 (1988).

10. N.F. Mott and E.A. Davis, *Electronic Processes in Non-crystalline Materials* (Clarendon, Oxford, 1979), Chap. 2.

11. O. Madelung, *Introduction to Solid-State Theory* (Springer-Verlag, Berlin, 1978), Chap. 10.

12. Solid State Research Report, Lincoln Laboratory, MIT (1989:1), p. 51.

13. L.J. Kushner, *Microwave J.* **32**, 103 (1989).

14. J. Obregon, E. Ngoya, M. Campovecchio, and M. Camiade, *Microwaves RF* **28**, 91 (1989).

15. V. Torre and T. Poggio, *IEEE Trans. Pattern Anal. Mach. Intell.* **PAMI-8**, 147 (1986).

6. ANALOG DEVICE TECHNOLOGY

6.1 SUBSTRATE TEMPERATURE MEASUREMENT

The properties of thin films depend strongly on the substrate temperature during deposition. Although many methods have been proposed to measure substrate temperature, a generally applicable method is not available. For substrates that are opaque to the near- or far-infrared, or that can be thermally anchored to a metal block (as in deposition of III-V semiconductors by molecular beam epitaxy) infrared thermometry can be used [1]. However, in many applications the substrate is transparent to infrared radiation, ruling out this method. In these cases, it is common to attach a small thermocouple to the substrate surface, which is an adequate technique provided good thermal contact can be made between the substrate and thermocouple and the thermocouple attachment does not significantly modify the local substrate temperature. Materials that have been used for attaching thermocouples to substrates are high-temperature cement and various gallium alloys [2]. However, while high-temperature cements are stable under high pressures of oxygen, they generally decompose in vacuum, contaminating the film deposition. In addition, these cements do not adhere well to most substrates. Gallium, on the other hand, reacts with most metals, limiting its use to temperatures below 500°C.

The problem of maintaining good thermal contact between the thermocouple and the substrate can be solved by forming the thermocouple directly on the substrate by the sequential deposition of two different metals to form a thin-film thermocouple [3]. However, this method has two shortcomings. First, the emf of the two thin films is usually different from that of the bulk and is extremely sensitive to the deposition method, requiring calibration of each individual sample. Second, the two thin films forming the thermocouple must still be connected to an external voltmeter using a wire-bonding process. The junctions between the bonded wires and the thermocouple films then serve as reference junctions. Consequently, this method is useful in applications such as pulsed laser experiments [4], where the instantaneous local temperature is the quantity of interest. However, for uniformly heated substrates the total emf generated by the thermocouples is zero since there is no temperature difference between the thermocouple junction and the reference junctions.

We have developed a simple and reproducible method to bond thermocouples directly onto a substrate, thus circumventing most of the difficulties of other techniques. It can be applied to most substrates, it assures good thermal contact with the substrate, and it does not require individual calibration of each substrate. In this method, illustrated in Figure 6-1, a small gold pad about 1 μm thick and 2 mm in diameter is evaporated onto a substrate using a metal mask. Depending on the substrate, a thin layer (30 nm) of chromium or titanium may be evaporated prior to formation of the gold pad to promote adhesion of the gold to the substrate. Two 25-μm-diam. thermocouple wires are ultrasonically bonded to the gold pad. The two thin wires are very fragile and, for convenience, they are connected to thicker extension wires having the same thermoelectric properties. These wires are then brought out of the deposition system through a vacuum feedthrough also made of a material having the same thermoelectric
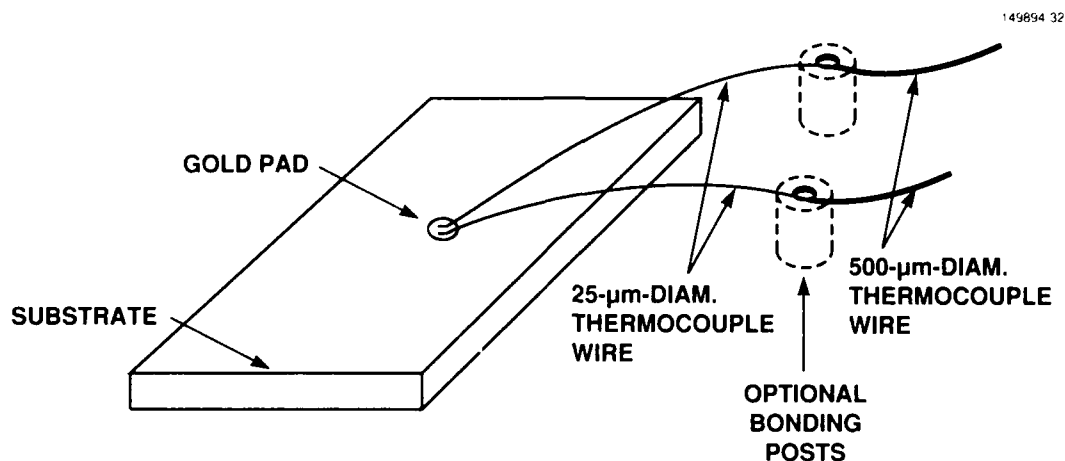
Figure 6-1. Configuration for measurement of substrate temperature using 25-μm thermocouple wires.

properties as those of the thin wires attached to the substrate. The thin wires are made of two different Au-Pt-Pd alloys (14, 31 and 55 percent; 65, 0 and 35 percent) commercially known as Platinel II thermocouple alloys [5]. These alloys were chosen for the following reasons:

1. They do not work harden as do most other thermocouple alloys. This allows the use of ultrasonic bonding for attaching the thermocouple to the gold pad.

2. They have a large thermopower very similar to that of a Chromel-Alumel pair, allowing the use of these less expensive thermocouple wires as expensive thermocouple wires as extension wires.

3. Their thermal resistance is large compared with that of ultrasonically bondable elemental wires.

4. They are stable in both vacuum and oxidizing atmospheres.

Since the positive and negative legs of the thermocouple are both bonded directly to the gold pad and not on top of each other, the thermocouple junction is formed at the interface of the wires with the gold pad, and the emf measured between the two wires is a true indication of the substrate temperature at the substrate surface. The only source of error is the local change in temperature created by the thermocouple itself. To calculate this disturbance we must know the heat conductivity σ and emissivity ε of both the substrate and the thermocouple wires, which are not known in most situations. Assuming reasonable values for these parameters (wire properties $\varepsilon_v = 0.2$ and $\sigma_w = 20$ W m^{-1} K^{-1}, substrate properties $\varepsilon_s = 0.8$ and $\sigma_s = 20$ W m^{-1} K^{-1}), we find a maximum difference of 1°C for a substrate temperature of 700°C. In these calculations we have not taken into account the increase in temperature resulting from the lower emissivity of the gold pad compared with that of the substrate, so the actual error will be even lower.

To verify the validity of the method and to evaluate the stability of the thermocouple, we constructed the small vacuum oven sketched in Figure 6-2. The substrate rests on a lower plate that is heated
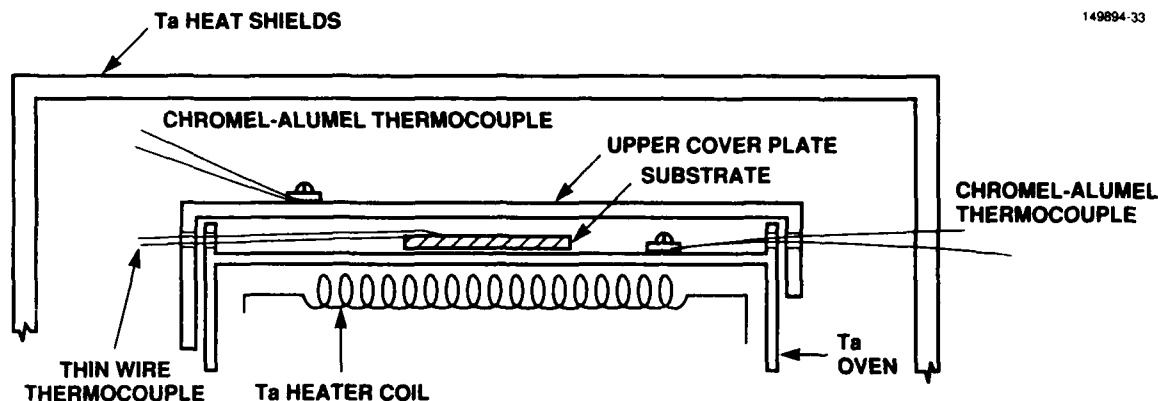
Figure 6-2. Vacuum oven for thermocouple calibration.

by a Ta resistance coil. The top surface is covered by an upper plate, and two Ta heat shields surround the heated surfaces. The temperatures of the upper and lower plates were measured using standard Chromel-Alumel thermocouples while the substrate temperature was measured using our new method and published values for the emf of Platinel II thermocouples.

For an upper-plate temperature T_{up} = 1009 K and a lower-plate temperature T_{low} = 1075 K, we measured a substrate temperature T_s = 1043 K. The substrate temperature was compared with calculations made using the Stefan-Boltzmann law. Assuming that the only heat transfer between the lower plate, the substrate, and the upper plate is due to radiation [6], we modeled our system as radiant heat transfer between three infinite parallel plates, in which the temperatures of the upper and lower plates are held constant. Under steady state conditions, the heat flux from the lower plate to the substrate equals the flux from the substrate to upper plate, which allows the substrate temperature to be calculated. On the assumption that the emissivity of the upper and lower plates is the same and that the two sides of the substrate have the same emissivity, T_s is related to T_{up} and T_{low} by

$$T_{up}^4 + T_{low}^4 = 2T_s^4 \qquad (6.1)$$

For T_{up} = 1009 K and T_{low} = 1075 K this yields T_s = 1044 K, which is in excellent agreement with our experimental value.

To evaluate stability, we monitored T_s while keeping the T_{up} and T_{low} constant for up to 5 h. The emf was constant and indicated a T_s of 775°C. For our application we do not expect the substrate temperature to exceed 700°C; hence, the stability of the thermocouple is satisfactory.

A.C. Westerheim
A.C. Anderson

6.2 SINGLE-TARGET SPUTTERING OF Y-Ba-Cu-O

Films deposited by *in situ* methods, where the substrate is heated to temperatures high enough to promote film crystallization during deposition, can produce Y-Ba-Cu-O thin films with excellent properties. Laser-pulsed evaporation [7,8] and sputtering [9-13] as well as simultaneous evaporation [14] have been used for this purpose.

The first investigators, attempting to deposit films from stoichiometric targets [9], observed that the composition of the films differed markedly from that of the target. These differences were explained as resulting from film bombardment during deposition by fast negative ions formed at the target surface and accelerated toward the films by the electric field in the space-charge region next to the cathode. Three basic approaches have been used to circumvent this problem. The first [10] utilizes very high pressures during deposition in order to thermalize the fast oxygen atoms. A second approach [11,12] uses an off-axis geometry where the substrate is placed away from the path of the negative ions. Geerk's group in Karlsruhe [13] pioneered a third approach in which a cylindrical target is employed, with the substrate placed perpendicular to the cylinder axis.

We have used the off-axis configuration to deposit films on different substrates by RF magnetron sputtering using a stoichiometric target (Figure 6-3). A 3-in.-diam. commercial magnetron assembly was modified by reducing the gap between the cathode and ground shield to allow operation at higher pressure (up to 200 mT) and by changing the magnetic field configuration to obtain a more uniform sputtering of the target. Substrates of lanthanum aluminate ($LaAlO_3$), lanthanum gallate ($LaGaO_3$), strontium titanate ($SrTiO_3$), yttria-stabilized zirconia (YSZ) and magnesium oxide (MgO) were used, but the films deposited on $LaAlO_3$ had superior properties and are the only ones discussed in this report. Substrate temperatures were kept between 660 and 730°C since the substrate temperature uniformity is critical for reproducible results. The sputtering atmosphere consisted of a mixture of argon and oxygen. Argon pressures between 50 and 100 mT and oxygen pressures between 30 and 75 mT were used. The RF power varied between 100 and 250 W although most films were deposited at 125 or 150 W. The position of the target relative to the substrate is indicated by x and y in Figure 6-3; x was varied between 5.0 and 7.0 cm and y between 3.5 and 7.0 cm. Immediately after sputtering, 100 Torr of oxygen was admitted to the chamber while the substrate temperature was lowered to 400°C. The sample was kept at this temperature for 20 min.

X-ray diffraction patterns of all films indicated strong c-axis orientation (Figure 6-4). Most films had c-axis lattice constants different from bulk value (1.1688 nm) with 1.1660 nm $< c <$ 1.1783 nm. Even at enhanced sensitivities we could not find any evidence of a-axis orientation. Films less than 300 nm were smooth while the topography of thicker films was a strong function of the substrate temperature and the relative position of the substrate and target. Films deposited onto hotter substrates (720°C) usually had higher transition temperatures (up to 86 K) but their surface was rough (100 nm rms for a 500-nm-thick film), while films deposited at lowest temperatures (660°C) were featureless but had lower transition temperatures near 77 K.
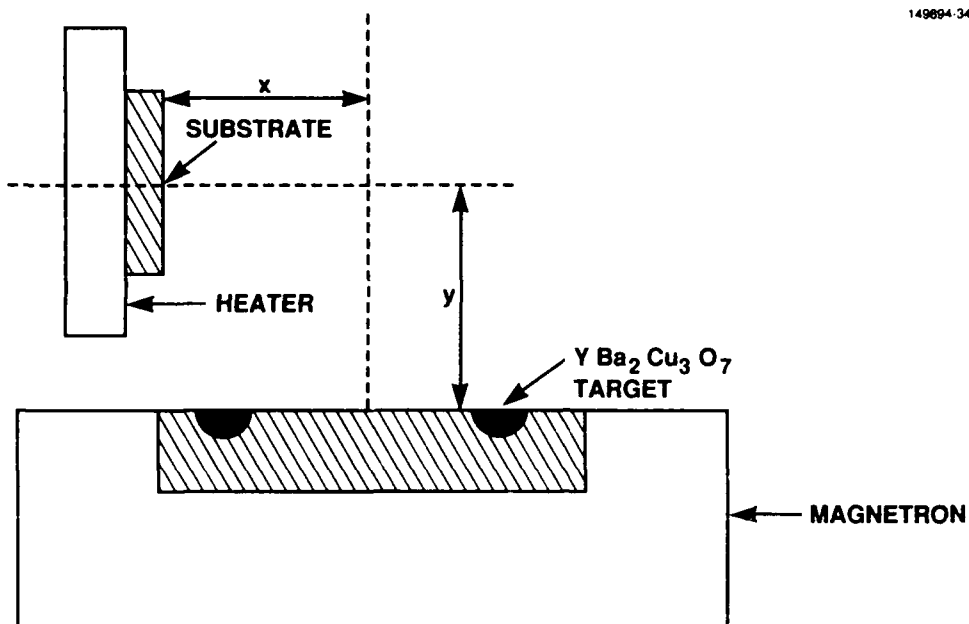
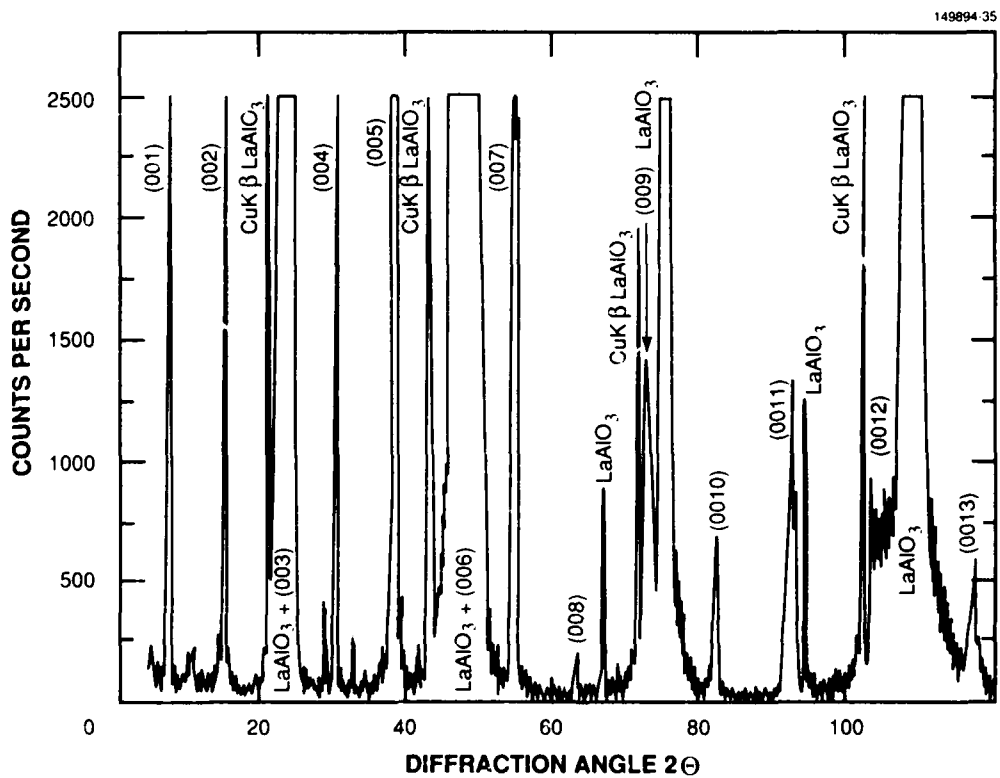Figure 6-3.   Configuration for off-axis sputtering.

Figure 6-4.   X-ray diffraction pattern of a film deposited on LaAlO₃. The large peaks are due to the substrate.

61

Figure 6-5 is a plot of resistivity as a function of temperature for three films. Curve a is for a 16-nm-thick film deposited onto a 700°C substrate. The critical temperature T_c at zero resistivity is 80 K, indicating very little reaction of the film with the substrate. Curve b is for a 210-nm-thick film deposited at 700°C. This film was patterned into a 38-μm-wide line to measure the critical current, which is plottted vs temperature in curve b′ of Figure 6-5. This film had the same T_c and resistivity before and after patterning. Its resistivity at 90 K (150 $\mu\Omega$ cm) is higher than for single crystals (50 $\mu\Omega$ cm). Characteristic c is for a 350-nm-thick film deposited at 720°C. The portion of the curve above T_c extrapolates to zero resistivity at zero temperature. This is an indication that the grain boundaries have temperature-independent resistivity that is much smaller than the temperature-dependent resisitivity of the grains. The resistivity of this film at 90 K (58 $\mu\Omega$ cm) was only slightly higher than for single crystals. The film was patterned onto a 100-μm-wide line, but its current density could not be measured because the currents were so high that the contact resistance heated the film.
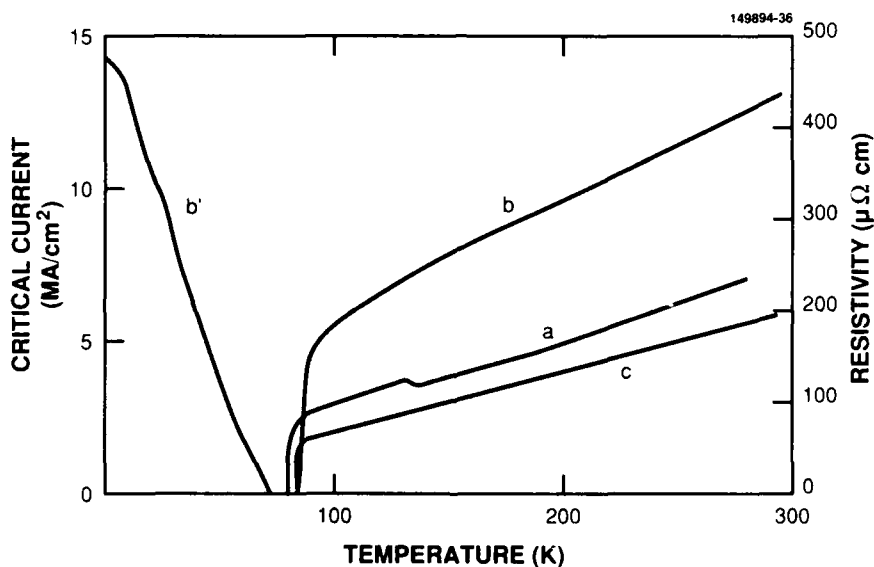

Figure 6-5. Variation of resistivity with temperature for a 160-Å film deposited at 700°C using a dc power supply (curve a), a patterned 2100-Å film deposited at 700°C (curve b), and a 3500-Å film deposited at 720°C (curve c). The critical current vs temperature for the film of curve b is depicted on the left (curve b′).

The surface resistance of a series of films deposited onto rectangular substrates (1.27 × 2.54 cm) was measured as a function of frequency using a stripline method described previously [15]. The best results, shown in Figure 6-6, are for a film deposited at 680°C. The transition temperature of this film was not measured, but the transition temperature of a film deposited under similar conditions was 77 K. Because the central conductor and upper ground planes of the stripline used in this method are made of Nb, all measurements of single films shown in Figure 6-6 were made at 4.2 K. To obtain the temperature
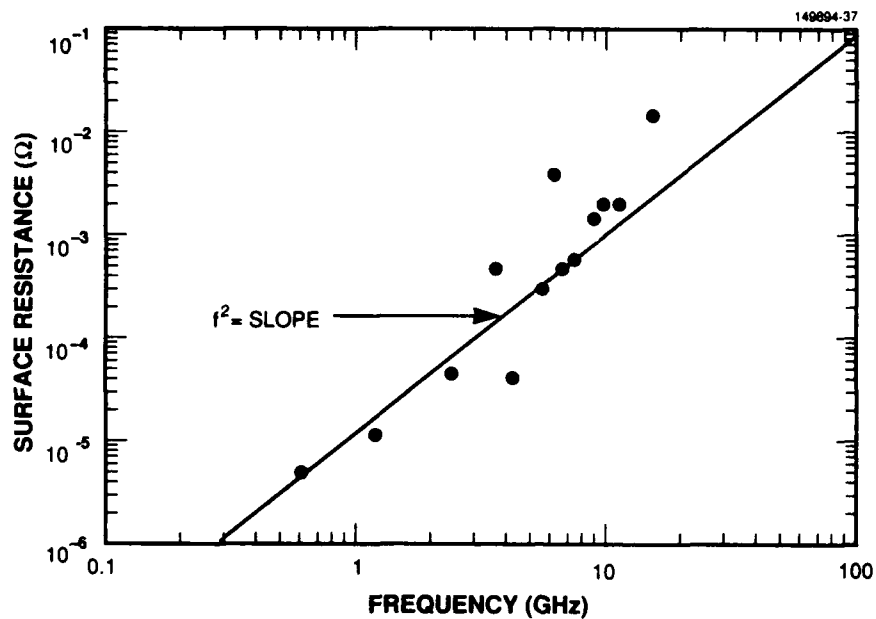
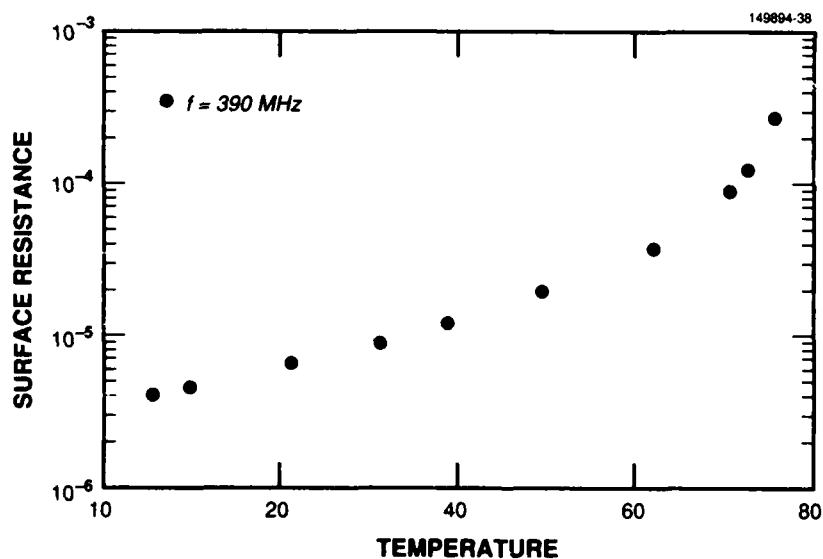*Figure 6-6.   Surface resistance as a function of frequency for a film deposited at 680°C.*

Figure 6-7.   Average surface resistance as a function of temperature for three films deposited under similar circumstances at 370 MHz. One film, deposited at 700°C, was patterned to form the central conductor of a stripline resonator, and the other two films were used as ground planes. Most of the losses are due to the center conductor.

63

dependence of the surface resistance [16], a resonator was made using three films of Y-Ba-Cu-O deposited under similar circumstances. The central conductor for the stripline resonator was defined in one of the films using conventional photolithography and etched using a 0.25-percent phosphoric acid solution that was sprayed onto the substrate. Silver contacts 8000 Å thick were formed by liftoff and annealed at 400°C for 1 h. The variation of the surface resistance of these films as a function of temperature is shown in Figure 6-7. The transition temperature for these films extrapolated from the RF results is 81 K.

A.C. Anderson   R.L. Slattery
D.E. Oates   W.G. Lyons

6.3 HIGH-TEMPERATURE SUPERCONDUCTIVE MICROSTRIP FILTERS

The newly discovered high-temperature superconductors (HTSs) offer great potential for passive microwave applications. The surface resistance of HTS materials, in particular Y-Ba-Cu-O, has been dramatically reduced recently as the quality of thin films of these materials has improved. Typical values of surface resistance at 4 GHz are better in state-of-the-art films than in copper by a factor of 10 at 77 K and a factor of 100 at 4.2 K [16], offering the possibility of substantial improvement in microwave device performance by utilizing HTS material in place of normal metals such as gold.

To demonstrate the potential performance benefits of HTS materials, we chose a four-pole Chebyshev bandpass design for implementation in Y-Ba-Cu-O. The design is a microstrip configuration with a signal line and a ground plane on opposite sides of a single substrate. Two types of growth techniques were used to deposit thin films of Y-Ba-Cu-O. In the first, amorphous Y-Ba-Cu-O is deposited on a substrate by coevaporation of BaF_2, Y and Cu, followed by a postdeposition annealing, typically at 850°C, in flowing O_2 containing H_2O vapor [17]. In the second, Y-Ba-Cu-O film deposition is accomplished *in situ* using off-axis single-target sputtering [12], with substrate temperatures typically kept between 600 and 700°C.

Both techniques can be applied to produce large-area films with good uniformity to at least a 2-in. diameter. Uniformity is crucial in obtaining low values of surface resistance and correspondingly good microwave device performance. The postannealment process can also be used to produce films on both sides of a substrate by annealing both sides simultaneously, while the current *in situ* sputtering process is limited to single-sided film production because silver paste is used to mount the back side of the substrate to the substrate heater block. Furthermore, the nonequilibrium nature of *in situ* growth often results in films with multiphase inclusions and uniformly distributed defects, which in turn act to slightly depress the superconducting transition temperature of the HTS films. Transition temperatures of 87 K for Y-Ba-Cu-O have been demonstrated using an optimized *in situ* off-axis single-target sputtering process [17], compared with typical transition temperatures of 91 K for postannealed Y-Ba-Cu-O films. In addition to producing HTS filters utilizing these two thin-film technologies, we have fabricated all-gold and all-niobium versions of the microstrip filters in order to verify device performance.

Lanthanum aluminate ($LaAlO_3$) was selected for the 1.3 × 2.3-cm microstrip substrate since this material has low-loss microwave properties and is chemically and structurally similar enough to Y-Ba-Cu-O that high-quality thin films of Y-Ba-Cu-O can be grown on the polished surface of $LaAlO_3$.

The dielectric constant of this perovskite material (ε_r = 24.5) is larger than that which the microwave circuit design routines Touchstone and Supercompact can treat with accuracy, so it was necessary to optimize the filter empirically using gold metallization. The filter was designed for a center frequency of 4 GHz and a 3-percent passband. The device was optimized on 500-μm-thick LaAlO$_3$ and functioned with a slightly narrower passband on 425-μm-thick LaAlO$_3$. After the design had been optimized, an all-niobium filter was fabricated as a reference for the performance of the HTS filters. Fabrication of the signal lines on the all-gold filters was accomplished by plating through a photoresist mask. For the all-niobium filters, niobium was deposited by sputtering and the signal line was patterned by reactive-plasma etching.

The three HTS filters that were fabricated are a double-sided postannealed filter with a Y-Ba-Cu-O signal line and ground plane, a single-sided postannealed filter with a patterned Y-Ba-Cu-O signal line and a silver ground plane, and a single-sided filter grown *in situ* with a Y-Ba-Cu-O signal line and a silver ground plane. The device processing for the double-sided postannealed filter began with formation of 300 nm of Y-Ba-Cu-O on the front and back sides of a 0.0425 × 1.3 × 2.3-cm LaAlO$_3$ substrate. A 3-μm silver film was evaporated over the Y-Ba-Cu-O on the ground-plane side of the device. Patterning of the signal line was accomplished with standard AZ1470 photoresist, overexposed to reduce development time in KOH. The Y-Ba-Cu-O was patterned using a spray etch of 0.25-percent H$_2$PO$_4$, which was found to be successful in preventing the residual film formation typically seen with other wet-etching methods. Undercutting of 1 to 2 μm is observed with this etch but is not significant since the minimum feature size on the filter is 66 μm, the size of the gap of the input couplers. A trilayer resist (PMMA/Ti/AZ1470) and liftoff process were used to pattern 1.5-μm-thick silver contacts on the signal line. Low-resistance ohmic contacts to the ground plane and signal line were produced by annealing the structure at 400°C in flowing O$_2$. Final packaging was performed using ultrasonic wedge bonding of aluminum ribbon directly to the annealed silver ohmic contacts on the signal line. For the single-sided postannealed filter and for the filter grown *in situ*, the ground plane side was left bare until after the annealing of the ohmic contacts on the signal line. A 4-μm silver film was then evaporated for the ground plane. Figure 6-8 is a photograph of the final packaged filter.

Performance measurements of the all-gold and all-niobium versions of the filter are shown in Figure 6-9. The characteristics for both filters were consistent with design goals. The conductor losses in the gold filter broaden the filter skirts and cause additional loss in the passband. Reflection measurements show return loss better than 10 dB over the entire passband for both types of filters, and return loss better than 16 dB at the insertion loss measurement frequency. The packaging did not influence the filter response and, except for harmonics of the passband, better than 50-dB out-of-band rejection was obtained up to 20 GHz. Design simulations indicate that the gold version of the filter would have a 2.5-dB insertion loss at 77 K.

Results at 77 K for the HTS filters are shown in Figures 6-10, 6-11, and 6-12. Figures 6-10 and 6-11 illustrate the transmission characteristics of the double- and single-sided postannealed filters, respectively. These two filters were fabricated on 425-μm-thick substrates and as a result have a slightly narrower passband than the 3-percent passband of the design. The double-sided device demonstrated insertion loss of 0.3 ± 0.1 dB at 77 K and less than 0.1 dB at 13 K. The single-sided device had insertion
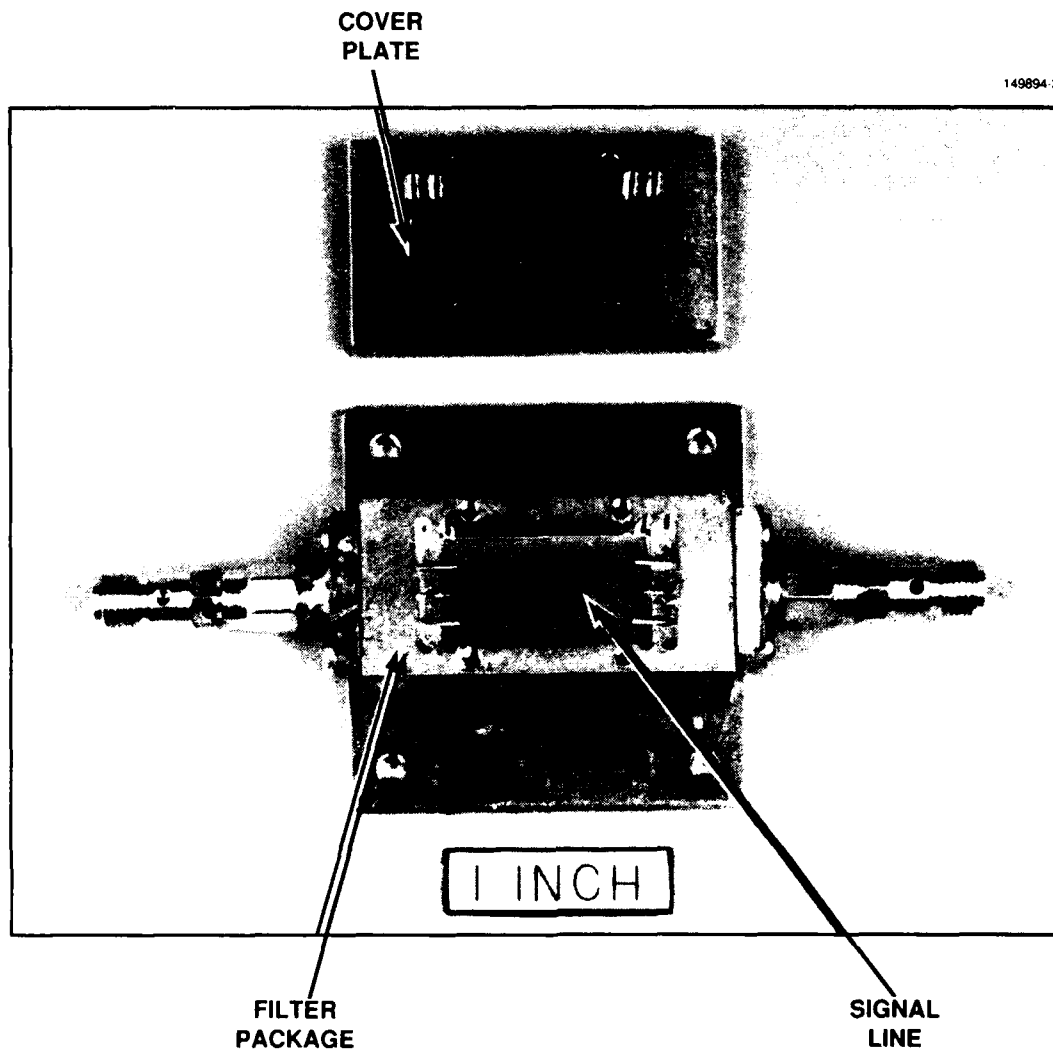
COVER
PLATE

149894-39

I INCH

FILTER
PACKAGE

SIGNAL
LINE

Figure 6-8.   Superconductive microstrip filter. The filters were fabricated on LaAlO$_3$ substrates using gold, niobium and Y-Ba-Cu-O signal lines.

loss of 0.4 ± 0.1 dB at 77 K and less than 0.1 dB at 7 K. For both filters, reflection measurements showed return loss better than 10 dB over the entire passband and better than 16 dB at the insertion loss measurement frequency, which were the same as for the gold and niobium versions. At 77 K the performance of the double-sided device was only 0.1 dB better than that of the single-sided device; the use of a superconducting ground plane is clearly not crucial. This was expected since most of the losses in this filter design occur in the signal line rather than in the ground plane. However, more aggressive filter designs with substantially greater sensitivity to conductor losses will require two-sided film deposition.
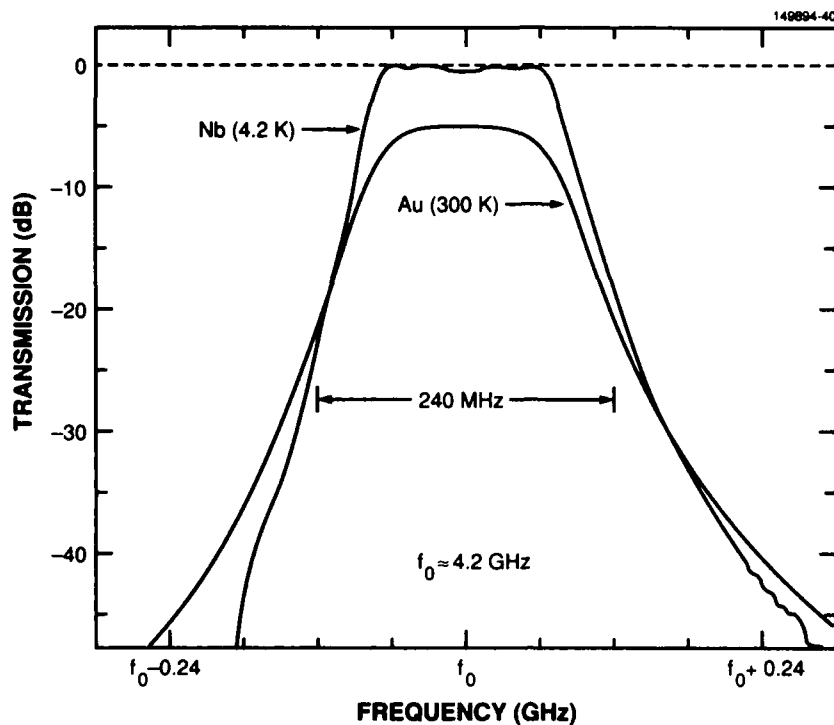
Figure 6-9. Measured transmission response of an all-gold filter at 300 K and of an all-niobium filter at 4.2 K. These filters were fabricated on a 500-μm-thick LaAlO$_3$ substrate. The niobium filter has less than 0.1-dB passband insertion loss while the gold filter has 5-dB insertion loss.
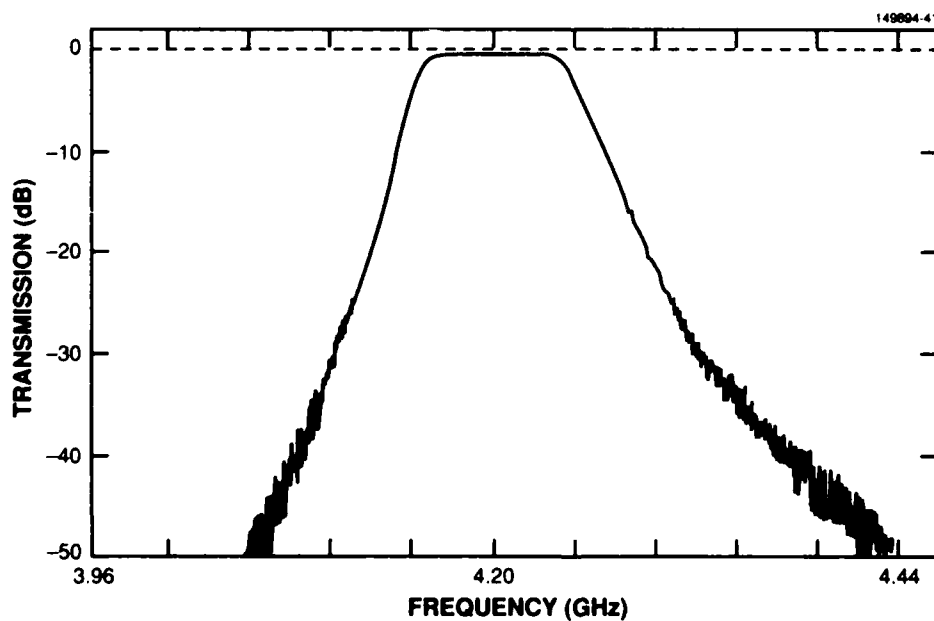

Figure 6-10. Measured transmission response at 77 K of a filter fabricated with a postannealed Y-Ba-Cu-O signal line and ground plane on a 425-μm-thick LaAlO$_3$ substrate. Passband insertion loss is 0.3 dB.
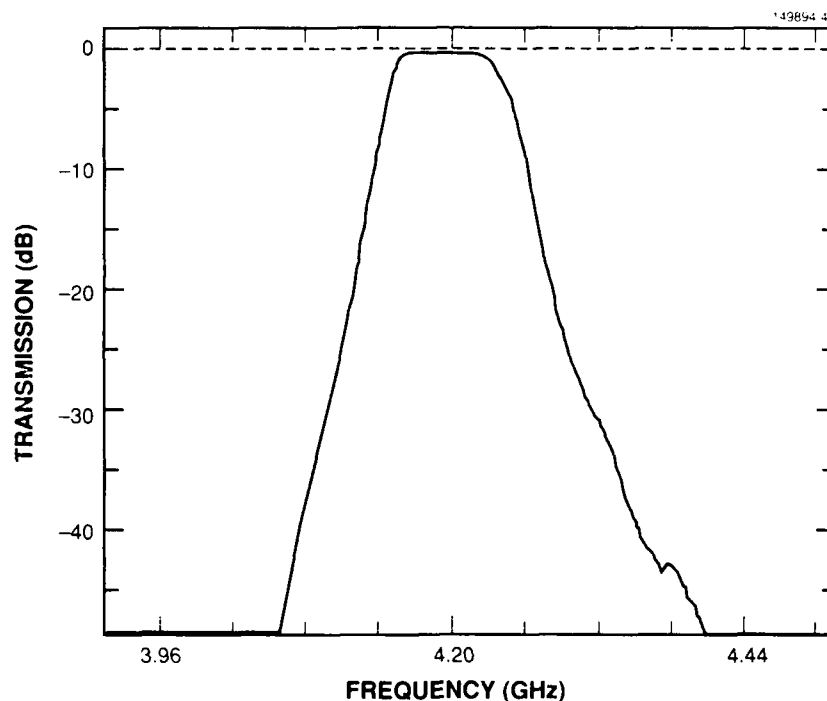
67

Figure 6-11. Measured transmission response at 77 K of a filter fabricated with a postannealed Y-Ba-Cu-O signal line and a silver ground plane on a 425-μm-thick LaAlO$_3$ substrate. Passband insertion loss is 0.4 dB.

The performance at 77 K of the single-sided filter grown *in situ* is shown in Figure 6-12. This filter has an insertion loss of 1.7 dB at 77 K due to the depressed transition temperature of the Y-Ba-Cu-O films. This performance is still better than the 2.5-dB insertion loss of a gold filter at 77 K. The temperature-dependent response indicates a transition temperature of 82 K for the filter grown *in situ*, compared with an inferred transition temperature of 91 K for the postannealed filters. The single-sided device grown *in situ* had insertion loss of 0.3 ± 0.1 dB at 69 K and less than 0.1 dB at 9 K. Measured return loss over the entire passband was better than 10 dB at temperatures up to 69 K. At 77 K there was some degradation in the return-loss performance as well as an observed 80-MHz shift of the center frequency due to the increased penetration depth in the superconductor as the transition temperature is approached.

Because operation at the liquid-nitrogen temperature of 77 K is important for many applications, the postannealment process has the distinct advantage of typical transition temperatures of 91 K over large-area films, while our *in situ* sputtering technique is currently producing large area films with depressed transition temperatures of the order of 82 K. A disadvantage of any postannealment process is the tendency for defects and impurities to aggregate rather than spread uniformly through the film as is the case for an *in situ* process [18]. This may result in increased weak-link behavior for the postannealed films, in addition to more sensitivity to processing steps and environmental conditions. Furthermore, the postannealment process is incapable of growing fully *c*-axis-oriented films of Y-Ba-Cu-O at film thicknesses greater than 300 nm, and multilayer HTS film deposition is also precluded. Thus, an optimized *in situ* growth process should ultimately provide the best Y-Ba-Cu-O thin films.
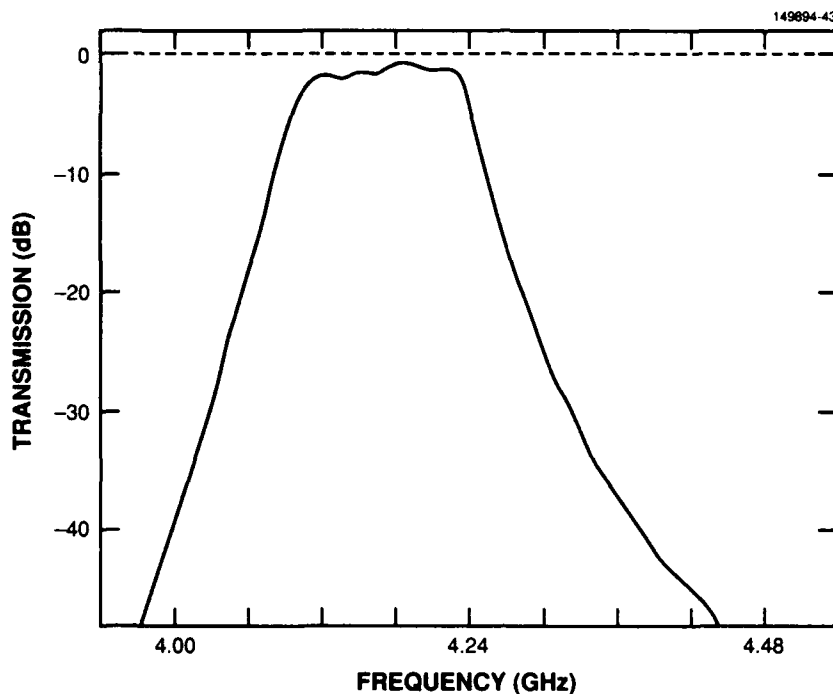
Figure 6-12. Measured transmission response at 77 K of a filter fabricated with a Y-Ba-Cu-O signal line, grown in situ on a 500-μm-thick LaAlO₃ substrate, and a silver ground plane. Passband insertion loss is 1.7 dB (reduced to 0.3 dB at 69 K) and shows an 80-MHz shift of the center frequency from that measured at low temperature. The frequency shift is due to the kinetic inductance caused by the very large penetration depth existing in the superconductor near the transition temperature.

In summary, four-pole microstrip filters have been produced that have nearly lossless passband characteristics and excellent out-of-band rejection at liquid-nitrogen temperature. These results have demonstrated that complex passive microwave devices can be designed and implemented using HTS materials. More aggressive filter designs utilizing many more poles will result in much greater performance advantages for an HTS filter technology over a normal-metal technology. Ultimately, ultrasharp-skirt filters can be produced, which would allow more closely spaced communication channels and more efficient use of microwave communication bands than are currently possible with conventional filters.

W.G. Lyons   [†]M.L. O'Malley
[*]R.R. Bonetti   A.C. Anderson
[*]A.E. Williams   R.S. Withers
[†]P.M. Mankiewich   [†]R.E. Howard
[*]A. Meulenberg

[*] COMSAT Laboratories, Clarksburg, Maryland.
[†] AT&T Bell Laboratories, Holmdel, New Jersey.

REFERENCES

1. D.E. Mars and J.N. Miller, *J. Vac. Sci. Technol. B* **4**, 571 (1986).

2. G.G. Harman, *Rev. Sci. Instrum.* **31**, 717 (1960).

3. M. Laugier, *Thin Solid Films* **67**, 163 (1980).

4. P. Baeri, S.V. Campisano, E. Rimini, and J.P. Zhang, *Appl. Phys. Lett.* **45**, 398 (1984).

5. J. Accinno and J.F. Schneider, in *Platinel a Noble Metal Thermocouple*, edited by C.H. Herzfeld (Reinhold, New York, 1962), Vol. 3, Pt. 2, Chap. 13.

6. M.G. Cooper, B.B. Mikic, and M.M. Yovanovich, *Int. J. Heat Mass Transfer* **12**, 279 (1969).

7. A. Inam, M.S. Hegde, X.D. Wu, T. Venkatesan, P. England, P.F. Miceli, E.W. Chase, C.C. Chang, J.M. Tarascon, and J.B. Wachtman, *Appl. Phys. Lett.* **53**, 908 (1988).

8. G. Koren, A. Gupta, E.A. Geiss, A. Segmüller, and R.B. Laibowitz, *Appl. Phys. Lett.* **54**, 1054 (1989).

9. M. Komuro, Y. Kozono, Y. Yazawa, T. Ohno, H. Hanazono, S. Matsuda, and Y. Sugita, *Jpn. J. Appl. Phys.* **26**, L1907 (1987).

10. H.C. Li, G. Linker, F. Ratzel, R. Smithey, and J. Geerk, *Appl. Phys. Lett.* **52**, 1098 (1988).

11. R.L. Sandstrom, W.J. Gallagher, T.R. Dinger, R.H. Koch, R B. Laibowitz, A.W. Kleinsasser, R.J. Gambino, B. Bumble, and M.F. Chisholm, *Appl. Phys. Lett.* **53**, 444 (1988).

12. C.B. Eom, J.Z. Sun, K. Yamamoto, A.F. Marshall, K.E. Luther, T.H. Geballe, and S.S. Laderman, *Appl. Phys. Lett.* **55**, 595 (1989).

13. X.X. Xi, G. Linker, O. Meyer, E. Nold, B. Obst, F. Ratzel, R. Smithey, B. Strehlau, F. Weschenfelder, and J. Geerk, *Z. Phys. B* **74**, 13 (1989).

14. T. Terashima, Y. Bando, H. Ma/aki, K. Iijima, K. Yamamoto, and K. Hirata, *Appl. Phys. Lett.* **53**, 2232 (1988).

15. M.S. DiIorio and A.C. Anderson, *Phys. Rev. B* **38**, 7019 (1988).

16. D.E. Oates and A.C. Anderson, to be published in *Proc. SPIE* **1187** (1990).

17. P.M. Mankiewich, J.H. Scofield, W.J. Skocpol, R.E. Howard, A.H. Dayem and E. Good, *Appl. Phys. Lett.* **51**, 1753 (1987).

18. T. Venkatesan, private communication.

REPORT DOCUMENTATION PAGE

Public reporting burden for this collection of information is estimated to average 1 hour per response, including the time for reviewing instructions, searching existing data sources, gathering and maintaining the data needed, and completing and reviewing the collection of information. Send comments regarding this burden estimate or any other aspect of this collection of information, including suggestions for reducing this burden, to Washington Headquarters Services, Directorate for Information Operations and Reports, 1215 Jefferson Davis Highway, Suite 1204, Arlington, VA 22202-4302, and to the Office of Management and Budget, Paperwork Reduction Project (0704-0188), Washington, DC 20503

1. AGENCY USE ONLY (Leave blank)	2. REPORT DATE 15 February 1990	3. REPORT TYPE AND DATES COVERED Quarterly Technical Report, 1 November 1989 — 31 January 1990

4. TITLE AND SUBTITLE

Solid State Research

5. FUNDING NUMBERS

C — F19628-90-C-0002
PE — 63250F
PR — 221

6. AUTHOR(S)

Alan L. McWhorter

7. PERFORMING ORGANIZATION NAME(S) AND ADDRESS(ES)

Lincoln Laboratory, MIT
P.O. Box 73
Lexington, MA 02173-9108

8. PERFORMING ORGANIZATION REPORT NUMBER

1990:1

9. SPONSORING/MONITORING AGENCY NAME(S) AND ADDRESS(ES)

Air Force Systems Command, USAF
Andrews AFB
Washington, DC 20334-5000

10. SPONSORING/MONITORING AGENCY REPORT NUMBER

ESD-TR-90-027

11. SUPPLEMENTARY NOTES

None

12a. DISTRIBUTION/AVAILABILITY STATEMENT

Approved for public release; distribution is unlimited.

12b. DISTRIBUTION CODE

13. ABSTRACT *(Maximum 200 words)*

This report covers in detail the research work of the Solid State Division at Lincoln Laboratory for the period 1 November 1989 through 31 January 1990. The topics covered are Electrooptical Devices, Quantum Electronics, Materials Research, Submicrometer Technology, Microelectronics, and Analog Device Technology. Funding is provided primarily by the Air Force, with additional support provided by the Army, DARPA, Navy, SDIO, NASA, and DOE.

14. SUBJECT TERMS

electrooptical devices	microelectronics	optical modulators	planarization techniques
quantum electronics	analog device technology	waveguide antennas	charge-coupled devices
materials research	lasers	epitaxial layers	superconductors
submicrometer technology	nonlinear optics	microwave semiconductor devices	

15. NUMBER OF PAGES

100

16. PRICE CODE

17. SECURITY CLASSIFICATION OF REPORT Unclassified	18. SECURITY CLASSIFICATION OF THIS PAGE Unclassified	19. SECURITY CLASSIFICATION OF ABSTRACT SAR	20. LIMITATION OF ABSTRACT